Fluid flow and heat transfer in dual-scale porous media

Morteza Hangi

A thesis submitted for the degree of

Doctor of Philosophy

The Australian National University

June 2020

Except where otherwise indicated, this thesis is my own original work.

Morteza Hangi
June 2020

I dedicate this thesis to my parents Lotfollah and Zahra for their endless support and encouragement, and my beloved wife Maryam who has made sacrifices by withstanding our distance.

Acknowledgements

First and foremost, I would like to express my special appreciation to my supervisor, Prof Wojciech Lipiński, for his valuable guidance and tremendous support throughout this project. His enthusiasm and inspiration were essential to the success of this research, and his wisdom and insights will serve as a source of ideas for my future endeavours.

I would not have been able to finish this research journey without Dr Vincent Wheeler who has taught me to approach problems from different angles and steered me in the right direction over the course of my PhD. Let me express my special thanks to Dr Alireza Rahbari for his valuable support and fruitful discussions. He has been a loyal colleague and an enthusiastic academic partner throughout my research.

I wish to thank Prof Adrian Sheppard from the Department of Applied Mathematics at the Australian National University for his advisory role in my PhD studies, and also all the members of Solar Thermal Group at the Australian National University for creating a more cooperative and positive work atmosphere during these years.

The support by the Australian Research Council through Prof Wojciech Lipiński's Future Fellowship, award no. FT140101213, is gratefully acknowledged.

Abstract

Porous media are omnipresent in various natural and engineered systems. The study of transport phenomena in porous media has attracted the attention of researchers from a wide variety of disciplines. In many applications such as hydrogeology, petroleum engineering and thermochemistry, porous media are encountered, in which heterogeneity exists at a multitude of length-scales. In solar thermochemical reactors, a promising approach to accomplish the thermochemical cycle is to form the reactive solid into a porous structure to promote efficient solid–gas reactions through a high specific surface area, while simultaneously achieving desired transport characteristics. Recently, in light of the apparent trade-offs between rapid reaction kinetics and efficient radiation absorption, reticulated porous ceramics (RPCs) featuring dual-scale porosity have been engineered. These structures are capable of combining the desired properties, namely uniform radiative absorption and high specific surface area. Therefore, investigations are required to understand and analyse different transport phenomena in such structures.

This dissertation is motivated by the need for understanding and analysing transport phenomena dual-scale porous media appear and used in many applications such as hydrogeology, petroleum engineering, chemical reactors, and in particular, energy technologies in high-temperature thermochemistry. The main objective of this thesis is to theoretically formulate and numerically demonstrate the fluid flow and heat transfer phenomena in dual-scale porous media. The theoretical and numerical results are used to propose models in forms of effective flow and heat transfer coefficients. The models are capable of estimating the fluid flow and heat transfer phenomena taking place in dual-scale porous media with appropriate fidelity and lower computational cost. The physical understanding of the models of transport phenomena in dual-scale porous structures allows us to tailor and optimise the morphology to accomplish optimal transport characteristics for the desired applications.

To determine the flow coefficients, numerical simulations are performed for the fluid flow in a dual-scale porous medium. Two numerical procedures are considered. Firstly, we

perform direct pore-level simulations by solving the traditional mass and momentum conservation equations for a fluid flowing through the dual-scale porous structure. Secondly, numerical simulations are performed at the Darcy level. For this purpose, the permeability and Forchheimer coefficient of the small-scale pores are numerically determined. Then, they are implemented in Darcy-level simulations in which the volume-averaged and traditional conservation equations are solved for the small- and large-scale pores, respectively. The results of the two approaches are separately used to determine and compare the permeability and Forchheimer coefficient of the dual-scale porous media.

To analyse the energy transport phenomena in dual-scale porous media, a mathematical model is developed by applying volume-averaging method to the convective–conductive energy conservation equation to derive the large-scale equations with effective coefficients. The closure problems are introduced along with the closure variables to establish the closed form of the two-equation model for heat transfer of dual-scale porous media. The closure problems are numerically solved for specific cases of dual-scale porous medium consisting of packed beds of porous spherical particles. The effective coefficients appearing in the two-equation model of heat transfer in dual-scale porous media are determined using the solution of the closure problems. The velocity field in the dual-scale porous structure is calculated using the solution of the fluid flow simulations in dual-scale porous medium. Finally, "numerical experiment" is performed to qualitatively and quantitatively analyse the accuracy of the numerical results obtained using the up-scaled model in comparison with those of the pore-level simulations.

The mathematical models developed in this work allow for the convenient use of the up-scaled conservation equations with the effective coefficients to numerically analyse the fluid flow and heat transfer in dual-scale porous media at a reduced computational cost.

Publications

- M. Hangi, V.M. Wheeler, W. Lipiński, Numerical determination of permeability and Forchheimer coefficient in dual-scale porous media, *International communication in Heat and Mass Transfer*, Under review.
- W. Lipiński, E. Abbasi-Shavazi, J. Chen, J. Coventry, M. Hangi, S. Iyer, A. Kumar, L. Li, S. Li, J. Pye, J.F. Torres, B. Wang, Y. Wang, V. Wheeler, Progress in heat transfer research for high-temperature solar thermal applications, *Applied Thermal Engineering*, (2020), 116137.
- M. Hangi, V.M. Wheeler, W. Lipiński, Convective–conductive heat transfer in dual-scale porous media: Theoretical model development and numerical validation, *International Journal of Heat and Mass Transfer*, 157 (2020) 119950.
- M. Hangi, V.M. Wheeler, W. Lipiński, Numerical investigation of heat and mass transfer in a structured packed bed of porous spherical particles, *International Heat Transfer Conference*, August 2018, 8067–8073.
- V.M. Wheeler, R. Bader, P.B. Kreider, M. Hangi, S. Haussener, W. Lipiński, Modelling of solar thermochemical reaction systems, *Solar Energy*, 156 (2017) 149–168.

Content

List of Figures

List of Tables

Nomenclature

Symbols

A	interfacial area (m^2)
b	closure variable vector (m)
c_F	Forchheimer coefficient
c_p	specific heat (J/kg K)
h	Convective heat transfer coefficient (W/m^2 K)
K	permeability (m^2)
k	thermal conductivity (W/m K)
K	thermal conductivity tensor (W/m K)
k_r	thermal conductivity ratio
n	unit normal vector (m)
Nu	Nusselt number
p	pressure (Pa)
q	volumetric flow rate (m^3/s)
q''	heat flux (W/m^2)
Re	Reynolds number
s	arbitrary source term
T	temperature (K)
u	x-component of velocity vector (m/s)
v	velocity vector (m/s)
v	y-component of velocity vector (m/s)
V	volume (m^3)
w	z-component of velocity vector (m/s)
x	x direction of Cartesian coordinates (m)
y	y direction of Cartesian coordinates (m)
z	z direction of Cartesian coordinates (m)

Greek symbols

ε	porosity
μ	viscosity (Pa s)
ρ	density (kg/m^3)
φ	volume fraction of regions
ψ	arbitrary transport variable

Subscripts

eff	effective
β	β-phase
η	η-region
σ	σ-phase
ω	ω-region

Superscripts

η	η-region
ω	ω-region

Abbreviations

3D	three-dimensional
3DOM	three-dimensionally ordered microporous
BCC	body-centred cubic
CFD	computational fluid dynamics
CT	computed tomography
DPLS	direct pore-level simulation
FCC	face-centered cubic
IBM	immersed boundary method
LHS	left hand side
LTE	local thermal equilibrium
LTNE	local thermal non-equilibrium
PIV	particle image velocimetry
REV	representative elementary volume
RHS	right hand side
RPC	reticulated porous ceramic

SAT	spatial averaging theorem
SC	simple cubic
SSA	specific surface area (1/m)
UDF	user-defined function
UDS	user-defined scalar
VAM	Volume-averaging method

Chapter 1
Introduction

Natural and artificial porous media are omnipresent in various natural and engineered systems. The study of transport phenomena in porous media has attracted the attention of researchers from a wide variety of disciplines including Civil Engineering, Hydrology, Mechanical Engineering, Chemical and Petroleum Engineering, Material Engineering, and Biomedical Engineering, to name but a few [1]. Examples of porous media found in nature are gas and oil reservoirs, aquifers, and biomedical tissues such as vertebrate skeleton and plants vascular system. In addition, porous media have been designed and engineered to be used in different industrial systems such as fuel cells, chemical reactors, filtration processes, and building insulations.

1.1. Motivation

"With the significant paradigm shift towards sustainable development in response to the growing environmental, economic, and security concerns associated with vulnerable reliance on fossil fuels, growing energy demand and continuing unmitigated CO_2 releases, it becomes apparent that clean and renewable energy technologies will remain in the focus of international research and development activities in the foreseeable future" [2]. One of the recent technologies in the field of renewable fuel production is to thermally dissociate H_2O and CO_2 via solar thermochemical cycles based on metal oxide redox reactions [3–8]. Figure 1.1 schematically shows the working principle of a two-step solar thermochemical redox cycle [9]. In the first endothermic step, a metal oxide is thermally reduced using concentrated solar radiation to a lower oxidation state. Subsequently, in the exothermic oxidation step, reduced metal oxide is reoxidised with H_2O and/or CO_2 to form H_2 and/or CO (synthetic gas). Finally, the reduced metal oxide is recycled to be used again in the cycle.

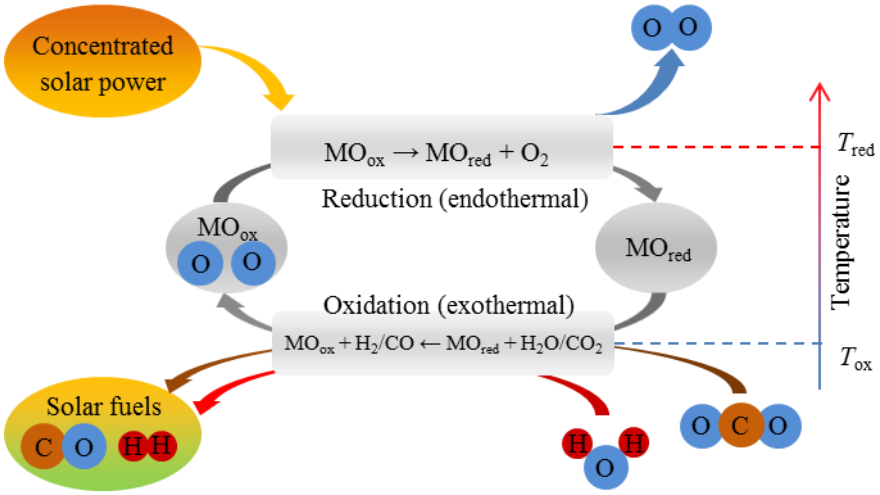

Figure 1.1. Schematic of the two-step solar thermochemical redox cycles for syngas production.

The idea behind this technology is that by coupling the cycle to CO_2 capture directly from atmospheric air, the same amount of CO_2 is used to produce the fuel as is emitted by the combustion of the fuel. Thus, these solar-made hydrocarbon fuels can be considered as carbon-neutral fuels. Different variety of metal oxide redox pairs, such as Fe_3O_4/FeO, ZnO/Zn, SnO_2/SnO and CeO_2/Ce_2O_3, have been theoretically and experimentally assessed for solar H_2O/CO_2 splitting [10–15]. However, irrespective of the applied metal oxide redox pairs, a promising approach to accomplish the thermochemical cycle in a solar reactor is to form the reactive solid into a porous structure to promote efficient solid–gas reactions through a high specific surface area, and simultaneously achieving desired transport characteristics [3, 5, 16, 17].

The first reduction step is usually performed with solar reactors that are directly exposed to high-flux solar irradiation. Within the reactor, the more uniform the porous metal oxide is heated, the more efficient the metal oxide is reduced. Thus, uniform radiative absorption is desired to enable uniform volumetric heating of the structure. Thus, a porous structure with slightly large pores is desirable such that the radiation can penetrate through the medium. On the other hand, the second oxidation step is largely surface dependent. Thus, large specific surface area (SSA) is desired to enhance reaction kinetics. In a porous structure, it is well established that the smaller the pores are, the larger the SSA becomes.

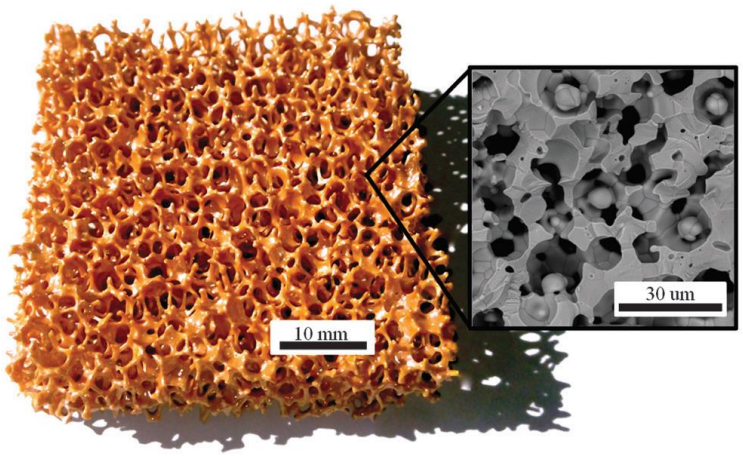

Figure 1.2. An RPC ceria sample with dual-scale porosity. Reprinted from [18] with permission from Royal Society of Chemistry.

However, porous structures supporting redox materials generally features only one of two desired properties: either with pores in μm-range exhibiting high SSA and less uniform radiative absorption, or with pores in mm-range exhibiting low SSA and more uniform radiative absorption. Recently, in light of the apparent trade-offs between rapid reaction kinetics and efficient radiation heat transfer, reticulated porous ceramics featuring dual-scale porosity were engineered, which are capable of combining both of the desired properties, namely uniform radiative absorption and high SSA [5, 18–23]. Figure 1.2 shows a dual-scale RPC ceria sample which can be used in a solar thermochemical reactor for H_2O and CO_2 splitting [18]. Such novel structure can provide pores in the scale of millimetre for efficient radiative penetration and also micrometre pores within the struts to provide large surface area for the heterogeneous chemical reaction.

For such novel technology in renewable fuel production, performing numerical simulations can not only give us insight into different phenomena occurring in a solar thermochemical reactor, but also enable us to find optimal designs for more efficient fuel production. Therefore, numerical simulations at a reactor level are needed to be performed to solve for heat and mass transfer coupled with chemical reaction. In a solar thermochemical reactor equipped with a dual-scale porous metal oxide (as illustrated in Figure 1.2), different length-scales are present from micrometers for the pores inside the struts to meters for the reactor and cavity receiver. Thus, performing numerical simulations at the reactor level is impossible using conventional numerical methods, since it requires enormous computational

resources. However, if we can propose models for the transport features taking place in the dual-scale porous media, it becomes possible to numerically analyse the phenomena occurring at the large-scale with logical computational cost. In addition, the effective transport properties of the media depend on the morphology. Thus, physically understanding the models of transport features of dual-scale porous structures enables us to engineer and optimise the morphology of the medium to achieve optimal transport characteristics for the desired applications. Investigation of transport in porous structures featuring different length-scales can not only give a comprehensive insight into fundamental aspects of the transport phenomena in such structures, but also prepare the ground for developing numerical simulations to be used in practical large-scale engineered systems.

1.2. Thesis outline

A comprehensive review of the literature is presented in Chapter 2 to understand the fundamentals of the field under study and to identify the knowledge gaps in the literature. This survey includes the background of the works that have been done to investigate modes of transport in different porous structures, and the approaches used to model such transport phenomena, including analytical, computational and experimental approaches. More attention is given to the studies in which the up-scaling method of volume averaging is used to theoretically analyse the transport phenomena in porous media.

In Chapter 3, the fluid flow in a dual-scale porous medium is numerically investigated at the pore level. The dual-scale porous medium is consisted of a packed bed of porous spherical particles. The void-space between the spherical particles is the big pores. Inside the spherical particles, there is three-dimensionally ordered macroporous (3DOM) media featuring small interconnected pores. For direct pore-level simulations (DPLS), the mass and momentum conservation equations are solved for a fluid flowing in the media using the finite volume method. The results are then used to calculate the permeability and Forchheimer coefficient of the dual-scale porous media. In addition, the permeability and Forchheimer coefficient of the 3DOM structures are numerically determined to be implemented in Darcy-level simulations. Finally, the results of Darcy-level simulations are compared with those of the direct pore-level simulations.

Chapter 4 presents a theoretical model development of heat transfer in dual-scale porous media. Firstly, the methodology is introduced, which is the method of volume averaging

applied for up-scaling transport phenomena. Then, a dual-scale porous structure is defined along with the associated length-scales, followed by the energy conservation equation and boundary conditions at the smallest scale considered in this work. The volume-averaging procedure is applied to the terms appearing the energy conservation equation. Then, the up-scaled energy equation is introduced along with the effective coefficients which take into account the heat transfer of the small-scale in the up-scaled equation. Finally, the closure problems are introduced. The effective coefficients are calculated using the solution of the closure problems.

Chapter 5 presents the numerical determination of the effective coefficients for different cases of dual-scale porous media. Firstly, the closure problems are numerically solved in 3D unit cells of packed beds of porous particles with different arrangements, representing the dual-scale porous media. The solution of the closure problem is then used to determine the effective coefficients appearing in the up-scaled energy equation. Finally, the results of the up-scaled model are compared with those of the pore-level simulations to investigate the fidelity of the up-scaled model.

The key findings of this dissertation are summarises in Chapter 6, followed by recommendations for future work.

Chapter 2
Background

This chapter reviews the work done in the field of transport in porous media. This survey includes the background of the works that have been done to investigate modes of transport, including mass, momentum and heat transfer, in different porous structures. In addition, a brief review is presented for the approaches used to model transport phenomena in porous media, including analytical, computational and experimental approaches. Since the methodology used in current dissertation is the method of volume averaging, more attention is given to review the studies in which this up-scaling method is used to theoretically analyse the transport phenomena in porous media.

2.1. Significance of transport phenomena in porous media

Different transport phenomena in porous media, including diffusion and adsorption, single- and multi-phase fluid flow, and different modes of heat transfer, can occur at various length-scales from nano- and micro-meters to tens of meters. Therefore, it is of great importance to investigate each of the mentioned processes both individually and simultaneously. Such effort results in understanding and controlling the transport occurring in natural porous systems, as well as designing optimal engineered porous structures with desired transport features to be used in relevant industries.

Mass transfer in porous structures is an important aspect of many environmental and engineering processes, including catalysis, reactors, petroleum recovery and separation via membranes. There are numerous examples of diffusion-controlled processes in various fields of engineering and science. For instance, diffusion can control the catalytic performance in porous catalysts [24], the ion- and proton exchange in fuel-cell electrodes [25], and species separation rate in membranes [26, 27]. It was shown in many experimental studies that the diffusion process in porous media is slower than that of a normal container without porous

media. Therefore, different effective diffusion coefficients have been proposed in porous media. Salama [28] used X-ray computed tomography scanning method to measure the diffusion of some hydrocarbon solvents in heavy oil in the presence of sand. Gooddy et al. [29] developed a method that enables the rapid determination of the effective diffusion coefficient of a solute in chalk. They reported that the outward diffusion of solute is not well characterised, however, an acceptable estimation of the apparent diffusion coefficient can be obtained with a relatively small effort. Cave et al. [30] presented a simple non-destructive method to measure one-dimensional pore diffusion coefficients in low-permeability geologic porous materials based on X-ray radiography. They concluded that the radiography measurements can significantly reduce the time for diffusion experiments, and also visualise the small-scale heterogeneities in diffusive properties within rocks.

In various environmental and engineering applications, there exists fluid flow in porous media. In this case, the mass transport in a porous medium is mostly controlled by the fluid displacement, which is called hydrodynamic dispersion [31]. In other words, the distribution of mass inside the porous structure is a result of the velocity field developing in the medium. In addition, when flow rate is very small in a porous medium, the contribution of mass transport by diffusion and dispersion can be comparable to each other, which means they are needed to be considered simultaneously. Different models have been introduced for dispersion coefficient in porous media, which take into account the effect of pure diffusion and fluid flow. Bernard and Wilhelm [32] and Carberry [33] studied the effect of particle shape on dispersion in fixed beds. They observed that using non-spherical particles leads to higher values of dispersion in comparison with similarly-sized spherical particles. Auset and Keller [34] investigated the effect of particle and pore size on colloid dispersion at the pore-level. They observed that the value of the dispersion coefficient at any constant flow rate depends not only on the pore-space geometry but also on the size of the pore channels and the size of the colloids.

Fluid flow in porous media is of great importance since it can significantly affect transport phenomena. The fluid dynamics in porous media is a relatively old topic. Since the development of Darcy's law in 1856 [35], it has been extensively used to estimate the velocity field in porous structures. Darcy's law correlates the pressure drop to the bulk velocity as:

$$\frac{\Delta p}{L} = \frac{\mu}{K}\frac{q}{A} \tag{2.1}$$

where Δp denotes the pressure difference across the length L, μ is fluid dynamic viscosity, K is the permeability of the porous media, q is the fluid volumetric flow rate, A is cross-section area of the bulk porous media. There are some assumptions made in the development of Darcy's law: (i) the solid phase is rigid; (ii) there is no chemical reaction; (iii) the fluid is homogeneous and incompressible; (iv) the value of Reynolds number is low, and (v) the drag coefficient is independent of velocity and pressure. It has been shown over the years that many of the above-mentioned assumptions are no longer valid for specific applications. For instance, as the Reynolds number increases, the contribution of inertial terms to the momentum balance leads to deviation from Darcy's law [36, 37], leading to the well-known Forchheimer modification of the Darcy's law [38]:

$$\frac{\Delta p}{L} = \frac{\mu}{K}\frac{q}{A} + \rho\beta\left(\frac{q}{A}\right)^2 \tag{2.2}$$

where ρ is the fluid density and β is the inertial flow coefficient. To predict momentum transport in porous media, Brinkman [39] modified the Darcy's law by introducing a term which takes into account the fluid–solid boundary effects. In Brinkman's model, an effective viscosity was proposed by considering the effect of porosity as below:

$$\mu_{\text{eff}} = \mu\left[1+2.5\left(1-\varepsilon\right)\right] \tag{2.3}$$

where ε is the porosity of the medium. In addition, studies have been carried out to modify the above correlation to take into account different types of porous structures [40].

Different modes of heat transfer (i.e. conduction, convection and radiation) can occur in porous structures used in various applications including thermochemical reactors [41, 42], compact heat exchangers [43, 44] and solar receivers [45, 46]. In porous media, the conduction heat transfer takes place in both solid struts with high thermal conductivity and fluid in the pores with lower thermal conductivity. Maxwell [47] was among the first researchers who studied the thermal conductivity in a fluid-saturated porous medium. Thus far, numbers of models have been proposed to determine effective thermal conductivity in different porous media such as packed beds of spheres [48] and metal foams [49, 50]. Singh [51] made a comprehensive review on various models of effective thermal conductivity in porous media. It was stated that apart from the thermal conductivities of the solid and fluid

phases and porosity, the effective thermal conductivity depends on the morphology of the porous structure and interphase interactions.

In a porous medium, convective heat transfer arises when a fluid is flowing in the pores and around the solid struts, and this phenomenon is of practical interest in many industries. Generally speaking, porous media can provide very large specific surface area resulting in high overall heat transfer, which makes them promising structures to be used in many thermochemical reactors and thermal management applications. When there is a fluid flow in a porous medium, the energy transport is actually a conjugate heat transfer problem. Heat transfers in the solid struts by means of conduction, and then, is taken away via convection by the fluid flowing around the solid struts at the exposed surface area. Studies have been performed to measure convective heat transfer coefficients of different porous structures. Eroshenko and Yaskin [52] analysed the problem of forced convection in sintered metal foams, and reviewed the latest results reported in the field. Dixon et al. [53] and Balakrishnan and Pei [54] studied convection heat transfer in packed bed systems, and proposed model for overall heat transfer coefficients. Calmidi and Mahajan [55] experimentally and numerically investigated the forced convection of air in high-porosity aluminium foams. They reported that due to relatively low values of effective thermal conductivity of the foam, the extended-surface efficiency of the porous block is very low, and convective heat transfer only occurs in a thin layer adjacent to the heated surface. More recently, with the help of numerical methods, convective heat transfer of different porous structures have been analysed at the pore level. Yang et al. [56] numerically studied the flow and heat transfer of some novel structured packed beds. They observed that packing arrangement and particle shape can significantly affect the convective heat transfer. They reported that the traditional correlations obtained for randomly packed bed arrangements overpredict the pressure drop and Nusselt number (the ratio of convective to conductive heat transfer) for structured packed beds, and proposed new correlations. Petrasch et al. [21] performed pore-level simulations on the 3D geometry of an RPC sample obtained from X-ray computed tomography. The results of the numerical simulations were used to determine the interfacial heat transfer coefficient and to derive a correlation for Nusselt number, which in turn were compared to proposed experimentally-determined correlations.

While most studies are focused on heat transfer and fluid flow problems in various porous structures, few are devoted to the radiative transfer phenomena in porous media. Radiative transfer in porous structures is of importance in many high-temperature engineering applications including porous burners [57, 58], fuel cells [59], thermochemical reactors [8], and thermal insulation [60, 61]. In complex structures such as porous media, solving Maxwell equations becomes a computationally-demanding task. Inverse techniques have been developed to experimentally estimate the hemispherical/directional transmissivity and reflectivity of porous structures [62–64]. In addition, analytical models have been developed based on the independent scattering approach [65–67]. Significant efforts have been devoted to use more practical numerical procedures to model radiative transfer in porous systems, which can be classified into two categories. The first one is to use homogeneous phase approach in which the radiative transfer equation (RTE) is used to calculate the radiative properties of a porous system [68, 69]. In recent years, ray-tracing Monte–Carlo methods have been used to compute the intensity distribution in porous media. Similarly to the inverse techniques, the numerical results are used instead of experimental ones to predict radiative properties [70, 71].

2.2. Analysis of transport phenomena in porous media

In Section 2.1, it was shown how different modes of transport—including mass diffusion, fluid flow and heat transfer—can occur in porous structures. Therefore, modelling the mentioned phenomena is of significant importance in several fields of engineering. For instance, in enhanced oil recovery applications, the objective of water injection is to fill the voids saturated with oil to maintain the desired pressure. Therefore, understanding the multi-phase fluid flow behaviour can lead to more efficient oil recovery [72–74]. In addition, in the field of groundwater protection, modelling the diffusion of contaminants in porous rocks can give us insight into contamination of drinking water supplies. Last but not least, in modern thermochemical reactors equipped with porous reacting media, different modes of transport phenomena such as diffusion due to chemical reaction, fluid flow and heat transfer play a significant role. In this section, a review is conducted on different approaches used to investigate transport phenomena in porous media, including analytical, computational, and experimental techniques.

2.2.1. Theoretical methods

Mathematical description of transport phenomena in porous structures is rather complicated due to the presence of different length-scales. For the conventional numerical methods, spatial discretisation is required to consider all these length-scales to capture the details of the transport phenomena and remain stable. Such different length-scales can vary from nano- or micro-meters to tens of meters. Thus, it seems to be a computationally-challenging task, even with current advances in computer technologies.

Beside difficulty of resolving different length-scales, investigating average properties seems to suffice in most of the engineering applications. For instance, in a thermochemical reactor used for water-splitting, it is of interest to estimate the amount of hydrogen production in the cycle. Therefore, different up-scaling techniques have been used to propose averaged models to take into account the transport features at different length-scales. The objective of using up-scaling techniques is to theoretically provide models for transport features of small-scales which can be applied in the large-scale transport equations to significantly reduce the required computational time. In the following, a brief review is presented on the up-scaling techniques in the field of porous media.

Non-local theory

Non-locality on the macro-scale is the result of not using boundary data during the up-scaling procedure from micro-scale [75, 76]. For a given transport variable under consideration, if information coming from the regions of time and space is different from the point vicinity where the variable is evaluated, then the theory is said to be non-local. In the context of transport phenomena in porous media, a constitutive theory is called non-local if it includes time and/or space integration or higher-order derivatives. Therefore, it is not possible to define intrinsic properties attached to a point of space. It has been shown in some numerical and experimental studies that the macroscopic dispersion is non-local for specific heterogeneous structures [77–80].

The development of non-local theories is based on time integration of fluid flow in heterogeneous media, and the effect of velocity fluctuations is mainly investigated in a probabilistic manner [81, 82]. The macroscopic dispersion tensor is obtained from a spatio-temporal procedure involving a memory function that takes into account the complexity of the local velocity field [75, 83–85]. The local dispersion is neglected in these purely

adventive theories by judging its effect. This issue has been discussed many times, and extensions have been proposed [86, 87]. However, the major disadvantage is the difficulty of practically using such models, because of the complex definition of the macroscopic dispersion tensor.

Stochastic approach

Experimental techniques including core, seismic, and electric measurements do not allow providing a complete cartography of a geological formation. They provide either global and qualitative or precise and localised information. The analysis of all the data leads to defining statistical quantities related to heterogeneities. Due to the lack of reliable information in natural environments, stochastic theories have been proposed. In these approaches, a porous medium is considered as a realisation of a random phenomenon. The term "random" simply means that the configuration, arrangement, and properties vary from one realisation to another. Thus, the most appropriate tool to study its variations is probabilistic concept. However, in practice, there is only one realisation. To be able to use this probabilistic concept, two fundamental hypotheses are added:

- Stationarity hypothesis: it is generally assumed that, for all directions, the law of probability of the property under investigation is stationary in the space.
- Ergodicity hypothesis: it is possible to replace the spatial average of a variable in a single realisation with the ensemble average of the given variable within the ensemble. This hypothesis actually connects the single realisation to the ensemble.

In stochastic approach, a variable, such as the porosity, permeability, position, and velocity, at the Darcy level is defined by its average value plus a random time-statistical fluctuation term. Several hypotheses on the statistics of local properties are made in order to make it possible to theoretically develop the macroscopic equations. One of the most fundamental variables in the framework of the stochastic approach is the hydraulic conductivity of the medium (or permeability of the medium) whose variation in space reflects directly the field heterogeneity [88–90]. It was shown that the effects of porosity variation or the variation of the local dispersion coefficient are secondary to the effects of permeability distribution [91, 92]. Freeze [93] studied a large number of aquifers, and showed that the logarithm of the permeability followed a normal distribution. Dagan [94]

chose a Gaussian distribution for the random function representing the logarithm of the permeability. However, the proposed model seems to be valid only for a small range of variation in the permeability distribution. The models of transport phenomena in porous structures provided by the stochastic approach have been successfully verified in some numerical and experimental studies [95, 96]. However, it has been shown that the fundamental assumptions of this approach, in particular the ergodicity hypothesis, is only valid when the domains are unrealistically and infinitely large [97].

The homogenisation method

Homogenisation theory has been used to theoretically develop macroscopic models which are derived from microscopic transport phenomena in porous media. This method was firstly developed in the studies of partial differential equations for extremely heterogeneous media. The purpose of homogenisation theory is to study the limiting behaviour transport variables at the pore-level. The idea behind this theory is that the microscopic fluctuations of transport variables generated in pores will average out, resulting in a simple homogenised partial differential equation which governs the macroscopic behaviour. The basic principles of this theory can be found in the textbook by Yang [98]. The most famous work in this field was performed by Tartar [99, 100], who used the homogenisation theory on the Stokes equation in periodic domains to show the mathematical proof of Darcy's law and to obtain permeability tensor. Using homogenisation theory, researchers have theoretically investigated the mechanical characteristics of composite materials [101], transport phenomena in electrochemical systems [102], and nano-porous materials [103].

The method of volume averaging

The volume-averaging method (VAM) applies the volume-averaging operator to the transport equations. This method was firstly introduced by Anderson and Jackson [104], Slattery [105] and Whitaker [106]. Since then, it has been used as a general mathematical tool in a wide range of applications, including single- and two-phase flows, as well as heat and mass transfer. The methodology used in the current work is the volume-averaging method to theoretically develop the heat transfer in dual-scale porous structures. Thus, the details of this method are presented next, along with a brief review of application of this

method in the field of transport phenomena in porous media. Considering Figure 2.1, this method is based on the following two assumptions:

1) The characteristic length-scale of the first level is very small compared to the characteristic length-scale of the upper level.
2) The radius of the averaging volume is large relative to the characteristic length-scale of the first level, and small relative to the characteristic length-scale of the upper level.

These two ideas can be formulated as:

$$l_\beta, l_\sigma \ll r_0 \ll L \tag{2.4}$$

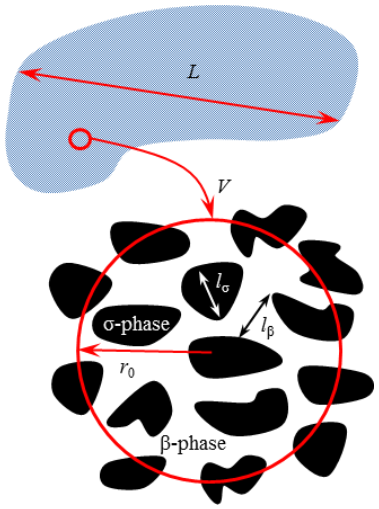

Figure 2.1. Characteristic length-scales at different levels and averaging volume.

Up-scaling techniques based on VAM have been widely used in different fields of engineering to derive the continuum governing equations and model transport phenomena in multiphase systems. In this method, the spatial and/or temporal averaging procedures are applied to the governing equations to remove the large gradients appearing in the microscopic field variables including pressure, velocity and temperature. Figure 2.2 schematically shows the volume-averaging procedure in a porous medium consisting of fluid (β) and solid (σ) phases. Applying VAM to the microscopic governing equations lead to the up-scaled volume-averaged equations with effective coefficients.

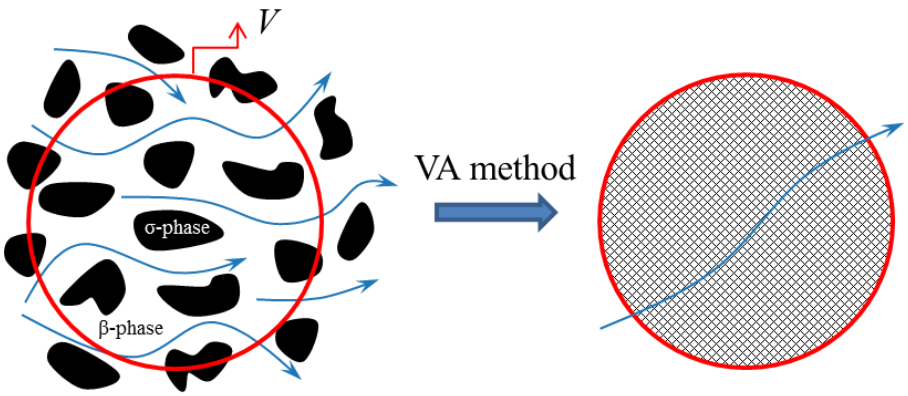

Figure 2.2. Schematic of the volume-averaging procedure in a porous medium.

The effective coefficients are obtained from the solution of the closure problems for a spatially periodic model of the given porous structure. The closure problems are derived by developing the governing equation for the spatial deviation of the transport property under study. Spatially-periodic assumption makes it possible to study the REV with periodic boundary condition instead of studying the entire porous domain. The REV needs to be large enough, such that the calculated effective coefficients from the solution of the closure problems for the selected REV can represent the whole porous medium. A rigorous mathematical development of the transport equations for multiphase systems was presented by Whitaker [107] and Gray [108]. The general procedure of the VAM is presented next. Assume that the general transport equation is as below:

$$\frac{\partial \psi}{\partial t} + \nabla \cdot \left(\mathbf{v} \psi \right) = \nabla \cdot \mathbf{\Omega} + s \tag{2.5}$$

where ψ, $\mathbf{v}$ and s are a generic transport variable, the velocity vector, and the source term, respectively. The parameter $\mathbf{\Omega}$ is a tensor with one order greater than ψ. Considering fluid (β) and solid (σ) phases in Figure 2.1, the averaging volume V is the sum of the volumes of the β- and σ-phases. Two definitions are used for the average of ψ to analyse the transport phenomena in the multiphase systems. The superficial or extrinsic average is defined as:

$$\left\langle \psi_\beta \right\rangle = \frac{1}{V} \int_{V_\beta} \psi_\beta \mathrm{d}V \tag{2.6}$$

The intrinsic average is defined as:

$$\left\langle \psi_\beta \right\rangle^\beta = \frac{1}{V_\beta} \int_{V_\beta} \psi_\beta \mathrm{d}V \tag{2.7}$$

The superficial and intrinsic averages are related to each other by the volume fraction of the phase ($\varepsilon_\beta = V_\beta / V$) as below:

$$\left\langle \psi_\beta \right\rangle^\beta = \varepsilon_\beta \left\langle \psi_\beta \right\rangle \tag{2.8}$$

During the averaging process, we make use of spatial averaging theorem (SAT) [109] which relates the average of a derivative to the derivative of the average as below:

$$\left\langle \nabla \psi_\beta \right\rangle = \nabla \left\langle \psi_\beta \right\rangle + \frac{1}{V} \int_{A_{\beta\sigma}} \mathbf{n}_{\beta\sigma} \psi_\beta \mathrm{d}A \tag{2.9}$$

$$\left\langle \nabla \cdot \psi_\beta \right\rangle = \nabla \cdot \left\langle \psi_\beta \right\rangle + \frac{1}{V} \int_{A_{\beta\sigma}} \mathbf{n}_{\beta\sigma} \cdot \psi_\beta \mathrm{d}A \tag{2.10}$$

where $A_{\beta\sigma}$ is the interfacial area between the β- and σ-phases, and $\mathbf{n}_{\beta\sigma}$ is the unit normal vector pointing from β to σ. In addition, to change the average of product into product of averages during the volume-averaging procedure, deviation terms ($\tilde{\mathbf{v}}_\beta$ and $\tilde{\psi}_\beta$) are defined as:

$$\mathbf{v}_\beta = \left\langle \mathbf{v}_\beta \right\rangle + \tilde{\mathbf{v}}_\beta \tag{2.11}$$

$$\psi_\beta = \left\langle \psi_\beta \right\rangle + \tilde{\psi}_\beta \tag{2.12}$$

With some arrangements and with the assumption of constant phase volume fractions, applying the volume-averaging procedure to Eq. (2.5) and using the definitions presented in Eqs. (2.9)–(2.12), the volume-averaged transport equations for the β- and σ-phases read:

$$\varepsilon_\beta \frac{\partial \left\langle \psi_\beta \right\rangle^\beta}{\partial t} + \nabla \cdot \left(\left\langle \mathbf{v}_\beta \right\rangle \left\langle \psi_\beta \right\rangle^\beta \right) + \nabla \cdot \left\langle \tilde{\mathbf{v}}_\beta \tilde{\psi}_\beta \right\rangle = \nabla \cdot \left\langle \mathbf{\Omega}_\beta \right\rangle + \frac{1}{V} \int_{A_{\beta\sigma}} \mathbf{n}_{\beta\sigma} \cdot \mathbf{\Omega}_\beta \mathrm{d}A + \varepsilon_\beta \left\langle s_\beta \right\rangle^\beta \tag{2.13}$$

$$\varepsilon_\sigma \frac{\partial \left\langle \psi_\sigma \right\rangle^\sigma}{\partial t} = \nabla \cdot \left\langle \mathbf{\Omega}_\sigma \right\rangle + \frac{1}{V} \int_{A_{\sigma\beta}} \mathbf{n}_{\sigma\beta} \cdot \mathbf{\Omega}_\sigma \mathrm{d}A + \varepsilon_\sigma \left\langle s_\sigma \right\rangle^\sigma \tag{2.14}$$

This procedure can be applied to the mass, momentum and energy conservation equations to derive the macroscopic transport equations.

In porous media, applying VAM to the microscopic transport equations leads to the macroscopic transport equations along with the explicit relation between the two regions in the form of the macroscopic coefficients appearing during the up-scaling procedure [109]. In the first studies of using VAM in porous structures, the method was applied to theoretically develop the up-scaled mass, momentum and energy conservation equations. For instance, applying VAM to the mass and momentum conservation equation in porous media leads to the development of Darcy and Darcy–Forchheimer equations along with the introduction of local effective coefficients as permeability and Forchheimer coefficient [110, 111].

$$-\nabla p = \frac{\mu}{K}\langle \mathbf{v} \rangle \tag{2.15}$$

$$-\nabla p = \frac{\mu}{K}\langle \mathbf{v} \rangle + \frac{\rho c_{\mathrm{F}}}{\sqrt{K}}\langle \mathbf{v} \rangle \left| \langle \mathbf{v} \rangle \right| \tag{2.16}$$

where $\langle \mathbf{v} \rangle$ is the superficial average velocity vector and c_{F} is the Forchheimer coefficient.

To theoretically analyse the diffusion phenomena in porous structures, VAM was applied to the species governing equation [106, 112], leading to the introduction of diffusivity tensor. In addition, volume-averaged energy conservation equation in porous media has been developed based on two assumptions. The first one is local thermal equilibrium (LTE) assumption leading to one-equation model with effective thermal conductivity tensor [113]. The second one is local thermal non-equilibrium (LTNE) assumption leading to two-equation model with effective thermal conductivity tensor plus the interfacial heat transfer coefficient which takes into account the convection heat transfer between the solid and fluid phases [114]. Lipiński et al. [115, 116] applied volume-averaging method to the discrete-scale equations of radiative transfer to theoretically derive the continuum-scale radiative transfer equations and the corresponding boundary conditions of two-phase and multi-component media.

In the earlier studies using the VAM to theoretically investigate the transport phenomena in porous media, many simplifications have been made including incompressible fluid, no heat source or linear heat sources, and single-phase fluid flow. Leroy and Bernard [117] considered up-scaling of heat transfer in porous media with nonlinear heat sources using VAM. They also made used of down-scaling methodology which allows reconstructing the temperature field and the heat source in the sub-domain of the porous media, in order to

improve the accuracy of the up-scaled heat transfer model. Zaouter et al. [118] analysed the flow of slightly compressible gas in fractured media. They applied VAM to mass, momentum, and gas state law equations to provide a macroscopic model with the definition of effective transmissivity tensor. They showed that an expansion to the first order in the Knudsen number (the ratio of the molecular mean free path to the representative physical length-scale) is carried out on the closure, yielding a decomposition of the effective transmissivity tensor into its purely viscous part and its slip correction. Qiu et al. [119] used volume-averaging method to up-scale multi-component mass transfer and reaction in rigid porous media. They considered the first-order reversible reaction occurring at the solid–fluid interface, and calculated the effective coefficients by solving the associated closure problems.

Apart from transport phenomena within porous media, the problem of transport at the boundary between a porous medium and a homogeneous fluid is of great importance as it occurs in a wide variety of technological applications. Therefore, studies have been conducted using VAM to investigate the interface conditions. Ochoa-Tapia and Whitaker [120, 121] developed the momentum transfer interface conditions as jump conditions, which apply at the boundary between a porous medium and a homogeneous fluid based on the non-local form of the volume-averaged momentum equation. They stated that further experimental studies are required to develop a reliable empirical representation. In another investigation performed by Ochoa-Tapia and Whitaker [122], VAM was applied to develop the heat transfer interface conditions at the boundary between a porous medium and a homogeneous fluid. The flux jump conditions derived in their study is in the form of surface transport equations consisting of excess surface accumulation, convection, conduction, and the excess surface heat exchange. Alazmi and Vafai [123] analysed the effect of using different types of interfacial conditions between a porous medium and a fluid layer on fluid flow and heat transfer at the vicinity of interface region. They investigated the effects of Darcy number (the ratio of permeability of the medium to its cross-sectional area), inertia parameter, Reynolds number (the ratio of inertial forces to viscous forces), porosity and slip coefficients. They concluded that using different interface conditions has more significant effect on the velocity field compared to the temperature field and Nusselt number distributions.

2.2.2. Experimental methods

Parallel to the theoretical methods, experimental techniques have been extensively used to investigate and model the transport phenomena in porous media. Macroscopic transport properties have been experimentally estimated for different porous structures. Straatman et al. [124] carried out experiments to quantify the hydraulic loss and convective heat transfer of water flowing through blocks of graphitic foams. Figure 2.3 shows the schematic of the experimental setup used in their study. A similar experimental setup was used in other studies in which the macroscopic heat and fluid flow properties were investigated. By using the classical Darcy–Forchheimer law for porous media, they calculated the permeability and Forchheimer coefficients from the pressure drop obtained experimentally. In addition, they used the correlation below to calculate the convective heat transfer coefficient h_{sf}:

$$\mathrm{Nu} = \frac{h_{sf} D}{k_{fa}} = \frac{q''}{\Delta T_{LM}} \frac{D}{k_{fa}} \tag{2.17}$$

where D is the characteristic pore diameter, k_{fa} is the fluid thermal conductivity, ΔT_{LM} is the log-mean temperature difference, and q'' is the heat flux.

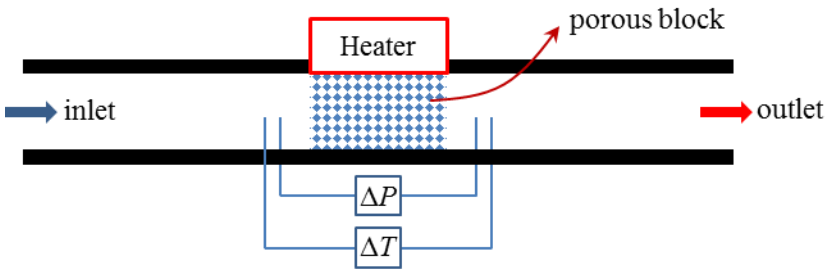

Figure 2.3. Schematic of experimental setup used for obtaining macroscopic heat and fluid flow properties. Reproduced from [124], with permission from ASME.

Similar experimental procedure was applied by Leong et al. [125] to estimate the permeability, Forchheimer coefficients and average Nusselt number of graphite foams. Yang et al. [126] experimentally studied the macroscopic hydrodynamic and heat transfer characteristics in structured packed beds with different arrangements. They reported that the traditional Ergun's [127] and Wakao's [128] equations overpredict the friction factors and Nusselt numbers for the structured packed beds, respectively. They proposed experimentally-modified correlations. From microscopic standpoint, studying flow and heat transfer characteristics in porous media is a difficult task due to the invasive characteristics of direct

measurement methods, high mixing and the inherent three-dimensionality of the flow. Recently, optical methods such as particle image velocimetry (PIV) have been used to achieve the required optical access and to microscopically investigate the transport phenomena [129–131]. Huang et al. [130] proposed imaging methods to characterise liquid flow through transparent porous medium composed of randomly packed beds of spheres. It was stated that the pore-level experimental results can be used to validate the direct pore-level simulations of the flow. Shams [132] used the PIV method to study flow behaviour at the interface of a porous medium and homogenous fluid. He reported that the fluid penetrates the porous medium much less significantly than predicted by Brinkman's equation. Although high quality 3D information can be provided by such experimental methods, they generally require expensive imaging equipment.

2.2.3. Computational methods

Transport phenomena in porous media significantly depend on several morphological and pore-level features such as tortuosity of the structure, irregular pore surfaces and even dead-end pores. Raoof and Hassanizadeh [133] demonstrated the significance of including kinetics obtained from the pore level, rather than relying on macroscopic properties. Therefore, studying the transport phenomena in porous media at the pore level is of great fundamental importance. Although it is possible to estimate the macroscopic effective properties of a porous structure by performing experiments, finding experimental correlation for such effective properties is an expensive task. In addition, the experimental investigation of transport phenomena in porous media is inherently difficult due to the invasive characteristics of direct measurement methods. Therefore, experimental methods can only give the macroscopic properties without any details about fluid–solid interaction, mixing, and secondary flows due to the fluid flow in tortuous interstitial pores.

Fatt [134] was amongst the first researchers who modelled a simple network of tubes representing real porous media, and derived the capillary pressure curves and pore size distributions. However, the real 3D pore-level modelling did not occur until the main advancement in computer power. The recent advancement in computers and imaging techniques has made it possible to three-dimensionally investigate transport phenomena in porous media at the pore level using numerical methods.

The first step to perform pore-level simulations is to choose the representative elementary volume (REV) of the given porous structure. The REV is the smallest volume of a structure which represents a property of the whole medium. If the porous sample is too small, oscillations are observed in the measurement of the property under study. By increasing the size of the sample, the observed fluctuations start to relax until the sample is big enough such that consistent measurements can be made for the property. There are several criteria to choose the dimensions of REV such as average pore diameter. However, this matter is not reviewed here for brevity. Once the appropriate size is selected for an REV, the 3D image of the structure is generated. One technique is to use direct imaging methods to generate the image of the porous structure using 2D destructive cutting [135], confocal laser scanning microscopy [136, 137] or X-ray computed tomography [138, 139]. Once the 3D images are generated, the physical model is built and meshed, and the numerical simulation can be performed [21-23, 140–146]. Void-space reconstruction is another technique to generate samples of porous media based on a statistical knowledge of the micro-structure of interest. In this method, a large number of small primitive objects, such as spheres and cylinders, are generated based on the dimensions obtained from statistical data describing the micro-structure of interest. Then, a finite domain is filled with the generated interfering primitives. The result is a digital domain representing the desired micro-structure, which is used in pore-level simulations to predict effective transport properties [147–156].

In a study performed by Vu and Straatman [156], the numerical results obtained using pore-level simulations were compared with of the volume-averaged model for three-dimensional spherical-void-phase models. They used the results of the pore-level simulations to establish effective coefficients such as the porosity, permeability, Forchheimer coefficients, interstitial exchange and interstitial surface area. They implemented the effective coefficients as closure coefficients in the volume-averaged model. It was shown that the temperature variations predicted by the volume-averaged model is acceptably close to those obtained using the pore-level simulation. Das et al. [157] applied immersed boundary method and CFD to solve the flow and heat transfer in an actual foam geometry obtained using a 3D scan of computed tomography. They compared their fluid flow results with those obtained using the Ergun correlation [127] as well as the experimental ones reported in [158]. They proposed a correlation for the Nusselt number of the foam sample.

Alam et al. [159] applied new techniques to obtain exact three-dimensional geometry of silicon carbide foams and performed direct pore-level simulations to study transport phenomena of the porous medium. By using this method, they were able to determine the thermal conductivity, permeability, friction factor, and heat transfer coefficients of the foam. It was claimed that the approach is quite general and can be used for other porous media. Suter et al. [146] experimentally characterised reticulate porous ceramic of ceria via 3D tomographic techniques. Then, they performed direct pore-level simulations on the generated geometry to determine the effective transport properties including extinction coefficient, scattering phase function, effective thermal conductivity, interfacial heat transfer coefficient, permeability, Dupuit–Forchheimer coefficient, and tortuosity. They concluded that such investigation provides guidance for pore-level engineering of materials used in solar reactors and other high-temperature heat and mass transfer applications.

Although performing numerical simulations on the exact porous structure generated by direct scanning can provide useful details of transport phenomena in porous media, it is an expensive and time-consuming task, in particular for performing parametric studies. Thus, idealised geometries have been generated based on the morphology of the porous medium. Then, numerical simulations are performed on the idealised REV [160–162]. Krishnan et al. [163] carried out direct simulations of the fluid flow and heat transfer in an open-cell metal foam using a periodic idealised unit cell. Figure 2.4 shows the geometry creation procedure for the metal foam unit cell. As depicted, the unit cell can be generated by subtracting the body-cantered cubic packing arrangement from the cube, where the diameter of the spheres is slightly larger than the cube edge length. They calculated the effective thermal conductivity, pressure drop, and convective heat transfer coefficient of the structure, and reported acceptable consistency with the existing experimental measurements and semi-empirical models. Choosing ideal periodic isotropic foam structures made it possible for Kumar and Topin [164] to study the effect of different strut shapes and their various orientations on the flow properties, namely the permeability and the inertia coefficient, for a wide range of porosity and Reynolds number. They compared their numerical results with the available experimental data, and observed an acceptable agreement.

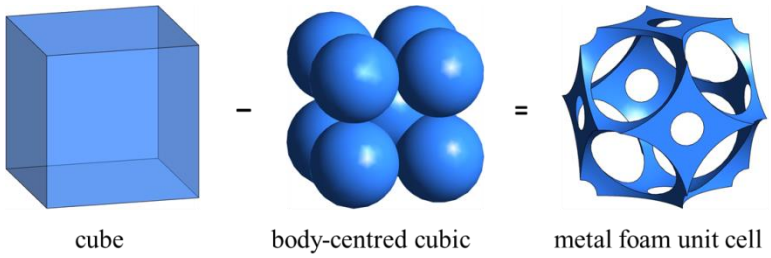

Figure 2.4. Metal foam unit cell geometry creation, reproduced from [163] with permission from ASME.

An interesting phenomenon in porous media is the transport occurring at the interface of a porous medium and homogeneous fluid. Sahraoui and Kaviany [165–167] performed direct pore-level simulations to analyse the fluid flow, conduction and convection occurring at the interface of porous and plain media. They examined the effect of fluid flow direction, porosity, Reynolds number, and the 2D porous structure arrangement on the velocity and temperature slip coefficients. It was observed that the slip coefficients depend on the structure, the flow direction, the Reynolds number, and the nonuniformity in the arrangement of the porous medium.

2.3. Transport phenomena in porous media with different length-scales

In many applications such as hydrogeology, petroleum engineering and chemical reactors, multiple length-scales are present in the porous media. By using VAM, models have been developed for such porous media, which can capture the phenomena occurring at different length-scales [168–171]. Quintard and Whitaker [172] considered the two-phase flow in heterogeneous porous media. They stated that the local volume averaging becomes extremely complex for a porous medium featuring different length-scales. Thus, large-scale averaging can be used to average the equations at the Darcy level over a region which is larger enough containing the different length-scales. Using the large-scale volume averaging of the continuity and momentum equations and assuming the principle of local mechanical equilibrium, they derived the up-scaled equations along with the closure problems. Solution of the closure problems leads to the calculation of large-scale permeability tensors and capillary pressure. In another study by Quintard and Whitaker [173], the transport of an adsorbing solute in a two-region model of a heterogeneous porous medium was theoretically analysed using large-scale VAM. They stated that if the assumption of large-scale mass equilibrium is valid, one-equation model can represent the solute transport process. With

such constraints, they developed the large-scale mass transport equation in terms of the large-scale average velocity, an average adsorption isotherm, and a single large-scale dispersion tensor. Yan et al. [174] applied the VAM to develop the closed form of solute transport in columns consisting of ordered pillar array columns with a thin retentive layer. They developed the closure problems and solved them for a unit cell with periodic boundary condition to calculate the dispersion tensor as a function of geometry shape and size, velocity field, retention, and resistance to mass transfer. They compared the results of their up-scaled model with those of the pore-level simulations as well as the experimental ones. Good agreement was observed. In another study performed by Yan et al. [175], they expanded their previous investigation and analysed the solute transport in hierarchical porous structure with reversible adsorption using the VAM. They derived a transient macroscopic advection–diffusion equation to describe the multi-scale solute transport problem, and introduced the closure problems. It was stated that the theoretical dispersion tensor is a function of velocity field at the pore level, and it can be calculated by performing pore-level simulations for unit cells of the hierarchical porous media. They concluded that the volume-averaged model can be used for predicting solute transport behaviour in packed beds of particles.

While numerous theoretical and experimental studies of transport phenomena exist for single-scale porous media, only few studies address transport phenomena in multi-scale porous media, e.g. for solute transport and advection–diffusion [173–175], and heat transfer problems [176–181]. Jadhav and Pillai [176] employed the control-volume approach to perform numerical simulation of 1D non-isothermal flow in fibrous dual-scale porous media based on energy balance in a two-layer model. They included conduction and convection between the two scales in their energy balance analysis. However, no definition for effective coefficients of the dual-scale porous media was presented. They stated that the conventional models for single-scale porous media cannot properly predict the heat transfer in dual-scale porous media, and more investigation is required to model and validate the heat transfer phenomena in a dual-scale porous medium. Munagavalasa and Pillai [177] performed numerical simulation on a 2D REV of an idealised dual-scale porous medium to estimate the effective thermal conductivity used in the volume-averaged energy equation of a dual-scale porous media. They included the convective heat transfer between the two regions in their volume-averaged energy equation. However, they only focused on the estimation of effective

thermal conductivity and its dependency on relevant parameters including velocity and spacing between regions.

Bi-disperse porous media (BDPM) is another terminology for porous structures with two different pore length-scales. in BDPM, the ligaments of the parent porous medium are porous themselves with interconnected pores [182, 183]. A review of the studies on convective heat transfer in bi-disperse porous media is presented by Nield and Bejan [182] and Mahmoudi et al. [183]. Nield and Kuznetsov [184–186] modelled fluid flow and heat transfer in BDPM, assuming LTE inside the micro-porous media. They proposed volume-averaged equations to model fluid flow and heat transfer in BDPM. Their volume-averaged two-equation model is an extended version of the two-equation model used for heat transfer in single-scale porous media based on LTNE assumption. They considered the convection term in both regions, without taking into account the energy exchange occurring as a result of fluid flow between the regions. The effective coefficients were not defined in their study. In addition, the model was not verified against experimental experimental data or the results obtained using pore-level simulations. In another study performed by Nield and Kuznetsov [187], they applied the same model to numerically investigate external natural convection in BDPM. Model verification was not performed by comparing the numerical results with experimental data or those obtained using pore-level simulations. The model proposed by Nield and Kuznetsov [184–186] was used by other researchers such as Kumari and Pop [188] for mixed convection of a circular cylinder embedded in a BDPM, and Wang and Li [189] for forced convection in BDPM incorporating viscous dissipation. Narasimhan and Reddy [190] and Narasimhan et al. [191] numerically investigated the application of BDPM in thermal management of heat generating electronics. They performed two-dimensional numerical simulations at the Darcy level—solving traditional conservation equations in the macro-pores and the volume-averaged conservation equations in the micro-pores. They assessed the effect of the permeability of the micro-porous region. Similar procedure was used in another study by Narasimhan and Reddy [192] to numerically investigate two-dimensional natural convection inside a square BDPM enclosure made from uniformly-spaced micro-porous blocks. However, the Darcy-level simulations performed in their study are computationally very expensive. Thus, this procedure is not feasible to model the three-dimensional transport phenomena in dual-scale porous structures in actual large-scale applications.

2.4. Research objectives

No previous pertinent studies reported the development of volume-averaged conservation equations for dual-scale porous media. A new approach to modelling the fluid flow and heat transfer in dual-scale porous media is proposed to facilitate computationally inexpensive but high-fidelity simulations suitable for large-scale applications. No studies have been reported on rigorously defining the effective fluid flow and heat transfer coefficients in a dual-scale porous media by performing multi-scale analyses of mass, momentum, and energy equations, and considering the exchange between the regions of different length-scales. This research gap needs to be addressed for contemporary engineering applications of dual-scale porous media in hydrogeology, petroleum engineering chemical reactors, and in particular high-temperature solar thermochemical systems featuring advanced materials-by-design [18, 19, 193–195]. Therefore, in order for the novel dual-scale porous structures to be used in their full potential in different applications, investigations are required to understand and model different transport phenomena in such structures. This issue becomes even more complicated, more important and worthy of investigation when dual-scale porous media are used as a reacting medium in high-temperature thermochemical reactors. In such applications, different modes of transport occur simultaneously, such as fluid flow, different modes of heat transfer and species transfer due to chemical reaction.

This dissertation is motivated by the need for understanding and analysing transport phenomena in structures featuring dual-scale porosity appear and used in many applications such as hydrogeology, petroleum engineering, chemical reactors, and in particular energy technologies in high-temperature thermochemistry. The main objective of this thesis is to theoretically formulate and numerically demonstrate the fluid flow and heat transfer phenomena in dual-scale porous media. To investigate the flow process, numerical simulations, at the pore and Darcy levels, are performed on fluid flow in a dual-scale porous medium. The effective flow coefficients are determined using the numerical results. To investigate heat transfer in dual-scale porous media, the up-scaling method of volume averaging [109] is used to progressively pass information from the smallest scale (pores in the struts of the medium depicted in Figure 1.2) to the largest one (the bulk of porous structure at the application level). The closed form of the energy equation in dual-scale porous media is derived, and the effective coefficients are defined. The up-scaled form of the

conservation equations with the effective coefficients are exactly the requirements for performing parametric numerical studies at the application level such as the reactor level.

2.5. Summary

A review of the literature in the field of transport phenomena in porous media has been presented in this chapter. The importance of modelling different transport phenomena in porous structures used in numerous natural and engineering applications was discussed. A review of the methods employed to investigate the transport phenomena in porous media has been presented, including theoretical, experimental, and computational methods.

In Section 1.1, the promising features of dual-scale porous structures have been discussed, in particular as a reacting medium in solar thermochemical applications. A review on the literature presented in Sections 2.1 and 2.2 reveals that a great deal of attention has been devoted to theoretical, experimental and numerical investigations on transport phenomena in conventional porous media featuring only one characteristic length-scale. Transport phenomena in multi-scale porous media have been addressed in few studies, which have been reviewed in Section 2.3. Finally, the research questions, the gaps in the literature, and the objective of this thesis are discussed in section 2.4.

Chapter 3
Fluid flow analysis

Fluid flow in dual-scale porous media is numerically investigated at the pore level. The model dual-scale porous medium consists of a packed bed of porous spherical particles. The void-space between the spherical particles represents the large-scale pores. The spherical particles are formed from three-dimensionally ordered macroporous (3DOM) media featuring small interconnected pores. To perform DPLS, traditional mass and momentum conservation equations for a fluid flowing through the medium are solved. The results are then used to calculate the permeability and Forchheimer coefficient of the dual-scale porous media. The permeability and Forchheimer coefficient of the 3DOM structures forming the spherical particles are numerically determined and implemented in the Darcy-level simulations. For this case, the volume-averaged and traditional conservation equations are, respectively, solved for the small-scale pores inside the spherical particles and large-scale pores between the particles. Finally, the results of Darcy-level simulations are compared with those of the DPLS.

3.1. Problem statement

Figure 3.1a illustrates the spherical particles containing 3DOM porous structures which are used in the model of the dual-scale porous packed bed. In the packed bed, the porous spherical particles ($2R = 1\,\text{mm}$) are arranged such that they create a body-centred cubic (BCC) packing arrangement, resulting in inter-particle pores of a much larger length-scale than contained in the particles. The length of the BCC unit cell is $L = \frac{4R}{\sqrt{3}} \approx 1.16\,\text{mm}$. One quarter of the BBC unit cell is used as a computational domain to reduce computational cost since it is symmetric (Figure 3.1b). The intra-particle region consists of 3DOM structures in which the solid ligaments are generated by subtracting an FCC packing arrangement from a

cube (Figure 3.1c). In the unit cell of the 3DOM structure with the edge length of a, the radius of the small particle (r) needs to be slightly greater than $\frac{\sqrt{2}}{4}a$ to generate interconnected pores. Thus, the greater the value of r compared to $\frac{\sqrt{2}}{4}a$ is, the bigger the windows between the small pores becomes (Figure 3.1c). In the packed bed of porous spherical particles, the values of R, L, and a remain constant for the numerical simulations. Three values 18, 18.5 and 19 μm are considered for r leading to 3DOM porosity of 0.78, 0.85 and 0.92, respectively. ANSYS DesignModeler [196] has been used to generate the structures shown in Figure 3.1. In addition, line 1 is defined in the computational domain as a location containing flow both in the inter- and intra-particle regions for further analysis after a solution has been found.

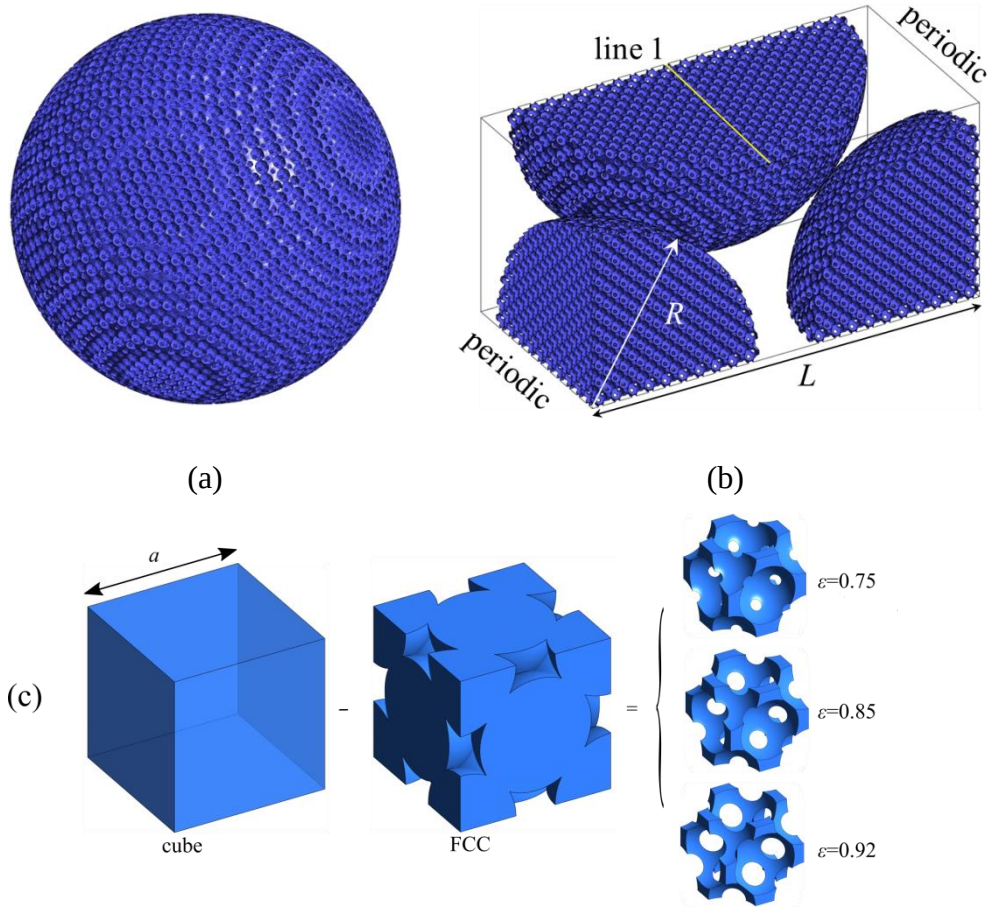

Figure 3.1. Packed bed of porous spherical particle, (a) 3DOM spherical particles, (b) computational domain, and (c) unit cells of 3DOM structures.

Before describing the numerical method for solving fluid flow in the dual-scale porous structure depicted in Figure 3.1, the reason for choosing the 3DOM structures as the model material is briefly discussed here. These structures have recently attracted attention of researchers due to their unique pore structure such as high specific surface area and high porosity. These features made them promising materials in applications including heterogeneous catalysis [197, 198], thermochemical reactors [199–201] and lithium ion batteries [202, 203]. 3DOM structures with open and interconnected pores have been successfully synthetised and tested in different catalytic cycles [197, 200, 204, 205]. Thus, a model of dual-scale porous medium consisting of a packed bed of 3DOM particles is considered due to its potential application in solar thermochemical reactors. The proposed structure simultaneously benefits from the unique characteristics of dual-scale porous media and 3DOM structures.

3.2. Methodology

In this section, the methodology used to perform direct pore-level simulations as well as Darcy-level simulations is presented. This includes the mass and momentum conservation equations at pore level and Darcy level, boundary and interface conditions, numerical method, and grid independency analysis.

Governing equations

For DPLS, the traditional conservation equations of mass and momentum are used for steady flow of an incompressible Newtonian fluid (air in this study):

$$\nabla \cdot \mathbf{v} = 0 \tag{3.1}$$

$$\rho_{\mathrm{f}} \nabla \cdot \left(\mathbf{vv} \right) = -\nabla p + \mu_{\mathrm{f}} \nabla^2 \mathbf{v} \tag{3.2}$$

where **v** and p are the velocity vector and the pressure, respectively. The parameters ρ_{f} and μ_{f}, respectively, define the fluid density and dynamic viscosity. In addition, simulations at the Darcy level are performed to make a comparison with the pore-level simulations. For Darcy-level simulations, the traditional mass and momentum equations, Eqs. (3.1) and (3.2), are solved for the big inter-particle pores, and the volume-averaged equations for mass and momentum are solved to model the fluid flow within the small pores of the spheres as below:

$$\nabla \cdot \left\langle \mathbf{v}_\mathrm{p} \right\rangle = 0 \tag{3.3}$$

$$\frac{\rho_\mathrm{f}}{\varepsilon} \nabla \cdot \left(\left\langle \mathbf{v}_\mathrm{p} \right\rangle \left\langle \mathbf{v}_\mathrm{p} \right\rangle \right) = -\varepsilon \nabla \left\langle p \right\rangle^\mathrm{f} + \mu_\mathrm{f} \nabla^2 \left\langle \mathbf{v}_\mathrm{p} \right\rangle - \frac{\varepsilon \mu_\mathrm{f}}{K} \left\langle \mathbf{v}_\mathrm{p} \right\rangle - \frac{\varepsilon \rho_\mathrm{f} c_\mathrm{F}}{\sqrt{K}} \left| \left\langle \mathbf{v}_\mathrm{p} \right\rangle \right| \left\langle \mathbf{v}_\mathrm{p} \right\rangle \tag{3.4}$$

where ε is the porosity of the 3DOM structure, $\left\langle \mathbf{v}_\mathrm{p} \right\rangle$ is the superficial average of the velocity inside the spherical particles, and $\left\langle p \right\rangle^\mathrm{f}$ is the intrinsic average of the pressure. The third and fourth terms on the right-hand side of Eq. (3.4) are the Darcy and Forchheimer terms, which, respectively, describe the microscopic viscous and inertial forces caused by interaction between the fluid and solid constituents. In these terms, the permeability K and the drag coefficient c_F are required as inputs to model the fluid flow in the porous region. In this study, they are numerically calculated for the 3DOM unit cells.

Boundary and interface conditions

For pore-level simulations, the no-slip boundary condition is applied on the solid walls. For both direct pore-level and Darcy-level simulations, the periodic boundary conditions are applied on the front and back faces of the domain to obtain the fully developed velocity field [206]. The periodic boundary condition enforces identical velocity profiles on the front and back walls of the domain. The symmetry boundary condition is applied on the lateral faces of the domain (Figure 3.1b). The pressure field is then obtained by post-processing the results of the simulations. Interface conditions are needed for Darcy-level simulations to couple the mass and momentum transfer between the homogenous fluid flowing in the inter-particle region and the fluid flowing in the porous spherical particles. For the interface between these two regions, the conditions of continuity of velocity and interfacial stress are applied as [120, 207, 208]:

$$\mathbf{v} = \left\langle \mathbf{v}_\mathrm{p} \right\rangle \tag{3.5}$$

$$\mu_\mathrm{f} \left(\frac{\partial u}{\partial y} + \frac{\partial v}{\partial x} \right) = \frac{\mu_\mathrm{f}}{\varepsilon} \left[\frac{\partial \left\langle u_\mathrm{p} \right\rangle}{\partial y} + \frac{\partial \left\langle v_\mathrm{p} \right\rangle}{\partial x} \right]_\mathrm{p} \tag{3.6}$$

$$\mu_\mathrm{f} \left(\frac{\partial w}{\partial y} + \frac{\partial v}{\partial z} \right) = \frac{\mu_\mathrm{f}}{\varepsilon} \left[\frac{\partial \left\langle w_\mathrm{p} \right\rangle}{\partial y} + \frac{\partial \left\langle v_\mathrm{p} \right\rangle}{\partial z} \right]_\mathrm{p} \tag{3.7}$$

$$\mu_{\mathrm{f}}\left(\frac{\partial w}{\partial x}+\frac{\partial u}{\partial z}\right)=\frac{\mu_{\mathrm{f}}}{\varepsilon}\left[\frac{\partial\left\langle w_{\mathrm{p}}\right\rangle}{\partial x}+\frac{\partial\left\langle u_{\mathrm{p}}\right\rangle}{\partial z}\right]_{\mathrm{p}} \tag{3.8}$$

$$-p=-\left\langle p\right\rangle^{\mathrm{f}} \tag{3.9}$$

where u, v and w are the *x*-, *y*- and *z*- components of the velocity vector, respectively. The subscript p refers to the porous spherical particles. In Eq. (3.5), it is assumed that at the nominal interface, the velocity on inter-particle side immediately becomes equivalent to the superficial average velocity on intra-particle side. In addition, Eqs. (3.6)–(3.8) assume that all the components of the total stress on the inter-particle side are equivalent to those of the intrinsically-averaged stress on the intra-particle side. A fraction ε of the total stress on the inter-particle side of the interface is carried in the fluid constituent of the porous domain of the intra-particle side, with the remainder carried by the solid constituent. In Eq. (3.9), we force the pressure on the inter-particle side of the interface to be equivalent to the intrinsically-averaged pressure on the intra-particle side. By implementing Eqs. (3.6)–(3.9), we enforce that the viscous portion of the normal stress and the portion of the normal stress due to pressure are continuous at the interface.

Numerical method, grid independency and validation

The three-dimensional computational domain is discretised using tetrahedral cells. The CFD code ANSYS FLUENT 17.1 is used to solve the governing equations using the finite volume method [209]. The velocity–pressure coupling is resolved by the SIMPLE (Semi-Implicit Method for Pressure Linked Equations) algorithm. The advection terms are discretised using the second order upwind scheme [210]. The convergence is achieved when the residuals reach 10^{-6} and 10^{-8} for the continuity and momentum equations, respectively. For periodic boundary condition, a constant mass flow rate is considered in the computational domain. Once the simulation is converged, the flow field and pressure drop are calculated by post-processing the results of the simulations. Figure 3.2 shows the meshing of the computational domain for DPLS and Darcy-level simulations. For the case of DPLS, finer meshing is implemented near the solid walls due to the presence of large velocity gradients. For the case of Darcy-level simulations, finer meshing is implemented near the interface between inter-particle region and porous spherical particles due to the presence of large velocity gradients.

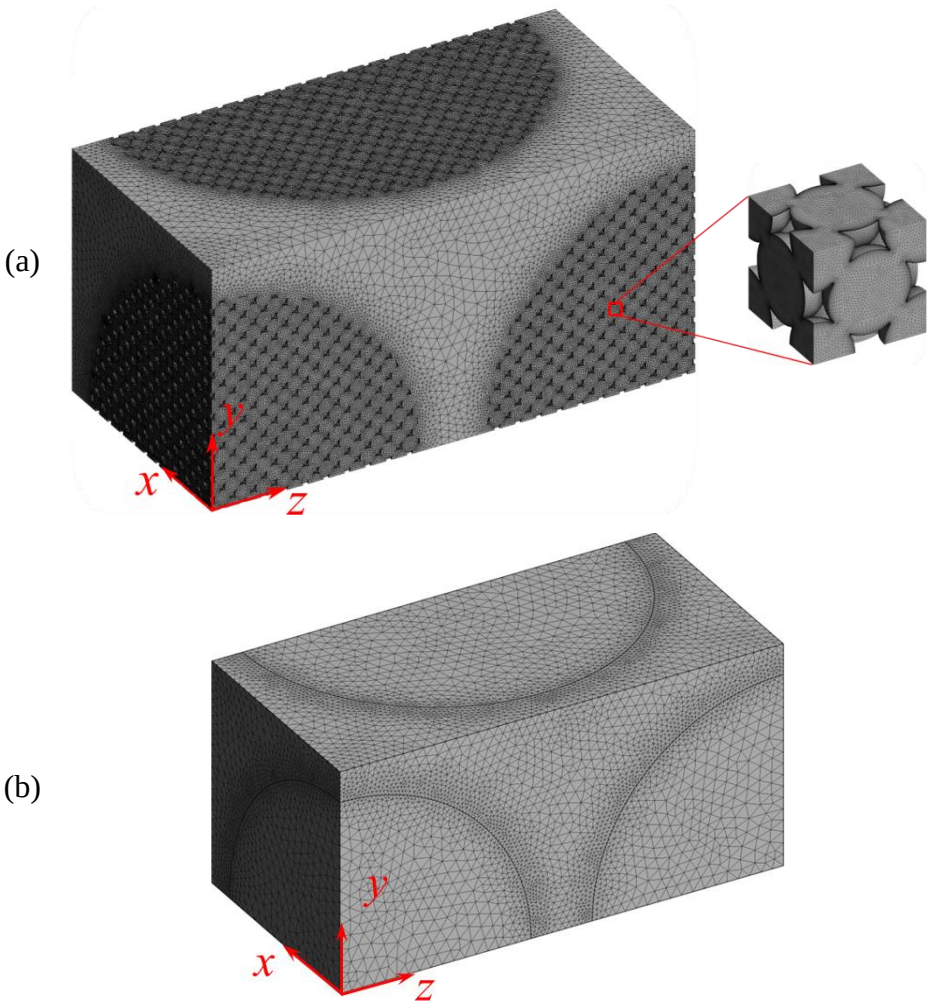

Figure 3.2. Meshing of the computational domain for (a) DPLS and (b) Darcy-level simulations.

Grids with different numbers of mesh elements are examined to ensure the grid independency. The total number of mesh elements for the dual-scale porous structures was varied from approximately 10^7 to 2.5×10^7. The velocity magnitude at different points (P1 in inter-particle region, P2 in intra-particle region, and P3 at the vicinity of inter-particle and intra-particle regions) as well as the pressure drop per unit length of the packed bed have been selected as the sample parameters ϕ for which the grid independency is examined. The relative error e_r of the parameter ϕ under examination is calculated by:

$$e_r = \frac{\left|\phi - \hat{\phi}\right|}{\hat{\phi}} \tag{3.10}$$

where $\hat{\phi}$ represents the value of the parameter obtained using the results of the simulation with the highest number of mesh elements. Figure 3.3a to Figure 3.3d show the mesh independency analysis for the selected parameters. It is observed that by increasing the number of mesh elements to approximately 1.9×10^7, the value of e_r for all the mentioned parameters is less than 3%.

The numerical results obtained in current study are benchmarked against the experimental results reported by Leong et al. [125] for porous graphite foam in order to validate the solution approach. Comparison verifies the consistent implementation of Darcy and Forchheimer terms in the solver, as indicated by the agreement shown in Figure 3.3e. In addition, to validate the numerical method, the pressure drop per unit length is calculated in terms of Reynolds number using the results of pore-level simulations. The numerical results are then compared with the experimental data reported by Yang et al. [126] for packed beds of solid particles (single-scale porosity) with different packing arrangements—simple cubic (SC), body-centred cubic (BCC) and face-centred cubic (FCC). The comparison presented in Figure 3.3f demonstrates close agreement. The two validation approaches corroborate the consistency of the solution approach for both pore- and Darcy-level simulations.

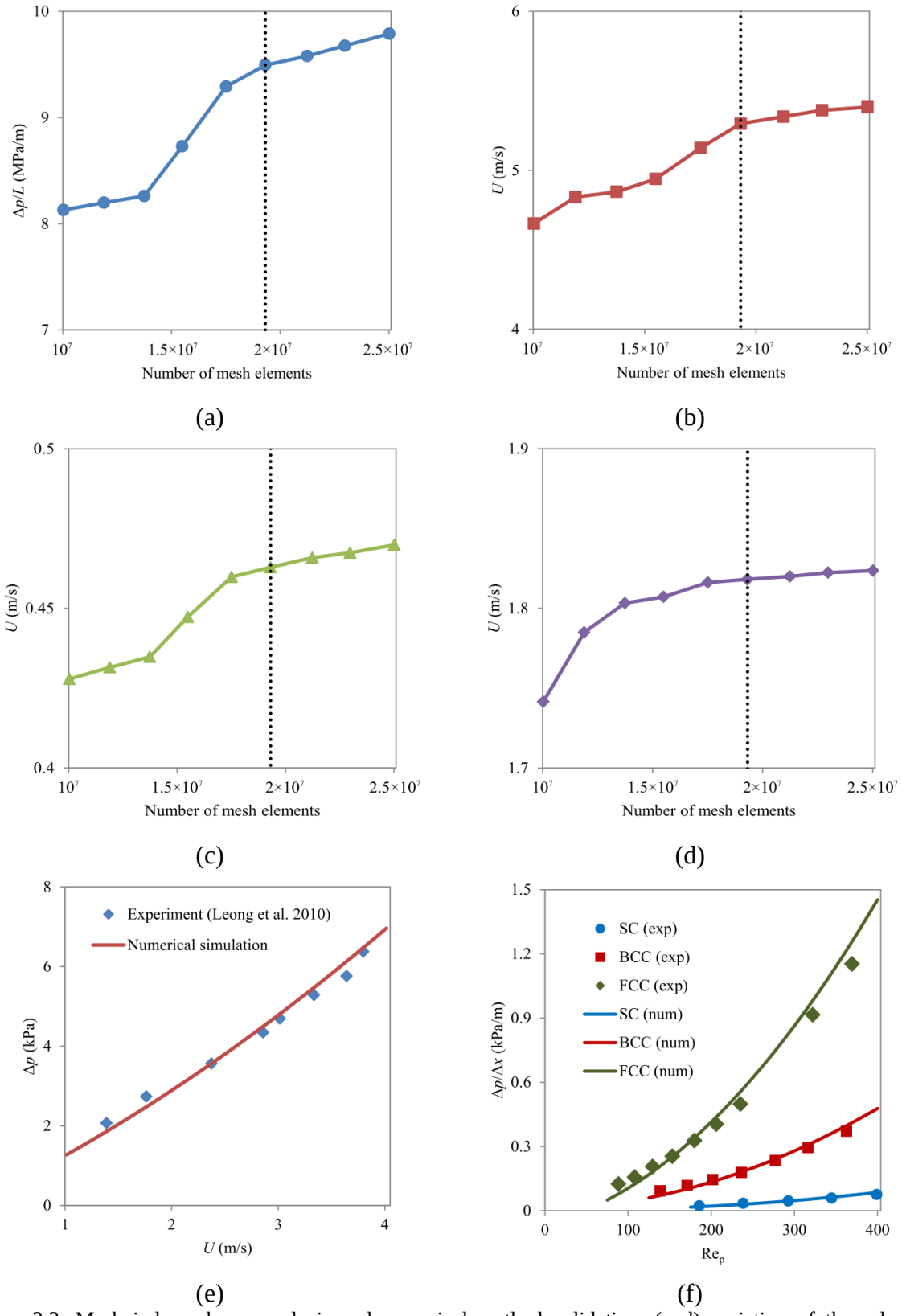

Figure 3.3. Mesh independency analysis and numerical method validation: (a–d) variation of the selected parameters with mesh refinement and (e, f) benchmarking of the solver with experimental results in [125, 126].

3.3. Direct pore-level simulations

Direct pore-level simulations are performed to study the fluid flow in dual-scale porous media consisting of packed beds of 3DOM spherical particles. The effect of changing porosity of the 3DOM structure on the flow characteristics of the packed bed is systematically studied for Reynolds numbers ranging from zero to 265. Figure 3.4 shows the velocity vectors in the in packed bed of 3DOM spherical particles at Re_p=100 for three different values of 3DOM porosity. The superficial average of the velocity is used to define $\mathrm{Re}_\mathrm{p} = \rho \langle v \rangle d_\mathrm{p} / \mu$ in the packed bed. It can be qualitatively seen that as the porosity of the 3DOM structures in the spherical particles increases, more fluid passes through intra-particle region (small pores) and, less fluid flows in the spaces between the spheres.

Figure 3.5 shows the velocity magnitude *U* for line 1 (see Figure 3.1b) at Re_p=100 for three different values of 3DOM porosity. At $\varepsilon = 0.78$, it can be seen that most of the fluid flows through the inter-particle region such that the average of the velocity in the inter-particle and intra-particle regions are 3.15 m/s and 0.44 m/s, respectively. By increasing the porosity of the 3DOM structures, the flow resistance is reduced, and more fluid passes through the 3DOM particles. In addition, it seems that changing the porosity of the 3DOM structures has a nonlinear effect on the amount of fluid flowing in the intra-particle pores, such that increasing the value of 3DOM porosity from 0.78 to 0.85 and from 0.85 to 0.92 increases the averaged velocity in the small pores by approximately 81 and 31%, respectively.

To better visualise the fluid flow inside the dual-scale porous structures, three control boxes are placed at different locations of the medium as shown in Figure 3.6: one inside a 3DOM sphere, and two encompassing both part of a 3DOM sphere and inter-particle pore.

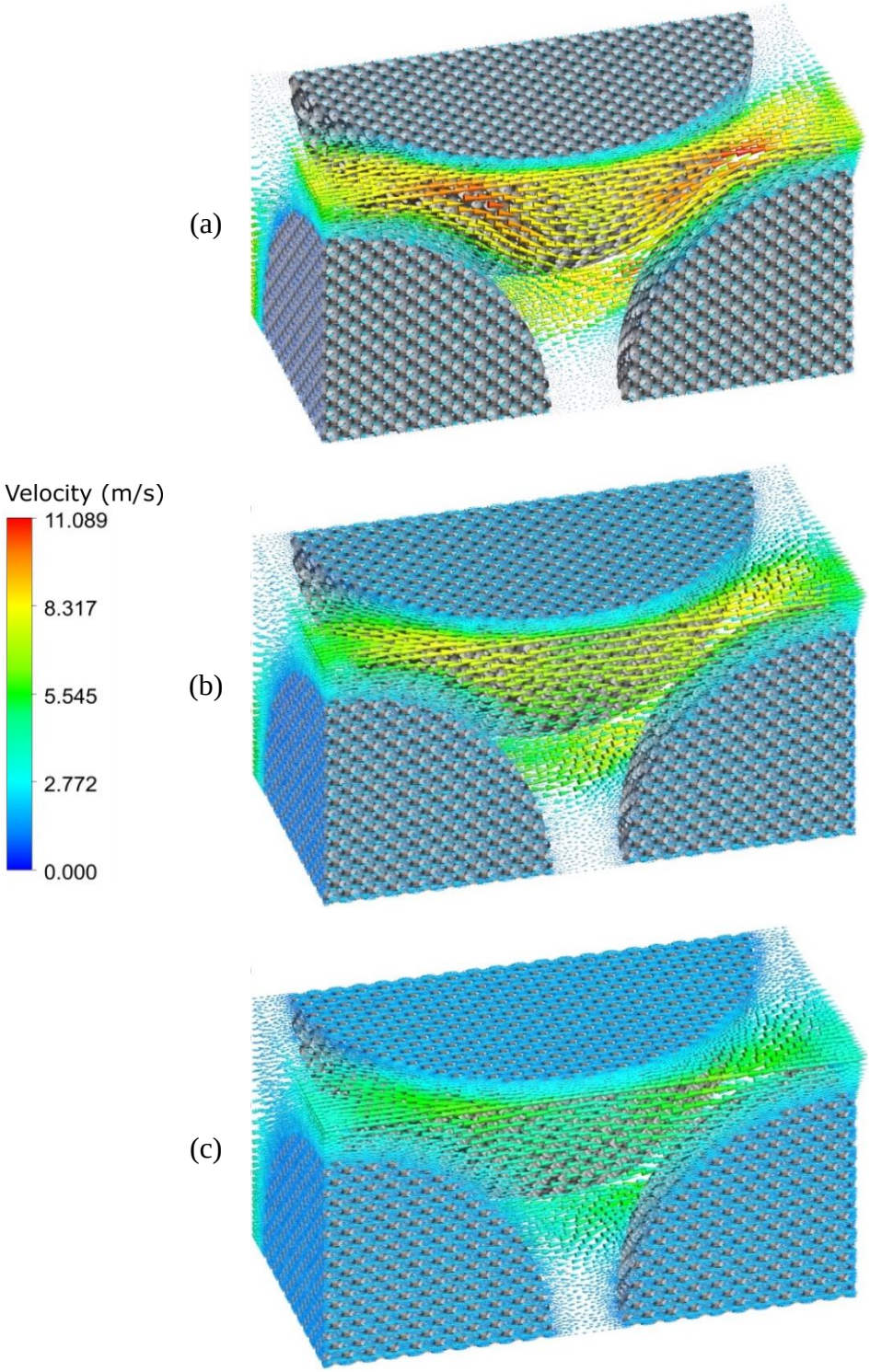

Figure 3.4. Velocity vectors in the in packed bed of 3DOM spherical particles at Re_p=100 for (a) $\varepsilon = 0.78$, (b) $\varepsilon = 0.85$, and (c) $\varepsilon = 0.92$.

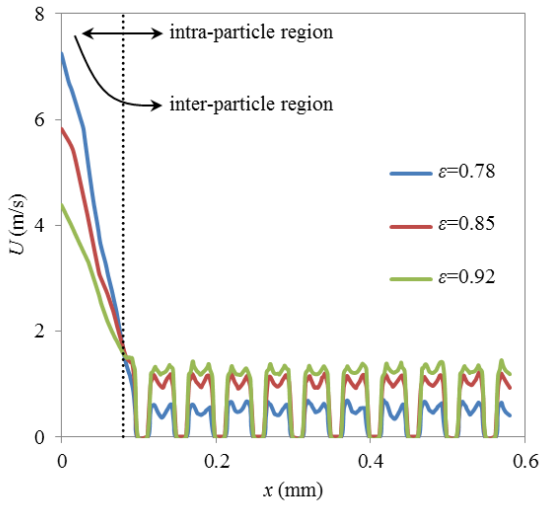

Figure 3.5. Velocity magnitude for line 1 at Re_p=100 for different values of 3DOM porosity.

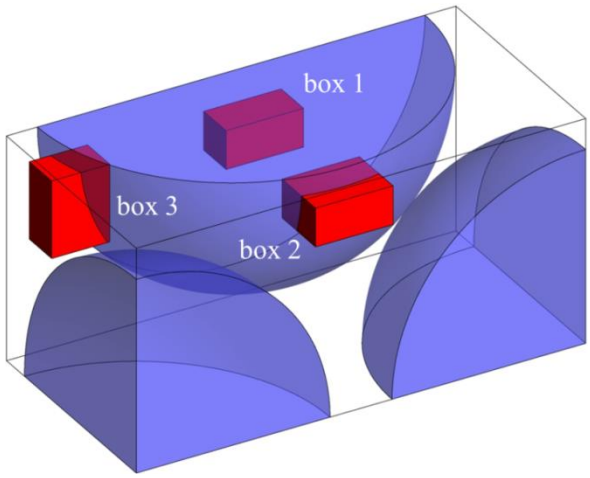

Figure 3.6. Location of three boxes for visualising the pore-level velocity field.

The velocity vectors in three control boxes, depicted in Figure 3.6, are illustrated in Figure 3.7 at Re_p=100 for three values of 3DOM porosity. For the box inside the 3DOM sphere (Figure 3.7a), increasing the porosity of the 3DOM structures leads to more uniform velocity distribution and increases the velocity in the intra-particle region. At $\varepsilon = 0.78$, the throats between the small pores are very tight (Figure 3.1c). This forces the fluid to pass through a narrow path, resulting in the local maximum velocity occurring there (the red velocity vectors). By increasing the porosity of the 3DOM structures, the throats between the small pores widen. Thus, the fluid passes through with less resistance and a more uniform velocity distribution is observed. Similar observations can be made for the fluid flow inside the small pores in Figure 3.7b and Figure 3.7c. In addition, it can be seen in Figure 3.7c that at $\varepsilon = 0.78$, the fluid seems to mostly bypass the 3DOM spheres. This can be again attributed to the fact that the throats in the 3DOM structures are rather tight, which creates significant flow resistance. However, as the porosity of the 3DOM structures increases and the throats between the small pores become wider, the velocity vectors at the vicinity of the big pores and small pores gradually shift their direction towards the 3DOM structure rather than away from the structure. The 3DOM structure with wider throats between the pores creates less amount of resistance for the flow, and the fluid can pass through the structure more freely.

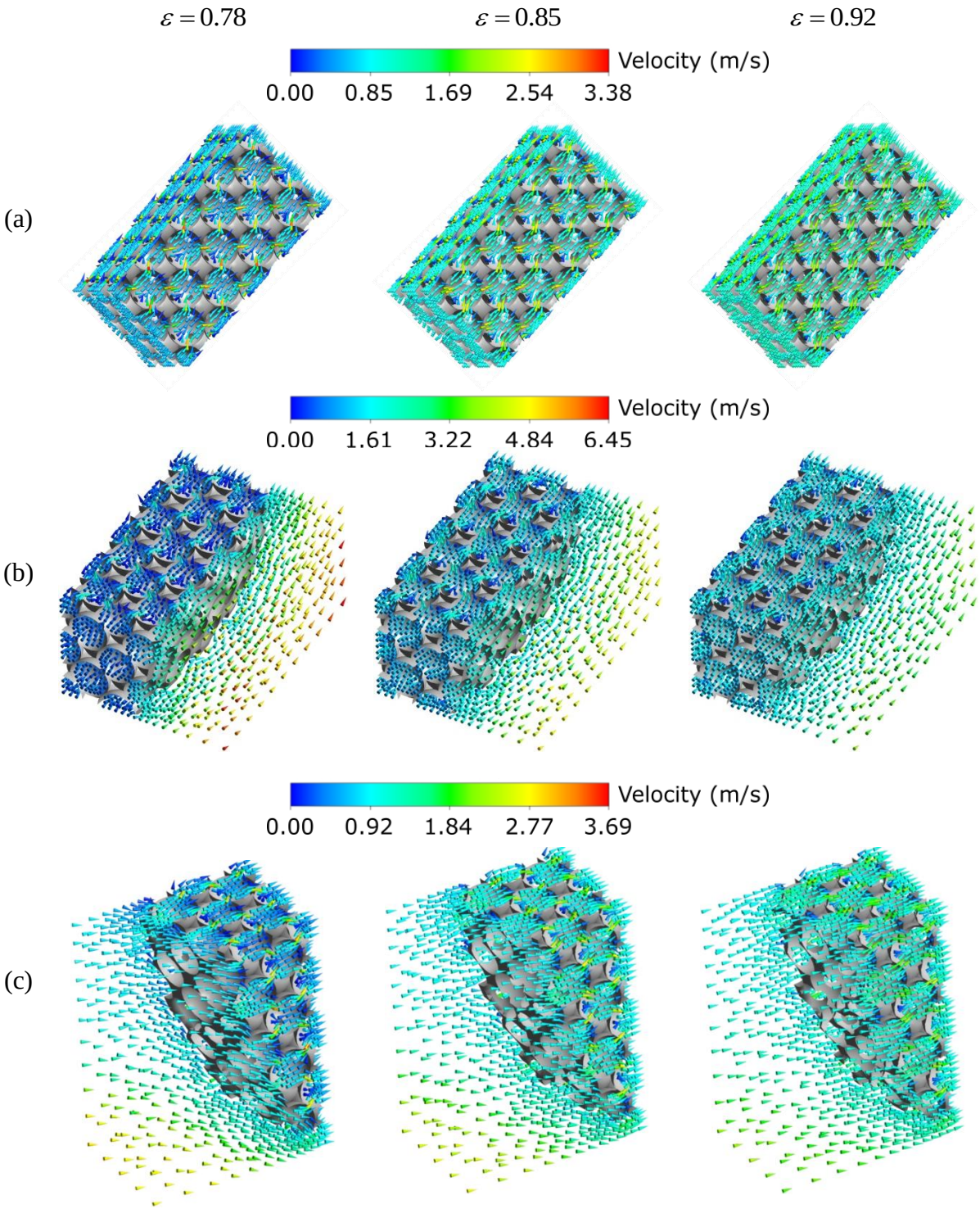

Figure 3.7. Pore-level velocity vectors in the packed bed unit cell at different values of 3DOM structure porosity and Re_p=100 for (a) box 1, and (b) box 2, and (c) box 3.

3.4. Darcy-level simulations

Now that direct pore-level simulations have been performed, Darcy-level simulations are carried out to compare the results with those of the DPLS. Pore-level simulations are performed on the unit cell of the 3DOM structures (Figure 3.1c), to calculate the effective flow properties—the permeability and Forchheimer coefficient. Then, the calculated effective properties are considered in the volume-averaged momentum conservation equation, Eq. (3.4), to model the fluid flow in the porous spherical particles of the packed bed. Thus, instead of directly resolving the small pores, the spheres of the BCC packed bed are considered as lumped media with the numerically-calculated effective permeability and Forchheimer coefficient of the 3DOM unit cells. Figure 3.8 shows the computational domain and meshing of the three 3DOM unit cells. Periodic boundary conditions are applied on the front and back faces in *z* direction (fluid flow direction), and symmetry boundary conditions are considered for the lateral surfaces.

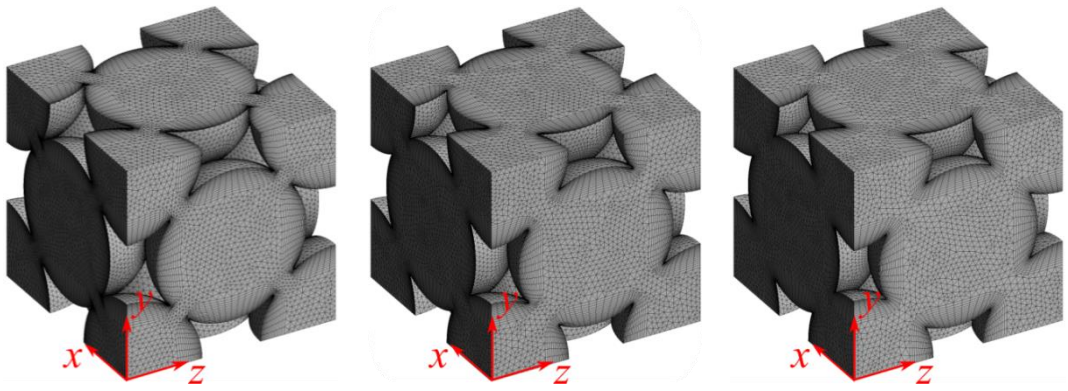

$\varepsilon = 0.78$ $\varepsilon = 0.85$ $\varepsilon = 0.92$

Figure 3.8. Computational domain and meshing of the three 3DOM structures.

Figure 3.9 shows the pressure drop per unit length in terms of superficial average of the velocity in the 3DOM unit cells $\langle v \rangle_{3\mathrm{DOM}}$. As the porosity of 3DOM structure increases and the throats between the small pores widen, the resistance of the structure to fluid flow, and consequently, the pressure drop decreases in the 3DOM unit cell.

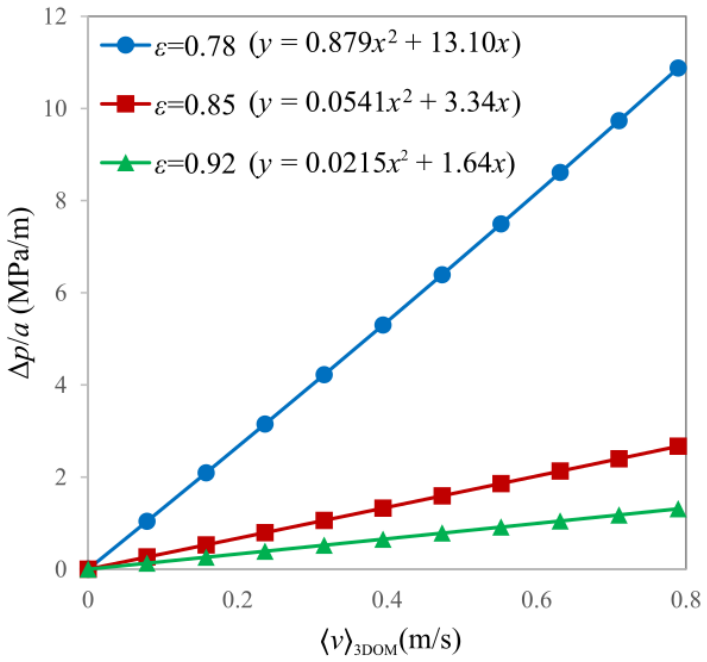

Figure 3.9. Pressure drop per unit length as a function of superficial velocity for the three 3DOM unit cells.

Pressure data from the pore-level simulations of the fluid flow in the 3DOM unit cells are now used to derive permeability (K) and Forchheimer coefficient (c_F) of the 3DOM structures using the classical Darcy–Forchheimer law for porous media [38, 111, 211]:

$$\frac{\Delta p}{a} = \frac{\mu_f}{K}\langle v\rangle_{3DOM} + \frac{\rho_f c_F}{\sqrt{K}}\langle v\rangle_{3DOM}^2 \tag{3.11}$$

As shown in Figure 3.9, the numerical data for pressure drop per unit length of the 3DOM structures in terms of unit cell velocity are fitted in second-order polynomial models. By matching the second-order polynomial models into the Darcy–Forchheimer law in Eq. (3.11), the effective permeability and Forchheimer coefficient of the 3DOM structures can be calculated. It should be noted that the R^2 values for the second-order polynomial models presented in Figure 3.9 are 1. Table 3.1 lists the calculated permeability and Forchheimer coefficient for three 3DOM structures. It can be seen that increasing the porosity of the 3DOM structures results in increase in the permeability and decrease in the Forchheimer coefficient. This is due to the nonlinearity of pressure drop in terms of velocity for fluid flow in porous media. The nonlinearity is attributed to the inertia forces when the direction of the fluid flow changes frequently in a medium [212]. When a medium is more tortuous, the flow is forced to change its direction due to the curvature of the pores, leading to higher inertia

forces. As can be seen in Figure 3.7a, the throats between the small pores widen by increasing the porosity of the 3DOM structures, and thus, a more uniform velocity distribution is observed. Therefore, the flow pattern experiences less curvature in the pores, leading to less inertia forces and lower values of Forchheimer coefficient.

Table 3.1. Permeability and Forchheimer coefficient for the 3DOM structures.

ε	K (m^2)	c_F
0.78	1.37×10^{-12}	0.84
0.85	5.36×10^{-12}	0.10
0.92	1.09×10^{-11}	0.06

For Darcy-level simulations, the effective permeability and Forchheimer coefficient of the 3DOM structures presented in Table 3.1 are used in the Eqs. (3.3) and (3.4) to model the fluid flow in the 3DOM particle structures.

Figure 3.10 shows the pressure drop per unit length of the BCC packed bed in terms of superficial average of velocity in the packed bed $\langle v \rangle$ for DPLS and Darcy-level simulations. It can be seen that the Darcy-level simulations overestimate the pressure drop of the dual-scale packed bed for all cases. One reason can be the fact that in Darcy-level simulations, the effective permeability and Forchheimer coefficient calculated for the 3DOM unit cell are forced for the whole domain of the spherical particles. However, periodic boundary conditions with a fully developed flow field were considered when determining these coefficients. In the DPLS, the fluid requires to flow in a couple of consecutive 3DOM unit cells at the interface of the two regions in order to develop, leading to the apparent disagreement. Therefore, the effective permeability and Forchheimer coefficient calculated for the 3DOM unit cells may not accurately model the viscous and inertia forces occurring in the small pores in the vicinity of the two regions.

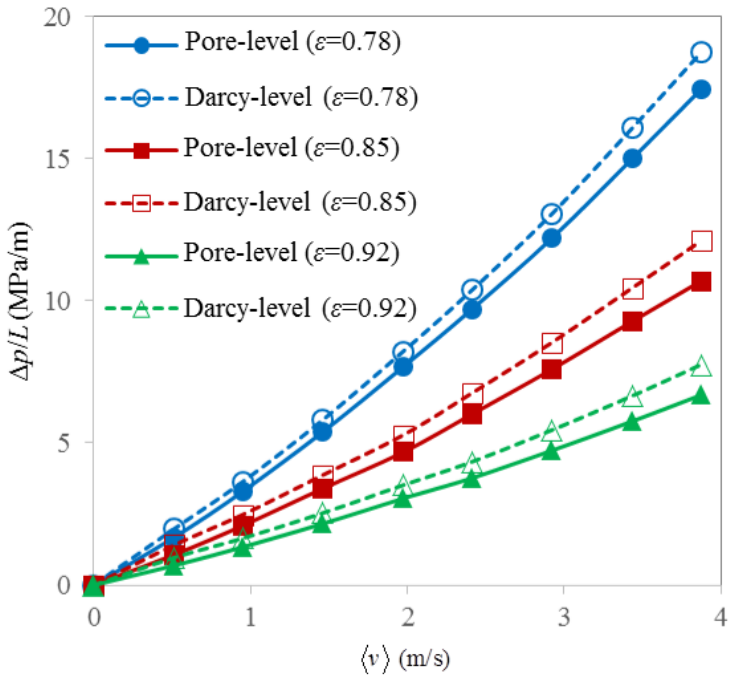

Figure 3.10. Pressure drop per unit length in terms of superficial average of the velocity in the packed bed.

In addition to the interface conditions, another possible reason for the observed discrepancy between the pore- and Darcy-level simulations can be related to the flow patterns in the inter-particle regions. Figure 3.11 shows the velocity vectors in the region between two porous spheres obtained using DPLS and Darcy-level simulations for example at Re_p=200. The Darcy-level simulations show vortex structures between the porous particles. Such vortex patterns were also observed in the study performed by Yang et al. [56] for a packed bed of solid spherical particles. However, for the case of DPLS, the fluid flows smoothly in the inter-particle regions. This pattern observed in the inter-particle regions for the case of Darcy-level simulations is another reason for Darcy-level simulations overestimating the pressure drop compared to DPLS. Note that as the porosity of the 3DOM structure increases, the trend of pressure gradient in the packed bed as a function of velocity becomes less quadratic, showing that the necessity of considering the Forchheimer term becomes less important to model the fluid flow at macro-scale.

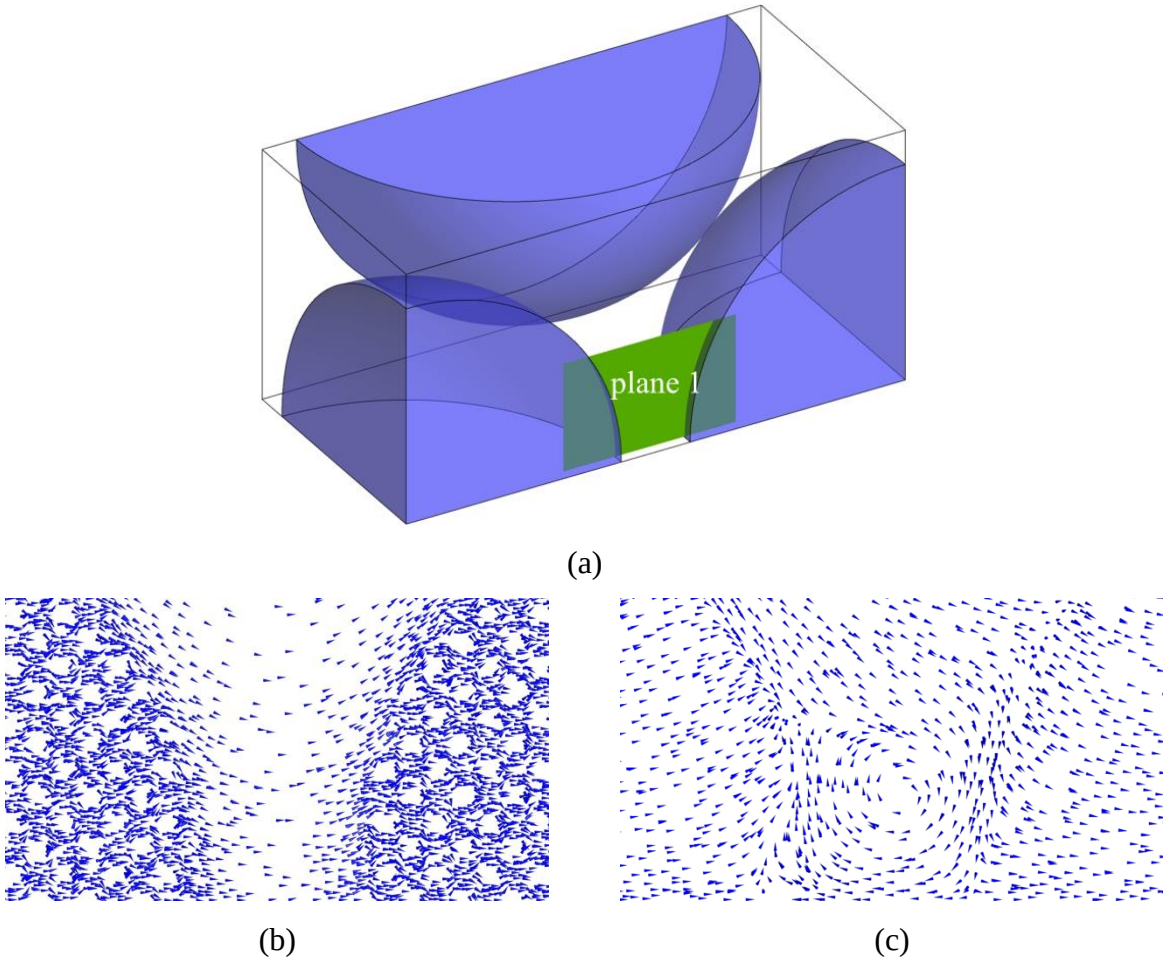

Figure 3.11. Velocity field analysis in the region between two porous spheres at Re_p=200: (a) control plane for post-processing the velocity field, (b) velocity vectors for DPLS, and (c) velocity vectors for Darcy-level simulations.

Table 3.2 compares the permeability and Forchheimer coefficient of the BCC dual-scale packed bed, K_{dual} and $c_{F,dual}$, respectively, obtained using the results of DPLS and Darcy-level simulations for Reynolds number in the range 0–265. The results of the pressure drop per unit length of the packed bed in terms of superficial average of the velocity in the packed bed are fitted in second-order polynomial models. Then the effective permeability and Forchheimer coefficient of the dual-scale packed bed are calculated by matching the second-order polynomial models into Darcy–Forchheimer law in Eq. (3.11) for the cases of DPLS and Darcy-level simulations. It can be seen that by increasing the 3DOM porosity, the error between the effective properties calculated using DPLS and Darcy-level simulations increases. This can again be attributed to the fact that, as the throats between the small pores

widen and the porosity of 3DOM structure increases, the flow can penetrate the 3DOM particles more significantly. Thus, the fluid requires more numbers of 3DOM unit cells at the interface in order to fully develop similarly to the fully-developed velocity field obtained using periodic boundary condition. For the case of Darcy-level simulations, the effective coefficients are applied for the whole domain of the spheres. However, since it takes more depth for the flow to fully develop inside the 3DOM structures by increasing the 3DOM porosity, the real region—for which the effective coefficients are valid—becomes smaller compared to the whole sphere. That is the reason why researchers have investigated more realistic interface conditions which take into account the flow transition between the homogeneous and porous regions instead of considering those presented in Eqs. (3.5)–(3.8) [123]. This issue becomes even more important since it was reported that the interface conditions depend on the structure, the flow direction, the Reynolds number, the nonuniformity in the arrangement, and tortuosity of porous medium [165].

Table 3.2. Permeability and Forchheimer coefficient BCC dual-scale packed bed.

	DPLS		Darcy-level simulations			
	K_{dual} (m^2)	$c_{F,dual}$	K_{dual} (m^2)	Error (%)	$c_{F,dual}$	Error (%)
$\varepsilon = 0.78$	5.54×10^{-12}	0.64	5.24×10^{-12}	5.31	0.68	6.37
$\varepsilon = 0.85$	8.81×10^{-12}	0.47	7.99×10^{-12}	9.24	0.52	10.63
$\varepsilon = 0.92$	1.35×10^{-11}	0.31	1.20×10^{-11}	11.26	0.35	12.16

Alazmi and Vafai [123] analysed different types of interfacial conditions between a porous medium and a fluid layer. They observed that, in general, application of different types of interfacial conditions considerably affect the velocity field. They concluded that the discrepancies between the different types of interfacial conditions can be more significant at higher Reynolds numbers and/or Darcy numbers. However, their study lacks experimental validation, and it is not clearly stated which type of interfacial conditions leads to more accurate results compared to experiments or pore-level simulations. Therefore, the accuracy of the different types of interfacial conditions investigated in their study is unknown. Another important issue is that the physical configuration used in their study is a very simple two-dimensional configuration consisting of a porous medium and a fluid layer, such that the normal component of velocity at the interface is always zero. However, in a real dual-scale porous structure, the tortuous flow channels lead to the three-dimensional flow patterns. Therefore, the angles at which the fluid flow in the big pores reaches the small pores are

different throughout the medium. Therefore, at this stage, it is difficult to judge which type of interfacial conditions leads to more accurate results. Thus, it is assumed that the well-established interface conditions introduced in Eqs. (3.5)–(3.8) suffice.

3.5. Summary

The fluid flow in a dual-scale porous medium consisting of a packed bed of 3DOM spherical particles was numerically investigated at the pore level and Darcy level. The effect of different 3DOM structures with different porosities was analysed. It was observed that the size of the throats between the small pores considerably affects the fluid flow patterns in the inter- and intra-particle regions as well as the region between them. The permeability and Forchheimer coefficient of the packed bed featuring dual-scale porosity were calculated using the results of DPLS and Darcy-level simulations. It was observed that the Darcy-level simulations overestimate the pressure drop in the dual-scale porous packed bed compared to the DPLS, in particular for 3DOM structures with higher values of porosity. However, Darcy-level simulations can provide acceptably accurate results using much less computational resources compared to DPLS. For the Darcy-level simulations, the average of the error in predicting effective flow properties compared to DPLS was approximately 7%. In future works, more accurate interface conditions need to be modelled to be used in Darcy-level simulations. which take into account the transition between the porous and homogenous regions as well as the effect of flow direction and velocity at the interface. This leads to more accurate results obtained using the Darcy-level simulations which are computationally much less expensive compared to DPLS. The results of this chapter for fluid flow in dual-scale porous media will be used in Chapter 5, since the convection term is considered for the heat transfer in dual-scale porous media. In the following chapters, the heat transfer in dual-scale porous media is theoretically and numerically analysed.

Chapter 4

Theoretical development of conductive–convective heat transfer model

In this chapter, the mathematical model of heat transfer in a dual-scale porous medium is developed. A dual-scale porous structure is introduced along with the associated length-scales, followed by the energy conservation equation and boundary conditions at the smallest scale under study. The volume-averaging procedure is applied to the terms appearing on the conductive–convective energy conservation equation. This procedure results in the introduction of the up-scaled energy equation along with the effective coefficients which take into account the heat transfer feature of small-scale in the up-scaled equation. Finally, the closure problems are introduced, which are solved in the next chapter to determine the effective heat transfer coefficients for given cases of dual-scale porous media.

4.1. Dual-scale porous structure

Figure 4.1 shows a schematic representation of a two-zone dual-scale porous medium. Three length-scales are considered:

1. Level A: a micro-scale level at which VAM is applied over volume V_A consisting of fluid and solid phases denoted as β and σ, respectively. The length-scales for this level are l_β and l_σ, where $l_\beta \approx l_\sigma$.
2. Level B: a meso-scale level at which VAM is applied over volume V_B consisting of regions η and ω. The length-scales for this level are l_η and l_ω, where $l_\eta \approx l_\omega$.

3. Level C: a macro-scale level at which effective transport equations with effective transport properties are used without any further volume averaging. The length-scale for this level is L_c.

The constraints for the dual-scale porous medium are $\left(l_\beta, l_\sigma\right)_\eta < \left(l_\beta, l_\sigma\right)_\omega$ (or vice versa) and $\left(l_\beta, l_\sigma\right)_{\eta,\omega} \ll l_\eta, l_\omega \ll L_c$. In addition, we consider that in the system illustrated in Figure 4.1, the σ-phase represents a rigid, impermeable solid phase, and the β-phase represents a Newtonian fluid. The parameter ψ in Figure 4.1 is the general scalar transport variable. It specifically has the meaning of temperature (T) in the present study of the conductive–convective heat transfer problem. The transport variable ψ is first up-scaled from level A to level B by its volume-averaging in volume V_A resulting in $\langle\psi\rangle^\omega$ or $\langle\psi\rangle^\eta$. Next, the transport variables at level B, $\langle\psi\rangle^\omega$ and $\langle\psi\rangle^\eta$, are up-scaled to level C by their volume-averaging in volume V_B, resulting in $\{\langle\psi\rangle\}$.

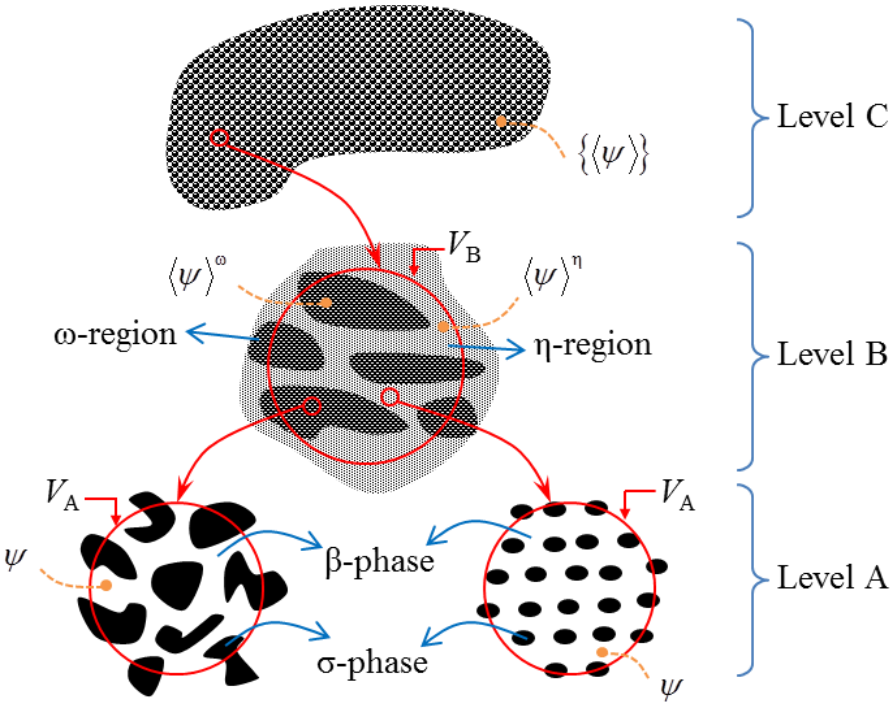

Figure 4.1. Schematic representation of a dual-scale porous medium.

4.2. Model assumptions

Now that the dual-scale porous media and the associated length-scales are defined, it is convenient to present all the available up-scaling strategies as shown in Figure 4.2. In this figure, LTE and LTNE represent the local thermal equilibrium and local thermal non-equilibrium assumptions, respectively. LTE is used when it can be assumed that the one phase or one region is in thermal equilibrium with the other phases or regions existing in its close vicinity. On the other hand, LTNE is used when it cannot be assumed that the one phase or one region is in thermal equilibrium with the other phases or regions existing in its close vicinity. This means that the convective heat transfer between the phases or heat exchange between the regions should be considered. The four available strategies for up-scaling energy transport in a dual-scale porous medium are as below:

- The first strategy, least complex scenario, is when we assume $\left(\left(\mathrm{LTE}\right)_{\beta\leftrightarrow\sigma}\right)_{\eta,\omega}$ for volume averaging over V_A, and $\left(\mathrm{LTE}\right)_{\eta\leftrightarrow\omega}$ for volume averaging over V_B. In this case, LTE assumption is made between β- and σ-phases in both η- and ω-regions when up-scaling from level A to B. Then, LTE assumption is made between η- and ω-regions during the up-scaling procedure from level B to C. Thus, one-equation model will be derived, which contains the effective coefficients.
- The second strategy is when we assume $\left(\left(\mathrm{LTE}\right)_{\beta\leftrightarrow\sigma}\right)_{\eta,\omega}$ for volume averaging over V_A, and $\left(\mathrm{LTNE}\right)_{\eta\leftrightarrow\omega}$ for volume averaging over V_B. In this case, LTE assumption is made between β- and σ-phases in both η- and ω-regions when up-scaling from level A to B. Then, LTNE assumption is made between η- and ω-regions during the up-scaling procedure from level B to C. Thus, two-equation model will be derived, which contains the effective coefficients including the heat exchange coefficient between the regions. If the heat exchange coefficient between the regions—which actually couples the two equations together—is assumed zero in this case, the situation will be the same as the first strategy.
- The third strategy is when we assume $\left(\left(\mathrm{LTE}\right)_{\beta\leftrightarrow\sigma}\right)_{\eta}$ and $\left(\left(\mathrm{LTNE}\right)_{\beta\leftrightarrow\sigma}\right)_{\omega}$ for volume averaging over V_A, and proceed with volume averaging over V_B. Thus, when up-

scaling from level A to B, we assume LTE between β- and σ-phases in η-region and LTNE between β- and σ-phases in ω-region, and then, continue the up-scaling procedure from level B to C. For up-scaling from level A to B in ω-region, the convective heat transfer between β- and σ-phases is taken into account, leading to the introduction of a convective heat transfer coefficient which will be up-scaled during the volume averaging over V_B. In this case, three-equation model will be derived (one for energy transport in β-phase of ω-region, one for energy transport in σ-phase of ω-region, and one for energy transport in η-region) along with the effective coefficients. If the convective heat transfer coefficient between β- and σ-phases in ω-region—which actually couples two of the equations related to ω-region together—is assumed zero in this case, the situation will be the same as the second strategy.

- The fourth strategy, the most complex scenario, is when we assume $\left(\left(\text{LTNE}\right)_{\beta\leftrightarrow\sigma}\right)_{\eta,\omega}$ for volume averaging over V_A, and proceed with volume averaging over V_B. Thus, when up-scaling from level A to B, we assume LTNE between β- and σ-phases in both η- and ω-regions, and then, we continue up-scaling process from level B to C. For the up-scaling from level A to B in both η- and ω-regions, the convective heat transfer between β- and σ-phases is taken into account, leading to the introduction of two convective heat transfer coefficients which will be up-scaled during the volume averaging over V_B. In this case, four-equation model will be derived (one for energy transport in β-phase of ω-region, one for energy transport in σ-phase of ω-region, one for energy transport in β-phase of η-region, and one for energy transport in σ-phase of η-region) along with the effective coefficients. If the convective heat transfer coefficient between β- and σ-phases in η-region—which actually couples two of the equations related to ω-region together—is assumed zero in this case, the situation will be the same as the third strategy. If the convective heat transfer coefficients between β- and σ-phases in both η- and ω-regions are assumed zero in this case, the situation will be the same as the second strategy.

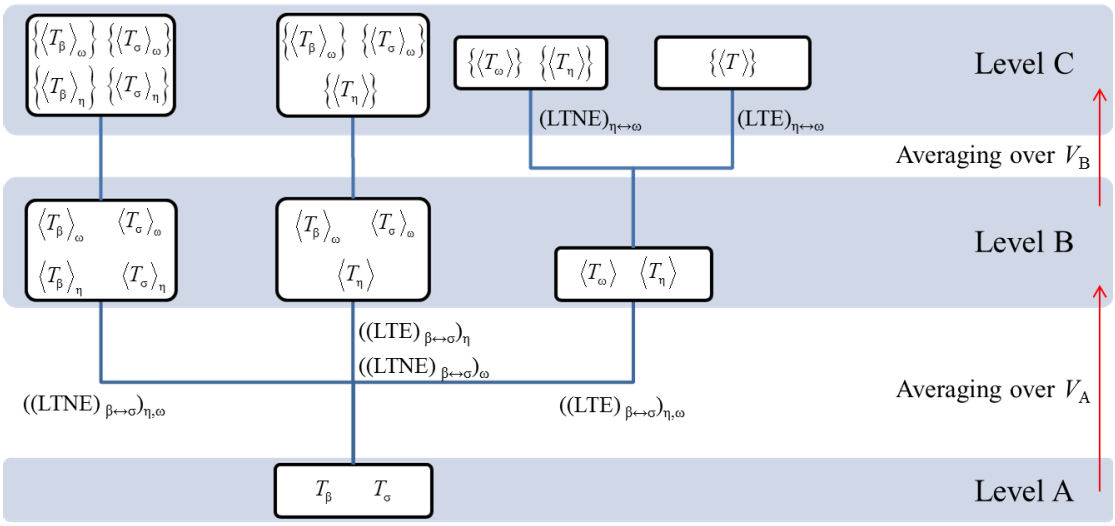

Figure 4.2. Different possible strategies for applying volume average method on the dual-scale porous medium.

In this thesis, the second strategy is employed to perform the volume-averaging procedure and derive the up-scaled governing equations for heat transfer in dual-scale porous media. This assumption was made by considering the specific application of dual-scale porous structures in solar thermochemistry, as shown in Figure 1.2. The dual-scale porous structures used for this applications can be RPC with porous struts [4, 213], or packed bed of porous particles [214]. As discussed in Section 1.1, such structures featuring dual-scale porosity, $\varepsilon_\eta = 1$ and $0 < \varepsilon_\omega < 1$, are capable of combining both of the desired properties in a solar thermochemical applications. For such cases, the velocity inside the micro-pores is considerably smaller than that of the macro-pores. Therefore, the convective heat transfer in the micro-pores can be neglected, and thus, LTE can be assumed within the micro-porous region. However, heat and mass transfer between micro- and macro-pores is of great importance, because most of the heterogeneous reactions occur in the micro-pores, and then, the species are transferred to the macro-pores. Thus, by making LTNE assumption between the regions, we ensure that heat transfer phenomena between the micro- and macro-pores are taken into account.

4.3. Darcy-level governing equations

The energy conservation equation at level A reads:

$$\left(\rho c_p\right)_\beta \frac{\partial T_\beta}{\partial t} + \left(\rho c_p\right)_\beta \nabla\cdot\left(\mathbf{v}_\beta T_\beta\right) = \nabla\cdot\left(k_\beta \cdot \nabla T_\beta\right) \tag{4.1}$$

B.C.1 $T_\beta = T_\sigma$ (4.2)

B.C.2 $\mathbf{n}_{\beta\sigma} \cdot k_\eta \cdot \nabla T_\beta = \mathbf{n}_{\beta\sigma} \cdot k_\sigma \cdot \nabla T_\sigma$ (4.3)

$$\left(\rho c_p\right)_\sigma \frac{\partial T_\sigma}{\partial t} = \nabla \cdot \left(k_\sigma \cdot \nabla T_\sigma\right) \tag{4.4}$$

where ρ, c_p and k are density, specific heat capacity, thermal conductivity, respectively. In addition, **v** and T represent the velocity vector and temperature, respectively. The VAM is used to pass information of energy transport phenomena step-by-step from smallest to largest scale until we reach the application level. For the first step, the up-scaling of energy conservation equation presented in Eqs. (4.1)–(4.4) is performed by applying volume-averaging procedure over volume V_A. Since we have two regions of η and ω with two different length-scales, volume averaging over V_A needs to be performed for both η- and ω-regions. Up-scaling the energy conservation equation from level A to level B by means of VAM was previously reported in [109, 211], and a derivation step re-used in this thesis but omitted from detailed presentation for brevity. Therefore, we start applying volume-averaging procedure over V_B on the volume-averaged energy equations at level B. As mentioned in Section 4.2, for up-scaling from level A to B, the LTE assumption is made between β- and σ-phases within both η- and ω-regions. Thus, the energy equations of the η–ω system at level B along with the corresponding boundary conditions read,

$$\left(\rho c_p\right)_\eta \varepsilon_\eta \frac{\partial \left\langle T_\eta \right\rangle^\eta}{\partial t} + \left(\rho c_p\right)_{\beta,\eta} \nabla \cdot \left(\left\langle \mathbf{v}_\beta \right\rangle_\eta \left\langle T_\eta \right\rangle^\eta\right) = \nabla \cdot \left(\mathbf{K}_\eta \cdot \nabla \left\langle T_\eta \right\rangle^\eta\right) \tag{4.5}$$

$$\left(\rho c_p\right)_\omega \varepsilon_\omega \frac{\partial \left\langle T_\omega \right\rangle^\omega}{\partial t} + \left(\rho c_p\right)_{\beta,\omega} \nabla \cdot \left(\left\langle \mathbf{v}_\beta \right\rangle_\omega \left\langle T_\omega \right\rangle^\omega\right) = \nabla \cdot \left(\mathbf{K}_\omega \cdot \nabla \left\langle T_\omega \right\rangle^\omega\right) \tag{4.6}$$

B.C.1 $\left\langle T_\eta \right\rangle^\eta = \left\langle T_\omega \right\rangle^\omega$, at $A_{\eta\omega}$ (4.7)

$$\text{B.C.2} \quad \begin{aligned} &\mathbf{n}_{\eta\omega} \cdot \left(\left(\rho c_p\right)_{\beta,\eta} \left\langle \mathbf{v}_\beta \right\rangle_\eta \left\langle T_\eta \right\rangle^\eta - \mathbf{K}_\eta \cdot \nabla \left\langle T_\eta \right\rangle^\eta\right) = \\ &= \mathbf{n}_{\eta\omega} \cdot \left(\left(\rho c_p\right)_{\beta,\omega} \left\langle \mathbf{v}_\beta \right\rangle_\omega \left\langle T_\omega \right\rangle^\omega - \mathbf{K}_\omega \cdot \nabla \left\langle T_\omega \right\rangle^\omega\right) \end{aligned}, \text{ at } A_{\eta\omega} \tag{4.8}$$

where ε and **K** are porosity and thermal conductivity tensor, respectively. In addition, $\left\langle T_\eta \right\rangle^\eta$ and $\left\langle \mathbf{v}_\beta \right\rangle_\eta$ represent the intrinsic average of temperature in the η-region and the superficial

average of velocity of the β-phase (i.e. fluid phase) in η-region, respectively. The intrinsic average of temperature is used in Eqs. (4.5)–(4.8) because it best represents thermal energy transport processes occurring in η- and ω- regions [211]. In Eq. (4.7), it is assumed that the total average temperature on the ω-region side of the interface is continuous with that of on η-region side of the interface to satisfy the thermal equilibrium at the interface. In addition, Eq. (4.8) assumes that the values of energy transfer due to conduction and convection occurring in both η- and ω-regions are equal to each other at the interface. Solution of the system of Eqs. (4.5)–(4.8) requires simultaneous solutions of mass and momentum equations. The continuity equations at level B for the η- and ω-regions and the associated boundary condition are given by

$$\nabla \cdot \left\langle \mathbf{v}_\beta \right\rangle_\eta = 0 \tag{4.9}$$

$$\nabla \cdot \left\langle \mathbf{v}_\beta \right\rangle_\omega = 0 \tag{4.10}$$

$$\text{B.C.3 } \mathbf{n}_{\eta\omega} \cdot \left\langle \mathbf{v}_\beta \right\rangle_\eta = \mathbf{n}_{\eta\omega} \cdot \left\langle \mathbf{v}_\beta \right\rangle_\omega \tag{4.11}$$

Next, we apply VAM to Eqs. (4.5)–(4.8) in V_B to up-scale the energy transport from the meso- to macro-scale level. The large-scale superficial and intrinsic averages of the general scalar transport variable are:

$$\left\{ \left\langle \psi \right\rangle_\eta \right\} = \frac{1}{V_B} \int_{V_\eta} \left\langle \psi \right\rangle_\eta \mathrm{d}V \ , \ \left\{ \left\langle \psi \right\rangle_\eta \right\}^\eta = \frac{1}{V_\eta} \int_{V_\eta} \left\langle \psi \right\rangle_\eta \mathrm{d}V \tag{4.12}$$

$$\left\{ \left\langle \psi \right\rangle_\eta \right\} = \varphi_\eta \left\{ \left\langle \psi \right\rangle_\eta \right\}^\eta \tag{4.13}$$

$$\varphi_\eta = \frac{V_\eta}{V_B} \tag{4.14}$$

In addition, the large-scale form of the spatial averaging theorem is:

$$\left\{ \nabla \left\langle \psi \right\rangle_\eta \right\} = \nabla \left\{ \left\langle \psi \right\rangle_\eta \right\} + \frac{1}{V_B} \int_{A_{\eta\omega}} \mathbf{n}_{\eta\omega} \left\langle \psi \right\rangle_\eta \mathrm{d}A \tag{4.15}$$

$$\left\{ \nabla \cdot \left\langle \psi \right\rangle_\eta \right\} = \nabla \cdot \left\{ \left\langle \psi \right\rangle_\eta \right\} + \frac{1}{V_B} \int_{A_{\eta\omega}} \mathbf{n}_{\eta\omega} \cdot \left\langle \psi \right\rangle_\eta \mathrm{d}A \tag{4.16}$$

4.4. Volume averaging of conductive and convective terms

In this study, it is assumed that the boundaries, the size of the regions, and the properties do not change with time. Therefore, the time derivative operator is not applied to them. Temperature is the only time-dependent parameter. Performing VAM on the energy transport equation for η-region, Eq. (4.5):

$$\left\{\left(\rho c_p\right)_\eta \varepsilon_\eta \frac{\partial \left\langle T_\eta \right\rangle^\eta}{\partial t}\right\} + \left\{\left(\rho c_p\right)_{\beta,\eta} \nabla \cdot \left(\left\langle \mathbf{v}_\beta \right\rangle_\eta \left\langle T_\eta \right\rangle^\eta\right)\right\} = \left\{\nabla \cdot \left(\mathbf{K}_\eta \cdot \nabla \left\langle T_\eta \right\rangle^\eta\right)\right\} \tag{4.17}$$

For the first term on the LHS of Eq. (4.17), the variation of the term $\left(\rho c_p\right)_\eta \varepsilon_\eta$ is ignored over V_B and therefore:

$$\left\{\left(\rho c_p\right)_\eta \varepsilon_\eta \frac{\partial \left\langle T_\eta \right\rangle^\eta}{\partial t}\right\} = \left(\rho c_p\right)_\eta \varepsilon_\eta \left\{\frac{\partial \left\langle T_\eta \right\rangle^\eta}{\partial t}\right\} = \left(\rho c_p\right)_\eta \varepsilon_\eta \frac{\partial \left\{\left\langle T_\eta \right\rangle^\eta\right\}}{\partial t} = \left(\rho c_p\right)_\eta \varepsilon_\eta \varphi_\eta \frac{\partial \left\{\left\langle T_\eta \right\rangle^\eta\right\}^\eta}{\partial t} \tag{4.18}$$

Using the spatial averaging theorem (SAT) provided by Eqs. (4.15) and (4.16), the convective and conductive terms take the forms as:

$$\begin{aligned}&\left\{\left(\rho c_p\right)_{\beta,\eta} \nabla \cdot \left(\left\langle \mathbf{v}_\beta \right\rangle_\eta \left\langle T_\eta \right\rangle^\eta\right)\right\} = \left(\rho c_p\right)_{\beta,\eta} \left\{\nabla \cdot \left(\left\langle \mathbf{v}_\beta \right\rangle_\eta \left\langle T_\eta \right\rangle^\eta\right)\right\} = \\ &= \left(\rho c_p\right)_{\beta,\eta} \left(\nabla \cdot \left\{\left\langle \mathbf{v}_\beta \right\rangle_\eta \left\langle T_\eta \right\rangle^\eta\right\}\right) + \frac{1}{V_B} \int_{A_{\eta\omega}} \mathbf{n}_{\eta\omega} \cdot \left(\left(\rho c_p\right)_{\beta,\eta} \left\langle \mathbf{v}_\beta \right\rangle_\eta \left\langle T_\eta \right\rangle^\eta\right) \mathrm{d}A\end{aligned} \tag{4.19}$$

$$\left\{\nabla \cdot \left(\mathbf{K}_\eta \cdot \nabla \left\langle T_\eta \right\rangle^\eta\right)\right\} = \nabla \cdot \left\{\mathbf{K}_\eta \cdot \nabla \left\langle T_\eta \right\rangle^\eta\right\} + \frac{1}{V_B} \int_{A_{\eta\omega}} \mathbf{n}_{\eta\omega} \cdot \left(\mathbf{K}_\eta \cdot \nabla \left\langle T_\eta \right\rangle^\eta\right) \mathrm{d}A \tag{4.20}$$

Substituting Eqs. (4.19) and (4.20) into (4.18) leads to:

$$\begin{aligned}&\left(\rho c_p\right)_\eta \varepsilon_\eta \varphi_\eta \frac{\partial \left\{\left\langle T_\eta \right\rangle^\eta\right\}^\eta}{\partial t} + \left(\rho c_p\right)_{\beta,\eta} \left(\nabla \cdot \left\{\left\langle \mathbf{v}_\beta \right\rangle_\eta \left\langle T_\eta \right\rangle^\eta\right\}\right) \\ &= \nabla \cdot \left\{\mathbf{K}_\eta \cdot \nabla \left\langle T_\eta \right\rangle^\eta\right\} - \frac{1}{V_B} \int_{A_{\eta\omega}} \mathbf{n}_{\eta\omega} \cdot \left(\left(\rho c_p\right)_{\beta,\eta} \left\langle \mathbf{v}_\beta \right\rangle_\eta \left\langle T_\eta \right\rangle^\eta - \mathbf{K}_\eta \cdot \nabla \left\langle T_\eta \right\rangle^\eta\right) \mathrm{d}A\end{aligned} \tag{4.21}$$

In order to consider the variation of $\mathbf{K}_\eta$, we make use of decomposition below:

$$\mathbf{K}_\eta = \left\{\mathbf{K}_\eta\right\}^\eta + \tilde{\mathbf{K}}_\eta \tag{4.22}$$

Applying the above decomposition on the first term on the RHS of Eq. (4.21) leads to:

$$\nabla\cdot\left\{\mathbf{K}_\eta\cdot\nabla\left\langle T_\eta\right\rangle^\eta\right\}=\nabla\cdot\left(\left\{\mathbf{K}_\eta\right\}^\eta\cdot\left\{\nabla\left\langle T_\eta\right\rangle^\eta\right\}+\left\{\tilde{\mathbf{K}}_\eta\cdot\nabla\left\langle T_\eta\right\rangle^\eta\right\}\right)$$
$$=\nabla\cdot\left(\left\{\mathbf{K}_\eta\right\}^\eta\cdot\left(\nabla\left\{\left\langle T_\eta\right\rangle^\eta\right\}+\frac{1}{V_\mathrm{B}}\int\limits_{A_{\eta\omega}}\mathbf{n}_{\eta\omega}\left\langle T_\eta\right\rangle^\eta\mathrm{d}A\right)+\left\{\tilde{\mathbf{K}}_\eta\cdot\nabla\left\langle T_\eta\right\rangle^\eta\right\}\right) \tag{4.23}$$

Therefore, Eq. (4.21) takes the form:

$$\left(\rho c_p\right)_\eta\varepsilon_\eta\varphi_\eta\frac{\partial\left\{\left\langle T_\eta\right\rangle^\eta\right\}^\eta}{\partial t}+\left(\rho c_p\right)_{\beta,\eta}\left(\nabla\cdot\left\{\left\langle\mathbf{v}_\beta\right\rangle_\eta\left\langle T_\eta\right\rangle^\eta\right\}\right)$$
$$=\nabla\cdot\left(\left\{\mathbf{K}_\eta\right\}^\eta\cdot\left(\nabla\left\{\left\langle T_\eta\right\rangle^\eta\right\}+\frac{1}{V_\mathrm{B}}\int\limits_{A_{\eta\omega}}\mathbf{n}_{\eta\omega}\left\langle T_\eta\right\rangle^\eta\mathrm{d}A\right)+\left\{\tilde{\mathbf{K}}_\eta\cdot\nabla\left\langle T_\eta\right\rangle^\eta\right\}\right) \tag{4.24}$$
$$-\frac{1}{V_\mathrm{B}}\int\limits_{A_{\eta\omega}}\mathbf{n}_{\eta\omega}\cdot\left(\left(\rho c_p\right)_{\beta,\eta}\left\langle\mathbf{v}_\beta\right\rangle_\eta\left\langle T_\eta\right\rangle^\eta-\mathbf{K}_\eta\cdot\nabla\left\langle T_\eta\right\rangle^\eta\right)\mathrm{d}A$$

Now we can use the decomposition below for the second term on the LHS of Eq. (4.24):

$$\left\langle\mathbf{v}_\beta\right\rangle_\eta=\left\{\left\langle\mathbf{v}_\beta\right\rangle_\eta\right\}^\eta+\tilde{\mathbf{v}}_{\beta\eta}$$
$$\left\langle T_\eta\right\rangle^\eta=\left\{\left\langle T_\eta\right\rangle^\eta\right\}^\eta+\tilde{T}_\eta \tag{4.25}$$

According to Eqs. (3.2-15)–(3.2-17) of [109]:

$$\left\{\left\langle\mathbf{v}_\beta\right\rangle_\eta\left\langle T_\eta\right\rangle^\eta\right\}=\left\{\left(\left\{\left\langle\mathbf{v}_\beta\right\rangle_\eta\right\}^\eta+\tilde{\mathbf{v}}_{\beta\eta}\right)\left(\left\{\left\langle T_\eta\right\rangle^\eta\right\}^\eta+\tilde{T}_\eta\right)\right\}$$
$$=\left\{\left\{\left\langle\mathbf{v}_\beta\right\rangle_\eta\right\}^\eta\left\{\left\langle T_\eta\right\rangle^\eta\right\}^\eta+\left\{\left\langle\mathbf{v}_\beta\right\rangle_\eta\right\}^\eta\tilde{T}_\eta+\tilde{\mathbf{v}}_{\beta\eta}\left\{\left\langle T_\eta\right\rangle^\eta\right\}^\eta+\tilde{\mathbf{v}}_{\beta\eta}\tilde{T}_\eta\right\} \tag{4.26}$$
$$=\varphi_\eta\left\{\left\langle\mathbf{v}_\beta\right\rangle_\eta\right\}^\eta\left\{\left\langle T_\eta\right\rangle^\eta\right\}^\eta+\varphi_\eta\left\{\tilde{\mathbf{v}}_{\beta\eta}\tilde{T}_\eta\right\}^\eta$$

Substituting Eq. (4.26) into (4.24) leads to:

$$\left(\rho c_p\right)_\eta\varepsilon_\eta\varphi_\eta\frac{\partial\left\{\left\langle T_\eta\right\rangle^\eta\right\}^\eta}{\partial t}+\left(\rho c_p\right)_{\beta,\eta}\left(\nabla\cdot\left(\varphi_\eta\left\{\left\langle\mathbf{v}_\beta\right\rangle_\eta\right\}^\eta\left\{\left\langle T_\eta\right\rangle^\eta\right\}^\eta\right)\right)$$
$$=\nabla\cdot\left(\left\{\mathbf{K}_\eta\right\}^\eta\cdot\left(\nabla\left\{\left\langle T_\eta\right\rangle^\eta\right\}+\frac{1}{V_\mathrm{B}}\int\limits_{A_{\eta\omega}}\mathbf{n}_{\eta\omega}\left\langle T_\eta\right\rangle^\eta\mathrm{d}A\right)+\left\{\tilde{\mathbf{K}}_\eta\cdot\nabla\left\langle T_\eta\right\rangle^\eta\right\}\right) \tag{4.27}$$
$$-\left(\rho c_p\right)_{\beta,\eta}\nabla\cdot\left(\varphi_\eta\left\{\tilde{\mathbf{v}}_{\beta\eta}\tilde{T}_\eta\right\}^\eta\right)-\frac{1}{V_\mathrm{B}}\int\limits_{A_{\eta\omega}}\mathbf{n}_{\eta\omega}\cdot\left(\left(\rho c_p\right)_{\beta,\eta}\left\langle\mathbf{v}_\beta\right\rangle_\eta\left\langle T_\eta\right\rangle^\eta-\mathbf{K}_\eta\cdot\nabla\left\langle T_\eta\right\rangle^\eta\right)\mathrm{d}A$$

To address the term $\left(\nabla\left\{\left\langle T_\eta\right\rangle^\eta\right\}+\frac{1}{V_\mathrm{B}}\int\limits_{A_{\eta\omega}}\mathbf{n}_{\eta\omega}\left\langle T_\eta\right\rangle^\eta \mathrm{d}A\right)$, we use the decomposition provided in Eq. (4.25) for temperature. In addition, variations of average quantities $\left\{\left\langle T_\eta\right\rangle^\eta\right\}^\eta$ within the averaging volume V_B are zero. Thus, by following the procedure presented by Carbonell and Whitaker [114] we obtain:

$$\begin{aligned}
&\nabla\left\{\left\langle T_\eta\right\rangle^\eta\right\}+\frac{1}{V_\mathrm{B}}\int\limits_{A_{\eta\omega}}\mathbf{n}_{\eta\omega}\left\langle T_\eta\right\rangle^\eta \mathrm{d}A=\nabla\left(\varphi_\eta\left\{\left\langle T_\eta\right\rangle^\eta\right\}^\eta\right)+\frac{1}{V_\mathrm{B}}\int\limits_{A_{\eta\omega}}\mathbf{n}_{\eta\omega}\left\{\left\langle T_\eta\right\rangle^\eta\right\}^\eta \mathrm{d}A+\frac{1}{V_\mathrm{B}}\int\limits_{A_{\eta\omega}}\mathbf{n}_{\eta\omega}\tilde{T}_\eta \mathrm{d}A=\\
&=\left\{\left\langle T_\eta\right\rangle^\eta\right\}^\eta\nabla\varphi_\eta+\varphi_\eta\nabla\left\{\left\langle T_\eta\right\rangle^\eta\right\}^\eta+\left\{\left\langle T_\eta\right\rangle^\eta\right\}^\eta\underbrace{\left(\frac{1}{V_\mathrm{B}}\int\limits_{A_{\eta\omega}}\mathbf{n}_{\eta\omega}\mathrm{d}A\right)}_{-\nabla\varphi_\eta}+\frac{1}{V_\mathrm{B}}\int\limits_{A_{\eta\omega}}\mathbf{n}_{\eta\omega}\tilde{T}_\eta \mathrm{d}A=\\
&=\varphi_\eta\nabla\left\{\left\langle T_\eta\right\rangle^\eta\right\}^\eta+\frac{1}{V_\mathrm{B}}\int\limits_{A_{\eta\omega}}\mathbf{n}_{\eta\omega}\tilde{T}_\eta \mathrm{d}A
\end{aligned}\tag{4.28}$$

Considering the term $\left\{\tilde{\mathbf{K}}_\eta\cdot\nabla\left\langle T_\eta\right\rangle^\eta\right\}$ and using the decomposition presented in Eq. (4.25) for temperature:

$$\left\{\tilde{\mathbf{K}}_\eta\cdot\nabla\left\langle T_\eta\right\rangle^\eta\right\}=\left\{\tilde{\mathbf{K}}_\eta\cdot\nabla\left\{\left\langle T_\eta\right\rangle^\eta\right\}^\eta\right\}+\left\{\tilde{\mathbf{K}}_\eta\cdot\nabla\tilde{T}_\eta\right\}\tag{4.29}$$

Once again, since variations of average quantities within the averaging volume are zero and also the fact that $\left\{\tilde{\psi}\right\}=0$, the first term on the RHS of Eq. (4.29) is zero. Substituting Eqs. (4.28) and (4.29) into (4.27) leads to:

$$\begin{aligned}
&\underbrace{\left(\rho c_p\right)_\eta\varepsilon_\eta\varphi_\eta\frac{\partial\left\{\left\langle T_\eta\right\rangle^\eta\right\}^\eta}{\partial t}}_{\text{accumulation}}+\underbrace{\left(\rho c_p\right)_{\beta,\eta}\left(\nabla\cdot\left(\varphi_\eta\left\{\left\langle \mathbf{v}_\beta\right\rangle_\eta\right\}^\eta\left\{\left\langle T_\eta\right\rangle^\eta\right\}^\eta\right)\right)}_{\text{macro-scale convection}}\\
&=\underbrace{\nabla\cdot\left(\left\{\mathbf{K}_\eta\right\}^\eta\left(\varphi_\eta\nabla\left\{\left\langle T_\eta\right\rangle^\eta\right\}^\eta+\frac{1}{V_\mathrm{B}}\int\limits_{A_{\eta\omega}}\mathbf{n}_{\eta\omega}\tilde{T}_\eta \mathrm{d}A\right)+\left\{\tilde{\mathbf{K}}_\eta\cdot\nabla\tilde{T}_\eta\right\}\right)}_{\text{macro-scale conduction}}\\
&\underbrace{-\left(\rho c_p\right)_{\beta,\eta}\nabla\cdot\left(\varphi_\eta\left\{\tilde{\mathbf{v}}_{\beta\eta}\tilde{T}_\eta\right\}^\eta\right)}_{\text{macro-scale dispersion}}\underbrace{-\frac{1}{V_\mathrm{B}}\int\limits_{A_{\eta\omega}}\mathbf{n}_{\eta\omega}\cdot\left(\left(\rho c_p\right)_{\beta,\eta}\left\langle \mathbf{v}_\beta\right\rangle_\eta\left\langle T_\eta\right\rangle^\eta-\mathbf{K}_\eta\cdot\nabla\left\langle T_\eta\right\rangle^\eta\right)\mathrm{d}A}_{\text{inter-region flux}}
\end{aligned}\tag{4.30}$$

The heat transfer equation for the ω-region is:

$$\underbrace{\left(\rho c_p\right)_{\omega}\varepsilon_{\omega}\varphi_{\omega}\frac{\partial\left\{\left\langle T_{\eta}\right\rangle^{\omega}\right\}^{\omega}}{\partial t}}_{\text{accumulation}}+\underbrace{\left(\rho c_p\right)_{\beta,\omega}\left(\nabla\cdot\left(\varphi_{\omega}\left\{\left\langle \mathbf{v}_{\beta}\right\rangle_{\omega}\right\}^{\omega}\left\{\left\langle T_{\omega}\right\rangle^{\omega}\right\}^{\omega}\right)\right)}_{\text{macro-scale convection}}$$

$$=\underbrace{\nabla\cdot\left(\left\{\mathbf{K}_{\omega}\right\}^{\omega}\left(\varphi_{\omega}\nabla\left\{\left\langle T_{\omega}\right\rangle^{\omega}\right\}^{\omega}+\frac{1}{V_{\mathrm{B}}}\int_{A_{\omega\eta}}\mathbf{n}_{\omega\eta}\tilde{T}_{\omega}\mathrm{d}A\right)+\left\{\tilde{\mathbf{K}}_{\omega}\cdot\nabla\tilde{T}_{\omega}\right\}\right)}_{\text{macro-scale conduction}} \tag{4.31}$$

$$-\underbrace{\left(\rho c_p\right)_{\beta,\omega}\nabla\cdot\left(\varphi_{\omega}\left\{\tilde{\mathbf{v}}_{\beta\omega}\tilde{T}_{\omega}\right\}^{\omega}\right)}_{\text{macro-scale dispersion}}-\underbrace{\frac{1}{V_{\mathrm{B}}}\int_{A_{\omega\eta}}\mathbf{n}_{\omega\eta}\cdot\left(\left(\rho c_p\right)_{\beta,\omega}\left\langle \mathbf{v}_{\beta}\right\rangle_{\omega}\left\langle T_{\omega}\right\rangle^{\omega}-\mathbf{K}_{\omega}\cdot\nabla\left\langle T_{\omega}\right\rangle^{\omega}\right)\mathrm{d}A}_{\text{inter-region flux}}$$

The macro-scale continuity conservation equation is required in the process of developing the two-equation model.

$$\begin{aligned}&\left\{\nabla\cdot\left\langle \mathbf{v}_{\beta}\right\rangle_{\eta}\right\}=0\Rightarrow\nabla\cdot\left\{\left\langle \mathbf{v}_{\beta}\right\rangle_{\eta}\right\}+\frac{1}{V_{\infty}}\int_{A_{\eta\omega}}\mathbf{n}_{\eta\omega}\cdot\left\langle \mathbf{v}_{\beta}\right\rangle_{\eta}dA=0\\&\left\{\nabla\cdot\left\langle \mathbf{v}_{\beta}\right\rangle_{\omega}\right\}=0\Rightarrow\nabla\cdot\left\{\left\langle \mathbf{v}_{\beta}\right\rangle_{\omega}\right\}+\frac{1}{V_{\infty}}\int_{A_{\omega\eta}}\mathbf{n}_{\omega\eta}\cdot\left\langle \mathbf{v}_{\beta}\right\rangle_{\omega}dA=0\end{aligned} \tag{4.32}$$

Using the decomposition presented in Eq. (4.25) for temperature on the inter-region flux term:

$$\begin{aligned}&\frac{1}{V_{\mathrm{B}}}\int_{A_{\eta\omega}}\mathbf{n}_{\eta\omega}\cdot\left(\left(\rho c_p\right)_{\beta,\eta}\left\langle \mathbf{v}_{\beta}\right\rangle_{\eta}\left\langle T_{\eta}\right\rangle^{\eta}-\mathbf{K}_{\eta}\cdot\nabla\left\langle T_{\eta}\right\rangle^{\eta}\right)\mathrm{d}A\\&=\frac{1}{V_{\mathrm{B}}}\int_{A_{\eta\omega}}\mathbf{n}_{\eta\omega}\cdot\left(\left(\rho c_p\right)_{\beta,\eta}\left\langle \mathbf{v}_{\beta}\right\rangle_{\eta}\left\{\left\langle T_{\eta}\right\rangle^{\eta}\right\}^{\eta}-\mathbf{K}_{\eta}\cdot\nabla\left\{\left\langle T_{\eta}\right\rangle^{\eta}\right\}^{\eta}\right)\mathrm{d}A\\&+\frac{1}{V_{\mathrm{B}}}\int_{A_{\eta\omega}}\mathbf{n}_{\eta\omega}\cdot\left(\left(\rho c_p\right)_{\beta,\eta}\left\langle \mathbf{v}_{\beta}\right\rangle_{\eta}\tilde{T}_{\eta}-\mathbf{K}_{\eta}\cdot\nabla\tilde{T}_{\eta}\right)\mathrm{d}A\end{aligned} \tag{4.33}$$

The second term on the RHS of Eq. (4.33) can be conveniently utilised to formulate the closure problem since it only contains the spatial deviation quantities. However, the first term is required to be treated using the decomposition provided in Eq. (4.22):

$$
\begin{aligned}
&\frac{1}{V_{\mathrm{B}}}\int\limits_{A_{\eta\omega}}\mathbf{n}_{\eta\omega}\cdot\left(\left(\rho c_p\right)_{\beta,\eta}\left\langle\mathbf{v}_\beta\right\rangle_\eta\left\{\left\langle T_\eta\right\rangle^\eta\right\}^\eta-\mathbf{K}_\eta\cdot\nabla\left\{\left\langle T_\eta\right\rangle^\eta\right\}^\eta\right)\mathrm{d}A\\
&=\frac{1}{V_{\mathrm{B}}}\int\limits_{A_{\eta\omega}}\mathbf{n}_{\eta\omega}\cdot\left(\left(\rho c_p\right)_{\beta,\eta}\left\langle\mathbf{v}_\beta\right\rangle_\eta\left\{\left\langle T_\eta\right\rangle^\eta\right\}^\eta-\left\{\mathbf{K}_\eta\right\}^\eta\cdot\nabla\left\{\left\langle T_\eta\right\rangle^\eta\right\}^\eta-\tilde{\mathbf{K}}_\eta\cdot\nabla\left\{\left\langle T_\eta\right\rangle^\eta\right\}^\eta\right)\mathrm{d}A\\
&=\left(\rho c_p\right)_{\beta,\eta}\left\{\left\langle T_\eta\right\rangle^\eta\right\}^\eta\underbrace{\left(\frac{1}{V_{\mathrm{B}}}\int\limits_{A_{\eta\omega}}\mathbf{n}_{\eta\omega}\cdot\left\langle\mathbf{v}_\beta\right\rangle_\eta\mathrm{d}A\right)}_{\text{zero}}\\
&-\left\{\mathbf{K}_\eta\right\}^\eta\cdot\nabla\left\{\left\langle T_\eta\right\rangle^\eta\right\}^\eta\underbrace{\left(\frac{1}{V_{\mathrm{B}}}\int\limits_{A_{\eta\omega}}\mathbf{n}_{\eta\omega}\mathrm{d}A\right)}_{\nabla\varphi_\eta}-\frac{1}{V_{\mathrm{B}}}\int\limits_{A_{\eta\omega}}\mathbf{n}_{\eta\omega}\cdot\left(\tilde{\mathbf{K}}_\eta\cdot\nabla\left\{\left\langle T_\eta\right\rangle^\eta\right\}^\eta\right)\mathrm{d}A
\end{aligned}
\tag{4.34}
$$

For a spatially periodic system, the first term on the RHS of Eq. (4.34) and $\nabla\varphi_\eta$ are zero [168]. Consequently, Eq. (4.34) takes the form:

$$
\begin{aligned}
&\frac{1}{V_{\mathrm{B}}}\int\limits_{A_{\eta\omega}}\mathbf{n}_{\eta\omega}\cdot\left(\left(\rho c_p\right)_{\beta,\eta}\left\langle\mathbf{v}_\beta\right\rangle_\eta\left\{\left\langle T_\eta\right\rangle^\eta\right\}^\eta-\mathbf{K}_\eta\cdot\nabla\left\{\left\langle T_\eta\right\rangle^\eta\right\}^\eta\right)\mathrm{d}A=\\
&=-\frac{1}{V_{\mathrm{B}}}\int\limits_{A_{\eta\omega}}\mathbf{n}_{\eta\omega}\cdot\left(\tilde{\mathbf{K}}_\eta\cdot\nabla\left\{\left\langle T_\eta\right\rangle^\eta\right\}^\eta\right)\mathrm{d}A
\end{aligned}
\tag{4.35}
$$

By substituting Eq. (4.35) into Eq. (4.33), the inter-region flux term takes the form:

$$
\begin{aligned}
&\frac{1}{V_{\mathrm{B}}}\int\limits_{A_{\eta\omega}}\mathbf{n}_{\eta\omega}\cdot\left(\left(\rho c_p\right)_{\beta,\eta}\left\langle\mathbf{v}_\beta\right\rangle_\eta\left\langle T_\eta\right\rangle^\eta-\mathbf{K}_\eta\cdot\nabla\left\langle T_\eta\right\rangle^\eta\right)\mathrm{d}A\\
&=\frac{1}{V_{\mathrm{B}}}\int\limits_{A_{\eta\omega}}\mathbf{n}_{\eta\omega}\cdot\left(\left(\rho c_p\right)_{\beta,\eta}\left\langle\mathbf{v}_\beta\right\rangle_\eta\tilde{T}_\eta-\mathbf{K}_\eta\cdot\nabla\tilde{T}_\eta-\tilde{\mathbf{K}}_\eta\cdot\nabla\left\{\left\langle T_\eta\right\rangle^\eta\right\}^\eta\right)\mathrm{d}A
\end{aligned}
\tag{4.36}
$$

By substituting the inter-region flux term developed in Eq. (4.36) into Eq. (4.31), the large-scale average heat transfer equation for η- and ω-region takes the form:

$$\underbrace{\left(\rho c_p\right)_\eta \varepsilon_\eta \varphi_\eta \frac{\partial\left\{\left\langle T_\eta\right\rangle^\eta\right\}^\eta}{\partial t}}_{\text{accumulation}}+\underbrace{\left(\rho c_p\right)_{\beta,\eta}\left(\nabla\cdot\left(\varphi_\eta\left\{\left\langle \mathbf{v}_\beta\right\rangle_\eta\right\}^\eta\left\{\left\langle T_\eta\right\rangle^\eta\right\}^\eta\right)\right)}_{\text{macro-scale convection}}$$

$$=\underbrace{\nabla\cdot\left(\left\{\mathbf{K}_\eta\right\}^\eta\cdot\left(\varphi_\eta\nabla\left\{\left\langle T_\eta\right\rangle^\eta\right\}^\eta+\frac{1}{V_\mathrm{B}}\int_{A_{\eta\omega}}\mathbf{n}_{\eta\omega}\tilde{T}_\eta \mathrm{d}A\right)+\left\{\tilde{\mathbf{K}}_\eta\cdot\nabla\tilde{T}_\eta\right\}\right)}_{\text{macro-scale conduction}} \tag{4.37}$$

$$-\underbrace{\left(\rho c_p\right)_{\beta,\eta}\nabla\cdot\left(\varphi_\eta\left\{\tilde{\mathbf{v}}_{\beta\eta}\tilde{T}_\eta\right\}^\eta\right)}_{\text{macro-scale dispersion}}-\underbrace{\frac{1}{V_\mathrm{B}}\int_{A_{\eta\omega}}\mathbf{n}_{\eta\omega}\cdot\left(\left(\rho c_p\right)_{\beta,\eta}\left\langle \mathbf{v}_\beta\right\rangle_\eta\tilde{T}_\eta-\mathbf{K}_\eta\cdot\nabla\tilde{T}_\eta-\tilde{\mathbf{K}}_\eta\cdot\nabla\left\{\left\langle T_\eta\right\rangle^\eta\right\}^\eta\right)\mathrm{d}A}_{\text{inter-region flux}}$$

$$\underbrace{\left(\rho c_p\right)_\omega \varepsilon_\omega \varphi_\omega \frac{\partial\left\{\left\langle T_\omega\right\rangle^\omega\right\}^\omega}{\partial t}}_{\text{accumulation}}+\underbrace{\left(\rho c_p\right)_{\beta,\omega}\left(\nabla\cdot\left(\varphi_\omega\left\{\left\langle \mathbf{v}_\beta\right\rangle_\omega\right\}^\omega\left\{\left\langle T_\omega\right\rangle^\omega\right\}^\omega\right)\right)}_{\text{macro-scale convection}}$$

$$=\underbrace{\nabla\cdot\left(\left\{\mathbf{K}_\omega\right\}^\omega\cdot\left(\varphi_\omega\nabla\left\{\left\langle T_\omega\right\rangle^\omega\right\}^\omega+\frac{1}{V_\mathrm{B}}\int_{A_{\omega\eta}}\mathbf{n}_{\omega\eta}\tilde{T}_\omega \mathrm{d}A\right)+\left\{\tilde{\mathbf{K}}_\omega\cdot\nabla\tilde{T}_\omega\right\}\right)}_{\text{macro-scale conduction}} \tag{4.38}$$

$$-\underbrace{\left(\rho c_p\right)_{\beta,\omega}\nabla\cdot\left(\varphi_\omega\left\{\tilde{\mathbf{v}}_{\beta\omega}\tilde{T}_\omega\right\}^\omega\right)}_{\text{macro-scale dispersion}}-\underbrace{\frac{1}{V_\mathrm{B}}\int_{A_{\omega\eta}}\mathbf{n}_{\omega\eta}\cdot\left(\left(\rho c_p\right)_{\beta,\omega}\left\langle \mathbf{v}_\beta\right\rangle_\omega\tilde{T}_\omega-\mathbf{K}_\omega\cdot\nabla\tilde{T}_\omega-\tilde{\mathbf{K}}_\omega\cdot\nabla\left\{\left\langle T_\omega\right\rangle^\omega\right\}^\omega\right)\mathrm{d}A}_{\text{inter-region flux}}$$

In Eqs. (4.37) and (4.38), there are some terms with large-scale averages such as $\left(\varphi_\eta\left\{\left\langle \mathbf{v}_\beta\right\rangle_\eta\right\}^\eta\left\{\left\langle T_\eta\right\rangle^\eta\right\}^\eta\right)$, and some terms involving the spatial deviation quantities such as $\tilde{\mathbf{v}}_{\beta\eta}\tilde{T}_\eta$. In addition, the inter-region flux is specified entirely in terms of the Darcy-scale variables such as $\left\langle \mathbf{v}_\beta\right\rangle_\eta$. In the following section, we need to develop the closure problem which will allow us to determine the terms such as $\left\{\tilde{\mathbf{K}}_\eta\cdot\nabla\tilde{T}_\eta\right\}$ and $\left\{\tilde{\mathbf{v}}_{\beta\eta}\tilde{T}_\eta\right\}^\eta$. More importantly, developing a representation for the inter-region flux is required, which is entirely determined by the closure problem.

4.5. Introducing closure problems

All terms in Eqs. (4.37) and (4.38) are either macro-scale averages or spatial deviation quantities. Thus, the closure problem must be formulated and solved to proceed. There is no

need to decompose the Darcy-level velocity, $\left\langle \mathbf{v}_\beta \right\rangle_\eta$ or $\left\langle \mathbf{v}_\beta \right\rangle_\omega$, since it is available directly from solving the meso-scale mass and momentum equations for a unit cell of a spatially periodic porous medium. By assuming constant φ_η, the closure problems for the spatial deviation temperatures, $\tilde{T}_\eta$ and $\tilde{T}_\omega$, are developed by subtracting the intrinsic form of Eq. (4.37) from (4.5) and (4.38) from (4.6),:

$$\begin{aligned}
&\left(\rho c_p\right)_\eta \varepsilon_\eta \frac{\partial \tilde{T}_\eta}{\partial t} + \left(\rho c_p\right)_{\beta,\eta} \left(\nabla \cdot \left(\left\langle \mathbf{v}_\beta \right\rangle_\eta \left\langle T \right\rangle_\eta^\beta - \left\{ \left\langle \mathbf{v}_\beta \right\rangle_\eta \right\}^\eta \left\{ \left\langle T_\eta \right\rangle^\eta \right\}^\eta \right) \right) \\
&= \nabla \cdot \left(\mathbf{K}_\eta \cdot \nabla \left\langle T_\eta \right\rangle^\eta - \left\{ \mathbf{K}_\eta \right\}^\eta \cdot \nabla \left\{ \left\langle T_\eta \right\rangle^\eta \right\}^\eta \right) - \nabla \cdot \left(\frac{\varphi_\eta^{-1} \left\{ \mathbf{K}_\eta \right\}^\eta}{V_\mathrm{B}} \int_{A_{\eta\omega}} \mathbf{n}_{\eta\omega} \tilde{T}_\eta \mathrm{d}A + \left\{ \tilde{\mathbf{K}}_\eta \cdot \nabla \tilde{T}_\eta \right\}^\eta \right) \\
&+ \left(\rho c_p\right)_{\beta,\eta} \nabla \cdot \left(\left\{ \tilde{\mathbf{v}}_{\beta\eta} \tilde{T}_\eta \right\}^\eta \right) + \frac{\varphi_\eta^{-1}}{V_\mathrm{B}} \int_{A_{\eta\omega}} \mathbf{n}_{\eta\omega} \cdot \left(\left(\rho c_p\right)_{\beta,\eta} \left\langle \mathbf{v}_\beta \right\rangle_\eta \tilde{T}_\eta - \mathbf{K}_\eta \cdot \nabla \tilde{T}_\eta - \tilde{\mathbf{K}}_\eta \cdot \nabla \left\{ \left\langle T_\eta \right\rangle^\eta \right\}^\eta \right) \mathrm{d}A
\end{aligned} \tag{4.39}$$

Subtracting Eq. (4.39) from (4.5) leads to:

$$\begin{aligned}
&\left(\rho c_p\right)_\eta \varepsilon_\eta \frac{\partial \tilde{T}_\eta}{\partial t} + \left(\rho c_p\right)_{\beta,\eta} \left(\nabla \cdot \left(\left\langle \mathbf{v}_\beta \right\rangle_\eta \left\langle T \right\rangle_\eta^\beta - \left\{ \left\langle \mathbf{v}_\beta \right\rangle_\eta \right\}^\eta \left\{ \left\langle T_\eta \right\rangle^\eta \right\}^\eta \right) \right) \\
&= \nabla \cdot \left(\mathbf{K}_\eta \cdot \nabla \left\langle T_\eta \right\rangle^\eta - \left\{ \mathbf{K}_\eta \right\}^\eta \cdot \nabla \left\{ \left\langle T_\eta \right\rangle^\eta \right\}^\eta \right) - \nabla \cdot \left(\frac{\varphi_\eta^{-1} \left\{ \mathbf{K}_\eta \right\}^\eta}{V_\mathrm{B}} \int_{A_{\eta\omega}} \mathbf{n}_{\eta\omega} \tilde{T}_\eta \mathrm{d}A + \left\{ \tilde{\mathbf{K}}_\eta \cdot \nabla \tilde{T}_\eta \right\}^\eta \right) \\
&+ \left(\rho c_p\right)_{\beta,\eta} \nabla \cdot \left(\left\{ \tilde{\mathbf{v}}_{\beta\eta} \tilde{T}_\eta \right\}^\eta \right) + \frac{\varphi_\eta^{-1}}{V_\mathrm{B}} \int_{A_{\eta\omega}} \mathbf{n}_{\eta\omega} \cdot \left(\left(\rho c_p\right)_{\beta,\eta} \left\langle \mathbf{v}_\beta \right\rangle_\eta \tilde{T}_\eta - \mathbf{K}_\eta \cdot \nabla \tilde{T}_\eta - \tilde{\mathbf{K}}_\eta \cdot \nabla \left\{ \left\langle T_\eta \right\rangle^\eta \right\}^\eta \right) \mathrm{d}A
\end{aligned} \tag{4.40}$$

To obtain $\left\langle \mathbf{v}_\beta \right\rangle_\eta \left\langle T_\eta \right\rangle^\eta - \left\{ \left\langle \mathbf{v}_\beta \right\rangle_\eta \right\}^\eta \left\{ \left\langle T_\eta \right\rangle^\eta \right\}^\eta$, we multiply the two decompositions presented in Eq. (4.25) together:

$$\left\langle \mathbf{v}_\beta \right\rangle_\eta \left\langle T_\eta \right\rangle^\eta = \left\{ \left\langle \mathbf{v}_\beta \right\rangle_\eta \right\}^\eta \left\{ \left\langle T_\eta \right\rangle^\eta \right\}^\eta + \left\{ \left\langle \mathbf{v}_\beta \right\rangle_\eta \right\}^\eta \tilde{T}_\eta + \tilde{\mathbf{v}}_{\beta\eta} \left\{ \left\langle T_\eta \right\rangle^\eta \right\}^\eta + \tilde{\mathbf{v}}_{\beta\eta} \tilde{T}_\eta$$

$$\Rightarrow \left\langle \mathbf{v}_\beta \right\rangle_\eta \left\langle T_\eta \right\rangle^\eta - \left\{ \left\langle \mathbf{v}_\beta \right\rangle_\eta \right\}^\eta \left\{ \left\langle T_\eta \right\rangle^\eta \right\}^\eta = \left\{ \left\langle \mathbf{v}_\beta \right\rangle_\eta \right\}^\eta \tilde{T}_\eta + \tilde{\mathbf{v}}_{\beta\eta} \left\{ \left\langle T_\eta \right\rangle^\eta \right\}^\eta + \tilde{\mathbf{v}}_{\beta\eta} \tilde{T}_\eta$$

$$= \left(\left\{ \left\langle \mathbf{v}_\beta \right\rangle_\eta \right\}^\eta + \tilde{\mathbf{v}}_{\beta\eta} \right) \tilde{T}_\eta + \tilde{\mathbf{v}}_{\beta\eta} \left\{ \left\langle T_\eta \right\rangle^\eta \right\}^\eta = \left\langle \mathbf{v}_\beta \right\rangle_\eta \tilde{T}_\eta + \tilde{\mathbf{v}}_{\beta\eta} \left\{ \left\langle T_\eta \right\rangle^\eta \right\}^\eta \tag{4.41}$$

$$\Rightarrow \nabla \cdot \left(\left\langle \mathbf{v}_\beta \right\rangle_\eta \left\langle T_\eta \right\rangle^\eta - \left\{ \left\langle \mathbf{v}_\beta \right\rangle_\eta \right\}^\eta \left\{ \left\langle T_\eta \right\rangle^\eta \right\}^\eta \right) = \nabla \cdot \left(\left\langle \mathbf{v}_\beta \right\rangle_\eta \tilde{T}_\eta \right) + \nabla \cdot \left(\tilde{\mathbf{v}}_{\beta\eta} \left\{ \left\langle T_\eta \right\rangle^\eta \right\}^\eta \right)$$

$$\Rightarrow \nabla \cdot \left(\left\langle \mathbf{v}_\beta \right\rangle_\eta \left\langle T_\eta \right\rangle^\eta - \left\{ \left\langle \mathbf{v}_\beta \right\rangle_\eta \right\}^\eta \left\{ \left\langle T_\eta \right\rangle^\eta \right\}^\eta \right) = \nabla \cdot \left(\left\langle \mathbf{v}_\beta \right\rangle_\eta \tilde{T}_\eta \right) + \left\{ \left\langle T_\eta \right\rangle^\eta \right\}^\eta \nabla \cdot \tilde{\mathbf{v}}_{\beta\eta} + \tilde{\mathbf{v}}_{\beta\eta} \nabla \cdot \left\{ \left\langle T_\eta \right\rangle^\eta \right\}^\eta$$

Considering the decomposition presented in Eq. (4.25) for velocity:

$$\left\langle \mathbf{v}_\beta \right\rangle_\eta = \left\{ \left\langle \mathbf{v}_\beta \right\rangle_\eta \right\}^\eta + \tilde{\mathbf{v}}_{\beta\eta} \Rightarrow \underbrace{\nabla \cdot \left\langle \mathbf{v}_\beta \right\rangle_\eta}_{\text{zero}} = \nabla \cdot \left\{ \left\langle \mathbf{v}_\beta \right\rangle_\eta \right\}^\eta + \nabla \cdot \tilde{\mathbf{v}}_{\beta\eta} \tag{4.42}$$

According to Eq. (4.9), $\nabla \cdot \left\langle \mathbf{v}_\beta \right\rangle_\eta = 0$. For a spatially periodic system, $\nabla \cdot \left\{ \left\langle \mathbf{v}_\beta \right\rangle_\eta \right\}^\eta$ is zero.

Consequently, $\nabla \cdot \tilde{\mathbf{v}}_{\beta\eta} = 0$ and Eq. (4.41) is simplified to:

$$\nabla \cdot \left(\left\langle \mathbf{v}_\beta \right\rangle_\eta \left\langle T_\eta \right\rangle^\eta - \left\{ \left\langle \mathbf{v}_\beta \right\rangle_\eta \right\}^\eta \left\{ \left\langle T_\eta \right\rangle^\eta \right\}^\eta \right) = \nabla \cdot \left(\left\langle \mathbf{v}_\beta \right\rangle_\eta \tilde{T}_\eta \right) + \tilde{\mathbf{v}}_{\beta\eta} \nabla \cdot \left\{ \left\langle T_\eta \right\rangle^\eta \right\}^\eta \tag{4.43}$$

We again apply the decomposition presented in Eqs. (4.22) and (4.25) for thermal conductivity and temperature:

$$\begin{aligned}
&\mathbf{K}_\eta \cdot \nabla \left\langle T_\eta \right\rangle^\eta - \left\{ \mathbf{K}_\eta \right\}^\eta \cdot \nabla \left\{ \left\langle T_\eta \right\rangle^\eta \right\}^\eta \\
&= \left(\left\{ \mathbf{K}_\eta \right\}^\eta + \tilde{\mathbf{K}}_\eta \right) \cdot \left(\nabla \left\{ \left\langle T_\eta \right\rangle^\eta \right\}^\eta + \nabla \tilde{T}_\eta \right) - \left\{ \mathbf{K}_\eta \right\}^\eta \cdot \nabla \left\{ \left\langle T_\eta \right\rangle^\eta \right\}^\eta \\
&= \cancel{\left\{ \mathbf{K}_\eta \right\}^\eta \cdot \nabla \left\{ \left\langle T_\eta \right\rangle^\eta \right\}^\eta} + \left\{ \mathbf{K}_\eta \right\}^\eta \cdot \nabla \tilde{T}_\eta + \tilde{\mathbf{K}}_\eta \cdot \nabla \left\{ \left\langle T_\eta \right\rangle^\eta \right\}^\eta + \tilde{\mathbf{K}}_\eta \cdot \nabla \tilde{T}_\eta - \cancel{\left\{ \mathbf{K}_\eta \right\}^\eta \cdot \nabla \left\{ \left\langle T_\eta \right\rangle^\eta \right\}^\eta} \\
&= \underbrace{\left(\left\{ \mathbf{K}_\eta \right\}^\eta + \tilde{\mathbf{K}}_\eta \right)}_{\mathbf{K}_\eta} \cdot \nabla \tilde{T}_\eta + \tilde{\mathbf{K}}_\eta \cdot \nabla \left\{ \left\langle T_\eta \right\rangle^\eta \right\}^\eta
\end{aligned} \tag{4.44}$$

By substituting Eqs. (4.43) and (4.44) into (4.40), the transport equation for $\tilde{T}_\eta$ becomes:

$$\left(\rho c_p\right)_\eta \varepsilon_\eta \frac{\partial \tilde{T}_\eta}{\partial t} + \left(\rho c_p\right)_{\beta,\eta} \nabla\cdot\left(\left\langle \mathbf{v}_\beta \right\rangle_\eta \tilde{T}_\eta\right) + \underbrace{\left(\rho c_p\right)_{\beta,\eta} \tilde{\mathbf{v}}_{\beta\eta} \nabla\cdot\left\{\left\langle T_\eta \right\rangle^\eta\right\}}_{\text{convective source}} - \left(\rho c_p\right)_{\beta,\eta} \nabla\cdot\left\{\tilde{\mathbf{v}}_{\beta\eta}\tilde{T}_\eta\right\}^\eta$$

$$= \nabla\cdot\left(\mathbf{K}_\eta\cdot\nabla\tilde{T}_\eta\right) + \underbrace{\nabla\cdot\left(\tilde{\mathbf{K}}_\eta\cdot\nabla\left\{\left\langle T_\eta\right\rangle^\eta\right\}^\eta\right)}_{\text{diffusive source}} - \nabla\cdot\left(\frac{\varphi_\eta^{-1}\left\{\mathbf{K}_\eta\right\}^\eta}{V_\mathrm{B}}\int_{A_{\eta\omega}}\mathbf{n}_{\eta\omega}\tilde{T}_\eta \mathrm{d}A + \left\{\tilde{\mathbf{K}}_\eta\cdot\nabla\tilde{T}_\eta\right\}^\eta\right) \tag{4.45}$$

$$+\frac{\varphi_\eta^{-1}}{V_\mathrm{B}}\int_{A_{\eta\omega}}\mathbf{n}_{\eta\omega}\cdot\left(\left(\rho c_p\right)_{\beta,\eta}\left\langle \mathbf{v}_\beta\right\rangle_\eta\tilde{T}_\eta - \mathbf{K}_\eta\cdot\nabla\tilde{T}_\eta - \tilde{\mathbf{K}}_\eta\cdot\nabla\left\{\left\langle T_\eta\right\rangle^\eta\right\}^\eta\right)\mathrm{d}A$$

The term $\dfrac{\varphi_\eta^{-1}\left\{\mathbf{K}_\eta\right\}^\eta}{V_\mathrm{B}}\displaystyle\int_{A_{\eta\omega}}\mathbf{n}_{\eta\omega}\tilde{T}_\eta\mathrm{d}A$ is simplified using SAT:

$$\left\{\nabla\tilde{T}_\eta\right\} = \nabla\left\{\tilde{T}_\eta\right\} + \frac{1}{V_\mathrm{B}}\int_{A_{\eta\omega}}\mathbf{n}_{\eta\omega}\tilde{T}_\eta\mathrm{d}A \xrightarrow{\{\tilde{\psi}\}=0} \frac{1}{V_\mathrm{B}}\int_{A_{\eta\omega}}\mathbf{n}_{\eta\omega}\tilde{T}_\eta\mathrm{d}A = \left\{\nabla\tilde{T}_\eta\right\}$$

$$\rightarrow \frac{\varphi_\eta^{-1}}{V_\mathrm{B}}\int_{A_{\eta\omega}}\mathbf{n}_{\eta\omega}\tilde{T}_\eta\mathrm{d}A = \left\{\nabla\tilde{T}_\eta\right\}^\eta \rightarrow \frac{\varphi_\eta^{-1}\left\{\mathbf{K}_\eta\right\}^\eta}{V_\mathrm{B}}\int_{A_{\eta\omega}}\mathbf{n}_{\eta\omega}\tilde{T}_\eta\mathrm{d}A = \left\{\left\{\mathbf{K}_\eta\right\}^\eta\nabla\tilde{T}_\eta\right\}^\eta \tag{4.46}$$

Substitute of Eq. (4.46) in the second term on the RHS of Eq. (4.45) leads to:

$$\nabla\cdot\left(\frac{\varphi_\eta^{-1}\left\{\mathbf{K}_\eta\right\}^\eta}{V_\mathrm{B}}\int_{A_{\eta\omega}}\mathbf{n}_{\eta\omega}\tilde{T}_\eta\mathrm{d}A + \left\{\tilde{\mathbf{K}}_\eta\cdot\nabla\tilde{T}_\eta\right\}^\eta\right) = \nabla\cdot\left(\left\{\left\{\mathbf{K}_\eta\right\}^\eta\cdot\nabla\tilde{T}_\eta\right\}^\eta + \left\{\tilde{\mathbf{K}}_\eta\cdot\nabla\tilde{T}_\eta\right\}^\eta\right)$$

$$= \nabla\cdot\left\{\left(\left\{\mathbf{K}_\eta\right\}^\eta + \tilde{\mathbf{K}}_\eta\right)\cdot\nabla\tilde{T}_\eta\right\}^\eta = \nabla\cdot\left\{\mathbf{K}_\eta\cdot\nabla\tilde{T}_\eta\right\}^\eta \tag{4.47}$$

Therefore, Eq. (4.45) is simplified to:

$$\left(\rho c_p\right)_\eta \varepsilon_\eta \frac{\partial \tilde{T}_\eta}{\partial t} + \left(\rho c_p\right)_{\beta,\eta} \nabla\cdot\left(\left\langle \mathbf{v}_\beta \right\rangle_\eta \tilde{T}_\eta\right) + \underbrace{\left(\rho c_p\right)_{\beta,\eta} \tilde{\mathbf{v}}_{\beta\eta} \nabla\cdot\left\{\left\langle T_\eta \right\rangle^\eta\right\}}_{\text{convective source}} - \left(\rho c_p\right)_{\beta,\eta} \nabla\cdot\left\{\tilde{\mathbf{v}}_\eta\tilde{T}_\eta\right\}^\eta$$

$$= \nabla\cdot\left(\mathbf{K}_\eta\cdot\nabla\tilde{T}_\eta\right) + \underbrace{\nabla\cdot\left(\tilde{\mathbf{K}}_\eta\cdot\nabla\left\{\left\langle T_\eta\right\rangle^\eta\right\}^\eta\right)}_{\text{conductive source}} - \nabla\cdot\left\{\mathbf{K}_\eta\cdot\nabla\tilde{T}_\eta\right\}^\eta \tag{4.48}$$

$$+\frac{\varphi_\eta^{-1}}{V_\mathrm{B}}\int_{A_{\eta\omega}}\mathbf{n}_{\eta\omega}\cdot\left(\left(\rho c_p\right)_{\beta,\eta}\left\langle \mathbf{v}_\beta\right\rangle_\eta\tilde{T}_\eta - \mathbf{K}_\eta\cdot\nabla\tilde{T}_\eta - \tilde{\mathbf{K}}_\eta\cdot\nabla\left\{\left\langle T_\eta\right\rangle^\eta\right\}^\eta\right)\mathrm{d}A$$

Equation (4.48) is simplified by comparing orders of magnitude of terms appearing in the equation. The orders of magnitudes for the accumulation and conductive terms are

$$\left(\rho c_p\right)_\eta \varepsilon_\eta \frac{\partial \tilde{T}_\eta}{\partial t} = \mathbf{O}\left[\frac{\left(\rho c_p\right)_\eta \varepsilon_\eta \tilde{T}_\eta}{t}\right]$$
$$\nabla \cdot \left(\mathbf{K}_\eta \cdot \nabla \tilde{T}_\eta\right) = \mathbf{O}\left[\frac{K_\eta \tilde{T}_\eta}{l_\eta^2}\right] \tag{4.49}$$

Equation (4.48) becomes quasi-steady for [114]:

$$\frac{K_\eta t}{l_\eta^2 \left(\rho c_p\right)_\eta \varepsilon_\eta} \gg 1 \tag{4.50}$$

This constraint has already been applied on the small-scale, during up-scaling from level A to B. Thus, it can be used at the macro-scale as well. Similar procedure is done for the convective, the large-scale dispersive, and the conductive terms in Eq. (4.48) as below:

$$\left(\rho c_p\right)_{\beta,\eta} \nabla \cdot \left(\left\langle \mathbf{v}_\beta \right\rangle_\eta \tilde{T}_\eta\right) = \mathbf{O}\left[\frac{\left(\rho c_p\right)_{\beta,\eta} \left\langle \mathbf{v}_\beta \right\rangle_\eta \tilde{T}_\eta}{l_\eta}\right] \tag{4.51}$$

$$\left(\rho c_p\right)_{\beta,\eta} \nabla \cdot \left\{\tilde{\mathbf{v}}_\eta \tilde{T}_\eta\right\}^\eta = \mathbf{O}\left[\frac{\left(\rho c_p\right)_{\beta,\eta} \left\langle \mathbf{v}_\beta \right\rangle_\eta \tilde{T}_\eta}{L_\mathrm{c}}\right] \tag{4.52}$$

$$\nabla \cdot \left(\mathbf{K}_\eta \cdot \nabla \tilde{T}_\eta\right) = \mathbf{O}\left[\frac{K_\eta \tilde{T}_\eta}{l_\eta L_\mathrm{c}}\right] \tag{4.53}$$

where L_c is the length-scale for the region averaged temperature. With the constraint $l_\eta, l_\omega \ll L_\mathrm{c}$, it is possible to neglect the large-scale dispersive and the conductive terms. By applying the decomposition presented in Eqs. (4.22) and (4.25) into Eqs. (4.6), (4.7) and (4.11), the boundary conditions for the spatial deviation variation are obtained. Therefore, by applying the order of magnitude analysis (Eqs. (4.49)–(4.53)), the closure problem can be obtained as follows:

$$\left(\rho c_p\right)_{\beta,\eta} \nabla \cdot \left(\left\langle \mathbf{v}_\beta \right\rangle_\eta \tilde{T}_\eta\right) + \underbrace{\left(\rho c_p\right)_{\beta,\eta} \tilde{\mathbf{v}}_{\beta\eta} \nabla \cdot \left\{\left\langle T_\eta \right\rangle^\eta\right\}^\eta}_{\text{convective source}} = \nabla \cdot \left(\mathbf{K}_\eta \cdot \nabla \tilde{T}_\eta\right) + \underbrace{\nabla \cdot \left(\tilde{\mathbf{K}}_\eta \cdot \nabla \left\{\left\langle T_\eta \right\rangle^\eta\right\}^\eta\right)}_{\text{conductive source}} +$$
$$+ \frac{\varphi_\eta^{-1}}{V_\mathrm{B}} \int_{A_{\eta\omega}} \mathbf{n}_{\eta\omega} \cdot \left(\left(\rho c_p\right)_{\beta,\eta} \left\langle \mathbf{v}_\beta \right\rangle_\eta \tilde{T}_\eta - \mathbf{K}_\eta \cdot \nabla \tilde{T}_\eta - \tilde{\mathbf{K}}_\eta \cdot \nabla \left\{\left\langle T_\eta \right\rangle^\eta\right\}^\eta\right) \mathrm{d}A \tag{4.54}$$

B.C.1 $\tilde{T}_\eta = \tilde{T}_\omega + \underbrace{\left(\left\{ \left\langle T_\omega \right\rangle^\omega \right\}^\omega - \left\{ \left\langle T_\eta \right\rangle^\eta \right\}^\eta \right)}_{\text{exchange source}}$, at $A_{\eta\omega}$ (4.55)

B.C.2 $\mathbf{n}_{\eta\omega} \cdot \mathbf{K}_\eta \cdot \nabla \tilde{T}_\eta + \underbrace{\mathbf{n}_{\eta\omega} \cdot \mathbf{K}_\eta \cdot \nabla \left\{ \left\langle T_\eta \right\rangle^\eta \right\}^\eta}_{\text{conductive source}} = \mathbf{n}_{\eta\omega} \cdot \mathbf{K}_\omega \cdot \nabla \tilde{T}_\omega + \underbrace{\mathbf{n}_{\eta\omega} \cdot \mathbf{K}_\omega \cdot \nabla \left\{ \left\langle T_\omega \right\rangle^\omega \right\}^\omega}_{\text{conductive source}}$, at $A_{\eta\omega}$ (4.56)

$$\left(\rho c_p\right)_{\beta,\omega} \nabla \cdot \left(\left\langle \mathbf{v}_\beta \right\rangle_\omega \tilde{T}_\omega \right) + \underbrace{\left(\rho c_p\right)_{\beta,\omega} \tilde{\mathbf{v}}_{\beta\omega} \nabla \cdot \left\{ \left\langle T_\omega \right\rangle^\omega \right\}^\omega}_{\text{convective source}} = \nabla \cdot \left(\mathbf{K}_\omega \cdot \nabla \tilde{T}_\omega \right) + \underbrace{\nabla \cdot \left(\tilde{\mathbf{K}}_\omega \cdot \nabla \left\{ \left\langle T_\omega \right\rangle^\omega \right\}^\omega \right)}_{\text{conductive source}} +$$
$$+ \frac{\varphi_\omega^{-1}}{V_B} \int_{A_{\omega\eta}} \mathbf{n}_{\omega\eta} \cdot \left(\left(\rho c_p\right)_{\beta,\omega} \left\langle \mathbf{v}_\beta \right\rangle_\omega \tilde{T}_\omega - \mathbf{K}_\omega \cdot \nabla \tilde{T}_\omega - \tilde{\mathbf{K}}_\omega \cdot \nabla \left\{ \left\langle T_\omega \right\rangle^\omega \right\}^\omega \right) \mathrm{d}A \quad (4.57)$$

Periodicity: $\tilde{T}_\eta\left(\mathbf{r} + l_i\right) = \tilde{T}_\eta\left(\mathbf{r}\right)$, $\tilde{T}_\omega\left(\mathbf{r} + l_i\right) = \tilde{T}_\omega\left(\mathbf{r}\right)$, $i = 1,2,3$ (4.58)

$\left\{ \tilde{T}_\eta \right\}^\eta = 0$, $\left\{ \tilde{T}_\omega \right\}^\omega = 0$ (4.59)

For Eqs. (4.54)–(4.57), the periodic conditions are applied on spatial deviation temperature. The idea is that the closure problem is only needed to be solved in an REV of a spatially periodic model of a porous medium [109, 211]. In addition to the periodic conditions, the average of the spatial deviation temperatures is required to be zero in order to determine the value of the area integrals in Eqs. (4.54) and (4.57).

It can be observed that in Eqs. (4.54)–(4.57), the convective, conductive and exchange sources are functions of $\nabla \left\{ \left\langle T_\eta \right\rangle^\eta \right\}^\eta$, $\nabla \left\{ \left\langle T_\omega \right\rangle^\omega \right\}^\omega$, and $\left(\left\{ \left\langle T_\omega \right\rangle^\omega \right\}^\omega - \left\{ \left\langle T_\eta \right\rangle^\eta \right\}^\eta \right)$. Therefore, we can represent the spatial deviation temperature in the following forms:

$$\tilde{T}_\eta = \mathbf{b}_{\eta\eta} \cdot \nabla \left\{ \left\langle T_\eta \right\rangle^\eta \right\}^\eta + \mathbf{b}_{\eta\omega} \cdot \nabla \left\{ \left\langle T_\omega \right\rangle^\omega \right\}^\omega + r_\eta \left(\left\{ \left\langle T_\omega \right\rangle^\omega \right\}^\omega - \left\{ \left\langle T_\eta \right\rangle^\eta \right\}^\eta \right) \quad (4.60)$$

$$\tilde{T}_\omega = \mathbf{b}_{\omega\eta} \cdot \nabla \left\{ \left\langle T_\eta \right\rangle^\eta \right\}^\eta + \mathbf{b}_{\omega\omega} \cdot \nabla \left\{ \left\langle T_\omega \right\rangle^\omega \right\}^\omega + r_\omega \left(\left\{ \left\langle T_\omega \right\rangle^\omega \right\}^\omega - \left\{ \left\langle T_\eta \right\rangle^\eta \right\}^\eta \right) \quad (4.61)$$

Where $\mathbf{b}_{\eta\eta}$, $\mathbf{b}_{\eta\omega}$, r_η, $\mathbf{b}_{\omega\eta}$, $\mathbf{b}_{\omega\omega}$ and r_ω are closure variables. Three closure problems are required to have a solution for the closure variables.

Closure problem I

The first closure problem is related to the source $\nabla\left\{\left\langle T_\eta\right\rangle^\eta\right\}^\eta$, and is given by:

$$\left(\rho c_p\right)_{\beta,\eta}\nabla\cdot\left(\left\langle\mathbf{v}_\beta\right\rangle_\eta\mathbf{b}_{\eta\eta}\right)+\left(\rho c_p\right)_{\beta,\eta}\tilde{\mathbf{v}}_{\beta\eta}=\nabla\cdot\left(\mathbf{K}_\eta\cdot\nabla\mathbf{b}_{\eta\eta}\right)+\nabla\cdot\tilde{\mathbf{K}}_\omega-\varphi_\eta^{-1}\mathbf{c}_{\eta\eta} \tag{4.62}$$

B.C.1 $\mathbf{b}_{\eta\eta}=\mathbf{b}_{\eta\omega}$, at $A_{\eta\omega}$ (4.63)

B.C.2 $\mathbf{n}_{\eta\omega}\cdot\mathbf{K}_\eta\cdot\nabla\mathbf{b}_{\eta\eta}+\mathbf{n}_{\eta\omega}\cdot\mathbf{K}_\eta=\mathbf{n}_{\eta\omega}\cdot\mathbf{K}_\omega\cdot\nabla\mathbf{b}_{\omega\eta}$, at $A_{\eta\omega}$ (4.64)

$$\left(\rho c_p\right)_{\beta,\omega}\nabla\cdot\left(\left\langle\mathbf{v}_\beta\right\rangle_\omega\mathbf{b}_{\omega\eta}\right)=\nabla\cdot\left(\mathbf{K}_\omega\cdot\nabla\mathbf{b}_{\omega\eta}\right)-\varphi_\omega^{-1}\mathbf{c}_{\omega\eta} \tag{4.65}$$

Periodicity: $\mathbf{b}_{\eta\eta}\left(\mathbf{r}+l_i\right)=\mathbf{b}_{\eta\eta}\left(\mathbf{r}\right)$, $\mathbf{b}_{\omega\eta}\left(\mathbf{r}+l_i\right)=\mathbf{b}_{\omega\eta}\left(\mathbf{r}\right)$, $i=1,2,3$ (4.66)

$$\left\{\mathbf{b}_{\eta\eta}\right\}^\eta=0\ ,\ \left\{\mathbf{b}_{\omega\eta}\right\}^\omega=0 \tag{4.67}$$

$$\mathbf{c}_{\eta\eta}=-\frac{1}{V_\mathrm{B}}\int_{A_{\eta\omega}}\mathbf{n}_{\eta\omega}\cdot\left(\left(\rho c_p\right)_{\beta,\eta}\left\langle\mathbf{v}_\beta\right\rangle_\eta\mathbf{b}_{\eta\eta}-\mathbf{K}_\eta\cdot\nabla\mathbf{b}_{\eta\eta}-\tilde{\mathbf{K}}_\eta\right)\mathrm{d}A \tag{4.68}$$

$$\mathbf{c}_{\omega\eta}=-\frac{1}{V_\mathrm{B}}\int_{A_{\omega\eta}}\mathbf{n}_{\omega\eta}\cdot\left(\left(\rho c_p\right)_{\beta,\omega}\left\langle\mathbf{v}_\beta\right\rangle_\omega\mathbf{b}_{\omega\eta}-\mathbf{K}_\omega\cdot\nabla\mathbf{b}_{\omega\eta}\right)\mathrm{d}A \tag{4.69}$$

Closure problem II

The second closure problem is related to the source $\nabla\left\{\left\langle T_\omega\right\rangle^\omega\right\}^\omega$, and is given by:

$$\left(\rho c_p\right)_{\beta,\eta}\nabla\cdot\left(\left\langle\mathbf{v}_\beta\right\rangle_\eta\mathbf{b}_{\eta\omega}\right)=\nabla\cdot\left(\mathbf{K}_\eta\cdot\nabla\mathbf{b}_{\eta\omega}\right)-\varphi_\eta^{-1}\mathbf{c}_{\eta\omega} \tag{4.70}$$

B.C.1 $\mathbf{b}_{\eta\omega}=\mathbf{b}_{\omega\omega}$, at $A_{\eta\omega}$ (4.71)

B.C.2 $\mathbf{n}_{\eta\omega}\cdot\mathbf{K}_\eta\cdot\nabla\mathbf{b}_{\eta\omega}=\mathbf{n}_{\eta\omega}\cdot\mathbf{K}_\omega\cdot\nabla\mathbf{b}_{\omega\omega}+\mathbf{n}_{\eta\omega}\mathbf{K}_\omega$, at $A_{\eta\omega}$ (4.72)

$$\left(\rho c_p\right)_{\beta,\omega}\nabla\cdot\left(\left\langle\mathbf{v}_\beta\right\rangle_\omega\mathbf{b}_{\omega\omega}\right)+\left(\rho c_p\right)_{\beta,\omega}\tilde{\mathbf{v}}_{\beta\omega}=\nabla\cdot\left(\mathbf{K}_\omega\cdot\nabla\mathbf{b}_{\omega\omega}\right)-\varphi_\omega^{-1}\mathbf{c}_{\omega\omega} \tag{4.73}$$

Periodicity: $\mathbf{b}_{\eta\omega}\left(\mathbf{r}+l_i\right)=\mathbf{b}_{\eta\omega}\left(\mathbf{r}\right)$, $\mathbf{b}_{\omega\omega}\left(\mathbf{r}+l_i\right)=\mathbf{b}_{\omega\omega}\left(\mathbf{r}\right)$, , $i=1,2,3$ (4.74)

$$\left\{\mathbf{b}_{\eta\omega}\right\}^\eta=0\ ,\ \left\{\mathbf{b}_{\omega\omega}\right\}^\omega=0 \tag{4.75}$$

$$\mathbf{c}_{\eta\omega}=-\frac{1}{V_\mathrm{B}}\int_{A_{\eta\omega}}\mathbf{n}_{\eta\omega}\cdot\left(\left(\rho c_p\right)_{\beta,\eta}\left\langle\mathbf{v}_\beta\right\rangle_\eta\mathbf{b}_{\eta\omega}-\mathbf{K}_\eta\cdot\nabla\mathbf{b}_{\eta\omega}\right)\mathrm{d}A \tag{4.76}$$

$$\mathbf{c}_{\omega\eta} = -\frac{1}{V_{\mathrm{B}}}\int_{A_{\omega\eta}} \mathbf{n}_{\omega\eta}\cdot\left(\left(\rho c_p\right)_{\beta,\omega}\left\langle \mathbf{v}_\beta\right\rangle_\omega \mathbf{b}_{\omega\omega} - \mathbf{K}_\omega\cdot\nabla\mathbf{b}_{\omega\omega} - \mathbf{K}_\omega\right)\mathrm{d}A \tag{4.77}$$

Closure problem III

The third closure problem originates from the exchange source $\left(\left\{\left\langle T_\omega\right\rangle^\omega\right\}^\omega - \left\{\left\langle T_\eta\right\rangle^\eta\right\}^\eta\right)$, and is given by:

$$\left(\rho c_p\right)_{\beta,\eta}\nabla\cdot\left(\left\langle \mathbf{v}_\beta\right\rangle_\eta r_\eta\right) = \nabla\cdot\left(\mathbf{K}_\eta\cdot\nabla r_\eta\right) - \varphi_\eta^{-1}\alpha \tag{4.78}$$

B.C.1 $r_\eta = r_\omega + 1$, at $A_{\eta\omega}$ (4.79)

B.C.2 $\mathbf{n}_{\eta\omega}\cdot\mathbf{K}_\eta\cdot\nabla r_\eta = \mathbf{n}_{\eta\omega}\cdot\mathbf{K}_\omega\cdot\nabla r_\omega$, at $A_{\eta\omega}$ (4.80)

$$\left(\rho c_p\right)_{\beta,\omega}\nabla\cdot\left(\left\langle \mathbf{v}_\beta\right\rangle_\omega r_\omega\right) = \nabla\cdot\left(\mathbf{K}_\omega\cdot\nabla r_\omega\right) - \varphi_\omega^{-1}\alpha \tag{4.81}$$

Periodicity: $r_\eta\left(\mathbf{r}+l_i\right) = r_\eta\left(\mathbf{r}\right)$, $r_\omega\left(\mathbf{r}+l_i\right) = r_\omega\left(\mathbf{r}\right)$, $i = 1,2,3$ (4.82)

$$\left\{r_\eta\right\}^\eta = 0 \ , \ \left\{r_\omega\right\}^\omega = 0 \tag{4.83}$$

where α is:

$$\begin{aligned}\alpha &= -\frac{1}{V_{\mathrm{B}}}\int_{A_{\eta\omega}} \mathbf{n}_{\eta\omega}\cdot\left(\left(\rho c_p\right)_{\beta,\eta}\left\langle \mathbf{v}_\beta\right\rangle_\eta r_\eta - \mathbf{K}_\eta\cdot\nabla r_\eta\right)\mathrm{d}A \\ &= +\frac{1}{V_{\mathrm{B}}}\int_{A_{\omega\eta}} \mathbf{n}_{\omega\eta}\cdot\left(\left(\rho c_p\right)_{\beta,\omega}\left\langle \mathbf{v}_\beta\right\rangle_\omega r_\omega - \mathbf{K}_\omega\cdot\nabla r_\omega\right)\mathrm{d}A\end{aligned} \tag{4.84}$$

We define new variables as below:

$$s_\eta = r_\eta \text{ and } s_\omega = r_\omega + 1 \tag{4.85}$$

Thus, the third closure problem takes the form shown next.

Closure problem III'

$$\left(\rho c_p\right)_{\beta,\eta}\nabla\cdot\left(\left\langle \mathbf{v}_\beta\right\rangle_\eta s_\eta\right) = \nabla\cdot\left(\mathbf{K}_\eta\cdot\nabla s_\eta\right) - \varphi_\eta^{-1}\alpha \tag{4.86}$$

B.C.1 $s_\eta = s_\omega$, at $A_{\eta\omega}$ (4.87)

B.C.2 $\mathbf{n}_{\eta\omega}\cdot\mathbf{K}_\eta\cdot\nabla s_\eta = \mathbf{n}_{\eta\omega}\cdot\mathbf{K}_\omega\cdot\nabla s_\omega$, at $A_{\eta\omega}$ (4.88)

$$\left(\rho c_p\right)_{\beta,\omega} \nabla\cdot\left(\left\langle \mathbf{v}_\beta \right\rangle_\omega s_\omega\right) = \nabla\cdot\left(\mathbf{K}_\omega\cdot\nabla s_\omega\right) - \varphi_\omega^{-1}\alpha \tag{4.89}$$

Periodicity: $s_\eta\left(\mathbf{r}+l_i\right) = s_\eta\left(\mathbf{r}\right)$, $s_\omega\left(\mathbf{r}+l_i\right) = s_\omega\left(\mathbf{r}\right)$, $i=1,2,3$ (4.90)

$$\left\{s_\eta\right\}^\eta = 0 \ , \ \left\{s_\omega\right\}^\omega = 0 \tag{4.91}$$

$$\alpha = -\frac{1}{V_\mathrm{B}}\int\limits_{A_{\eta\omega}} \mathbf{n}_{\eta\omega}\cdot\left(\left(\rho c_p\right)_{\beta,\eta}\left\langle \mathbf{v}_\beta\right\rangle_\eta s_\eta - \mathbf{K}_\eta\cdot\nabla s_\eta\right)\mathrm{d}A \tag{4.92}$$

4.6. Up-scaled energy equation

By substituting Eq. (4.60) into (4.37), the closed from energy equation (i.e. the up-scaled volume-averaged energy equation at level C) for the η-region becomes:

$$\begin{aligned}
&\underbrace{\left(\rho c_p\right)_\eta \varepsilon_\eta\varphi_\eta \frac{\partial\left\{\left\langle T_\eta\right\rangle^\eta\right\}^\eta}{\partial t}}_{\text{accumulation}} + \underbrace{\left(\rho c_p\right)_{\beta,\eta}\left(\nabla\cdot\left(\varphi_\eta\left\{\left\langle \mathbf{v}_\beta\right\rangle_\eta\right\}^\eta\left\{\left\langle T_\eta\right\rangle^\eta\right\}^\eta\right)\right)}_{\text{convection}} \\
&\underbrace{-\nabla\cdot\left(\mathbf{d}_\eta\left(\left\{\left\langle T_\eta\right\rangle^\eta\right\}^\eta - \left\{\left\langle T_\omega\right\rangle^\omega\right\}^\omega\right)\right)}_{\text{traditional energy source}} \underbrace{-\mathbf{u}_{\eta\eta}.\nabla\left\{\left\langle T_\eta\right\rangle^\eta\right\}^\eta - \mathbf{u}_{\eta\omega}.\nabla\left\{\left\langle T_\omega\right\rangle^\omega\right\}^\omega}_{\text{non-traditional convection}} \\
&= \underbrace{\nabla\cdot\left(\mathbf{K}_{\eta\eta}\cdot\nabla\left\{\left\langle T_\eta\right\rangle^\eta\right\}^\eta\right)}_{\text{dominant thermal dispersion}} + \underbrace{\nabla\cdot\left(\mathbf{K}_{\eta\omega}\nabla\left\{\left\langle T_\omega\right\rangle^\omega\right\}^\omega\right)}_{\text{coupling thermal dispersion}} \underbrace{-\alpha\left(\left\{\left\langle T_\eta\right\rangle^\eta\right\}^\eta - \left\{\left\langle T_\omega\right\rangle^\omega\right\}^\omega\right)}_{\text{inter-region energy exchange}}
\end{aligned} \tag{4.93}$$

where the coefficients are defined as:

$$\mathbf{d}_\eta = \varphi_\eta\left\{\tilde{\mathbf{v}}_{\beta\eta}s_\eta - \mathbf{K}_\eta\cdot\nabla s_\eta\right\}^\eta \tag{4.94}$$

$$\mathbf{u}_{\eta\eta} = -\frac{1}{V_\mathrm{B}}\int\limits_{A_{\eta\omega}} \mathbf{n}_{\eta\omega}\cdot\left(\left(\rho c_p\right)_{\beta,\eta}\left\langle \mathbf{v}_\beta\right\rangle_\eta \mathbf{b}_{\eta\eta} - \mathbf{K}_\eta\cdot\nabla\mathbf{b}_{\eta\eta} - \tilde{\mathbf{K}}_\eta\right)\mathrm{d}A \tag{4.95}$$

$$\mathbf{u}_{\eta\omega} = -\frac{1}{V_\mathrm{B}}\int\limits_{A_{\eta\omega}} \mathbf{n}_{\eta\omega}\cdot\left(\left(\rho c_p\right)_{\beta,\eta}\left\langle \mathbf{v}_\beta\right\rangle_\eta \mathbf{b}_{\eta\omega} - \mathbf{K}_\eta\cdot\nabla\mathbf{b}_{\eta\omega}\right)\mathrm{d}A \tag{4.96}$$

$$\mathbf{K}_{\eta\eta} = \varphi_\eta\left\{\mathbf{K}_\eta\cdot\left(I+\nabla\mathbf{b}_{\eta\eta}\right) - \tilde{\mathbf{v}}_{\beta\eta}\mathbf{b}_{\eta\eta}\right\}^\eta \tag{4.97}$$

$$\mathbf{K}_{\eta\omega} = \varphi_\eta\left\{\mathbf{K}_\eta\cdot\nabla\mathbf{b}_{\eta\omega} - \tilde{\mathbf{v}}_{\beta\eta}\mathbf{b}_{\eta\omega}\right\}^\eta \tag{4.98}$$

$$\alpha = -\frac{1}{V_\mathrm{B}}\int\limits_{A_{\eta\omega}} \mathbf{n}_{\eta\omega}\cdot\left(\left(\rho c_p\right)_{\beta,\eta}\left\langle \mathbf{v}_\beta\right\rangle_\eta s_\eta - \mathbf{K}_\eta\cdot\nabla s_\eta\right)\mathrm{d}A \tag{4.99}$$

In addition, by substituting Eq. (4.61) into (4.38), the closed form of energy equation for the ω-region becomes:

$$\underbrace{\left(\rho c_p\right)_{\omega}\varepsilon_{\omega}\varphi_{\omega}\frac{\partial\left\{\left\langle T_{\omega}\right\rangle^{\omega}\right\}^{\omega}}{\partial t}}_{\text{accumulation}}+\underbrace{\left(\rho c_p\right)_{\beta,\omega}\left(\nabla\cdot\left(\varphi_{\omega}\left\{\left\langle \mathbf{v}_{\beta}\right\rangle_{\omega}\right\}^{\omega}\left\{\left\langle T_{\omega}\right\rangle^{\omega}\right\}^{\omega}\right)\right)}_{\text{convection}}$$
$$\underbrace{-\nabla\cdot\left(\mathbf{d}_{\omega}\left(\left\{\left\langle T_{\omega}\right\rangle^{\omega}\right\}^{\omega}-\left\{\left\langle T_{\eta}\right\rangle^{\eta}\right\}^{\eta}\right)\right)}_{\text{traditional energy source}}\underbrace{-\mathbf{u}_{\omega\omega}.\nabla\left\{\left\langle T_{\omega}\right\rangle^{\omega}\right\}^{\omega}-\mathbf{u}_{\omega\eta}.\nabla\left\{\left\langle T_{\eta}\right\rangle^{\eta}\right\}^{\eta}}_{\text{non-traditional convection}} \tag{4.100}$$
$$=\underbrace{\nabla\cdot\left(\mathbf{K}_{\omega\omega}\cdot\nabla\left\{\left\langle T_{\omega}\right\rangle^{\omega}\right\}^{\omega}\right)}_{\text{dominant thermal dispersion}}+\underbrace{\nabla\cdot\left(\mathbf{K}_{\omega\eta}\nabla\left\{\left\langle T_{\omega}\right\rangle^{\omega}\right\}^{\omega}\right)}_{\text{coupling thermal dispersion}}\underbrace{-\alpha\left(\left\{\left\langle T_{\omega}\right\rangle^{\omega}\right\}^{\omega}-\left\{\left\langle T_{\eta}\right\rangle^{\eta}\right\}^{\eta}\right)}_{\text{inter-region energy exchange}}$$

where the coefficients are defined as:

$$\mathbf{d}_{\omega}=\varphi_{\omega}\left\{\tilde{\mathbf{v}}_{\beta\omega}s_{\omega}-\mathbf{K}_{\omega}\cdot\nabla s_{\omega}\right\}^{\omega} \tag{4.101}$$

$$\mathbf{u}_{\omega\omega}=-\frac{1}{V_{\mathrm{B}}}\int_{A_{\omega\eta}}\mathbf{n}_{\omega\eta}\cdot\left(\left(\rho c_p\right)_{\beta,\omega}\left\langle\mathbf{v}_{\beta}\right\rangle_{\omega}\mathbf{b}_{\omega\omega}-\mathbf{K}_{\omega}\cdot\nabla\mathbf{b}_{\omega\omega}-\tilde{\mathbf{K}}_{\omega}\right)\mathrm{d}A \tag{4.102}$$

$$\mathbf{u}_{\omega\eta}=-\frac{1}{V_{\mathrm{B}}}\int_{A_{\omega\eta}}\mathbf{n}_{\omega\eta}\cdot\left(\left(\rho c_p\right)_{\beta,\omega}\left\langle\mathbf{v}_{\beta}\right\rangle_{\omega}\mathbf{b}_{\omega\eta}-\mathbf{K}_{\omega}\cdot\nabla\mathbf{b}_{\omega\eta}\right)\mathrm{d}A \tag{4.103}$$

$$\mathbf{K}_{\omega\omega}=\varphi_{\omega}\left\{\mathbf{K}_{\omega}\cdot\left(I+\nabla\mathbf{b}_{\omega\omega}\right)-\tilde{\mathbf{v}}_{\beta\omega}\mathbf{b}_{\omega\omega}\right\}^{\omega} \tag{4.104}$$

$$\mathbf{K}_{\omega\eta}=\varphi_{\omega}\left\{\mathbf{K}_{\omega}\cdot\nabla\mathbf{b}_{\omega\eta}-\tilde{\mathbf{v}}_{\beta\omega}\mathbf{b}_{\omega\eta}\right\}^{\omega} \tag{4.105}$$

$$\alpha=-\frac{1}{V_{\mathrm{B}}}\int_{A_{\omega\eta}}\mathbf{n}_{\omega\eta}\cdot\left(\left(\rho c_p\right)_{\beta,\omega}\left\langle\mathbf{v}_{\beta}\right\rangle_{\omega}s_{\omega}-\mathbf{K}_{\omega}\cdot\nabla s_{\omega}\right)\mathrm{d}A \tag{4.106}$$

In Eqs. (4.93) and (4.100), the heat transfer in the dual-scale porous medium is controlled by energy transport mechanisms of convection, conduction, and inter-region heat exchange. They are quantified via the effective transport coefficients defined in Eqs. (4.94)–(4.99) and Eqs. (4.101)–(4.106). In the above equations, the coefficients $\mathbf{K}_{\eta\eta}$ and $\mathbf{K}_{\eta\omega}$ are referred to as the dominant thermal dispersion tensors. The coefficients $\mathbf{K}_{\eta\omega}$ and $\mathbf{K}_{\omega\eta}$ are the coupling thermal dispersion tensors. In the two non-traditional convective transport terms in Eqs. (4.93) and (4.100), the coefficients $\mathbf{u}_{\eta\eta}$, $\mathbf{u}_{\eta\omega}$, $\mathbf{u}_{\omega\omega}$, $\mathbf{u}_{\omega\eta}$ are the pseudo-velocity vectors. The

coefficients $\mathbf{d}_\eta$ and $\mathbf{d}_\omega$ are related to the energy source terms. The parameter α is the inter-region energy exchange coefficient.

4.7. Summary

In this chapter, a theoretical approach is used to present mathematical model of heat transfer in dual-scale porous structures. The volume-averaging method was applied to the convective–conductive energy conservation equation to derive the large-scale equations. The closure problems were introduced along with the closure variables to establish the two-equation model for heat transfer of dual-scale porous media. It possible for the users intending to perform numerical simulation at level C, such as reactor level, to conveniently apply the up-scaled two-equation model along with the effective coefficients to model the heat transfer in the dual-scale porous media. The effective coefficients are calculated using the solution of the closure problems for an REV of a given dual-porosity medium. In the following chapter, the effective coefficients for given dual-scale porous media are numerically determined. The accuracy of using the up-scaled two-equation model with effective coefficients, Eqs. (4.93) and (4.100), is examined by comparing the results of the volume-averaged model to those of pore-level simulations.

Chapter 5

Numerical determination of effective heat transfer coefficients

This chapter presents the numerical determination of the effective heat transfer coefficients introduced in Chapter 4 for air flowing in packed beds of porous spherical particles. Firstly, the introduced closure problems defined in Section 4.5 are numerically solved in 3D unit cells of packed bed of porous particles, representing the dual-scale porous medium. Then, the solution of the closure problem is used to determine the effective coefficients appearing in the up-scaled energy equation. Finally, the results of the up-scaled model are compared with those of the pore-level simulations (at the meso-scale) to investigate the accuracy of the up-scaled model.

5.1. Solution procedure of the closure problems

The effective coefficients defined in Eqs. (4.94)–(4.99) and Eqs. (4.101)–(4.106), which are related to the two-equation model of conductive–convective heat transfer in a dual-scale porous medium presented in Eqs. (4.93) and (4.100), are functions of closure variables $\mathbf{b}_{\eta\eta}$, $\mathbf{b}_{\eta\omega}$, r_{η}, $\mathbf{b}_{\omega\eta}$, $\mathbf{b}_{\omega\omega}$, and $\mathbf{b}_{\omega\omega}$. Therefore, the closure problems introduced in Section 4.5 are needed to be solved numerically for an REV of a dual-scale porous medium in order to determine the effective coefficients. In the method of volume averaging, it is assumed that the representative cells can be periodically repeated in all directions to produce the entire desired porous medium. Each closure problem is in the form of a steady-state boundary value problem with two variables coupled through the inter-region flux term. The solutions to the closure problems are unique depending on the structure of the porous medium. The procedure of determining the effective coefficients in a dual-scale porous medium is:

1) Define the REV of a dual-scale porous system

2) Calculate the pore-scale periodic velocity field in the REV
3) Apply the velocity field in the closure problems
4) Solve the closure problems (boundary value problems)
5) Calculate effective coefficients based on the closure variables field

In the first step, the REV of the given dual-scale porous medium is defined. The advection terms appears in the closure problems, and the integral sources $\mathbf{c}_{\eta\eta}$, $\mathbf{c}_{\omega\eta}$, $\mathbf{c}_{\eta\omega}$, $\mathbf{c}_{\omega\omega}$ and α are functions of velocity field. Thus, we need to calculate the pore-level velocity field in the REV. Then, we apply the velocity fields as the inputs to the closure problems. In the next step, the closure problems are solved in both regions separately from the up-scaled two-equation model of heat transfer. In the final step, the effective coefficients defined in Eqs. (4.94)–(4.99) and Eqs. (4.101)–(4.106) are determined using the solution of the closure problems.

5.1.1. Case study definition

We emphasise that the two-equation model developed in Chapter 4 is for a general case of η- and ω-regions being porous but with different characteristic length-scales. As discussed in Section 4.2, a specific case of $\varepsilon_\eta = 1$ and $0 < \varepsilon_\omega < 1$ is considered in this work.

The model dual-porosity medium is depicted in Figure 5.1. It consists of a packed bed of porous spherical particles. The inter-particle region, referred to as the η-region, contains a fluid only. The intra-particle region, referred to as the ω-region, contains a porous domain. The mathematical model developed in Chapter 4 and the procedure of determining the effective coefficients presented in Section 5.1 can be used for any given dual-scale porous medium. However, each specific dual-scale porous medium has its own unique solution of the closure problems, and consequently, its own unique effective coefficients. Therefore, the dual-scale porous medium used in this study has been chosen as a specific case due to its application in industry in general and in solar thermochemistry in particular. Thus, this section focuses on the procedure of solving the closure problems and determining the effective coefficients.

Figure 5.1 illustrates the REVs of dual-scale porous media consisting of packed bed of porous spherical particles with SC, BCC, and FCC packing arrangement. By utilizing the unit cell symmetry, a quarter of the selected geometries sufficies to obtain the numerical solution

at a reduced computational cost. To calculate the fully-developed velocity fields—as inputs for solving the closure problems—the periodic boundary conditions are applied on the front and back faces of the domains shown in Figure 5.1. Symmetry boundary conditions are on the lateral faces. In Figure 5.1a, the periodic boundary conditions are applied on the faces $z=0$ and $z=l_{\mathrm{SC}}$, and the symmetry boundary conditions are applied on the faces $x=0$, $x=l_{\mathrm{SC}}/2$, $y=0$ and $y=l_{\mathrm{SC}}/2$. The symmetry boundary conditions on the lateral faces are justified assumptions due to the reasons below:

i. The unit cells of the packed bed shown in Figure 5.2 are symmetrical.
ii. Fluid flow is in *z* direction
iii. Normal velocity component at the lateral faces can be neglected.

The use of symmetry boundary conditions for fluid flow is a well-established procedure for simulating the transport phenomena in REVs of porous media [56, 164, 215–218]. In the case of calculating the fluid flow, constant mass flow rate in the *z* direction is considered for the periodic boundary condition, which forces equivalent velocity profiles at the front and back faces of the domains (at the planes $z=0$ and $z=l_{\mathrm{SC}}$). Same conditions are applied for solving the closure problems, namely periodicity for front and back faces, and symmetry for the lateral faces. The symmetry boundary condition at each face enforces the values of the closure variables on the given face to become equivalent to those on the faces mirrored by the symmetry plane. For instance, consider Figure 5.1a. The symmetry condition is applied on the plane $x=l_{\mathrm{SC}}/2$. Thus, this plane reproduces the values of closure variables being calculated in its front. Consequently, the values of closure variables on plane $x=l_{\mathrm{SC}}$ are exactly similar to those calculated on plane $x=0$. Therefore, the periodic conditions of the closure variables are satisfied for the whole representative unit cells shown in the top row of Figure 5.1 according to Eqs. (4.68), (4.74) and (4.90). This is a common procedure within the volume-averaging framework [109].

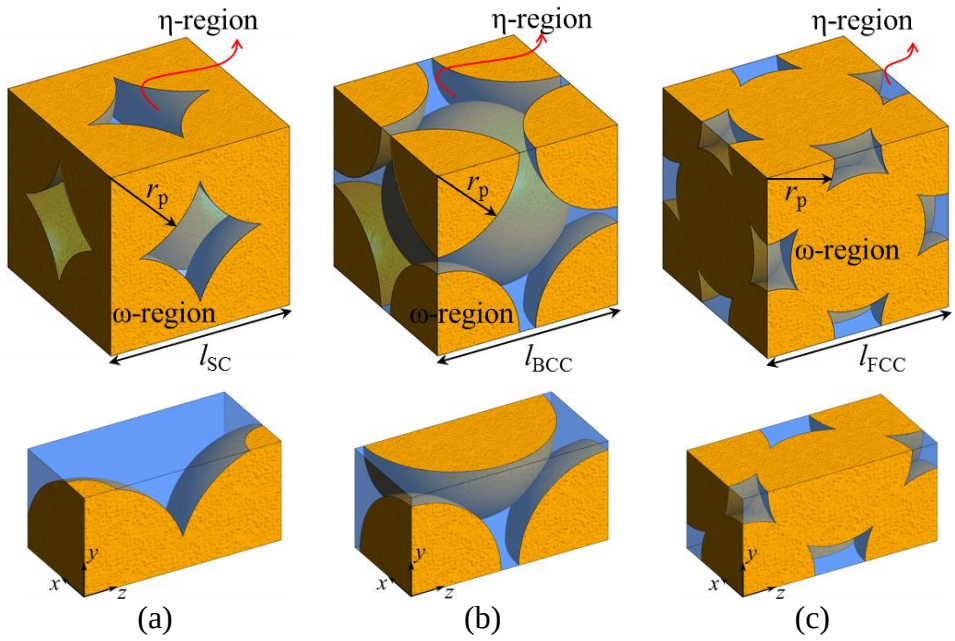

Figure 5.1. Representative 3D unit cells and the computational domain used to solve the closure problem for (a) SC, (b) BCC, and (c) FCC packing arrangements.

Table 5.1 summarises the closure problem parameters for the considered model medium consisting of a packed bed of porous spherical particles. Because the two-equation volume-averaged model derived in Chapter 4 is generally applicable to dual-scale porous media, two different values were chosen for the permeability of the porous particles of the packed bed (ω-region) as shown in Table 5.1. These values are chosen to show the general character of the two-equation volume-averaged model. Thereby, one of the values for permeability is in the order of those reported in Table 3.2. The other one is higher than those reported in Table 3.2. Therefore, the case studies and the values of the relevant parameters presented in Table 3.2 are only chosen for the sake of investigating the fidelity of the model by performing numerical experiment. Note that the permeability of a porous medium is a function of many factors, including pore size, porosity and tortuosity. From the theoretical standpoint, even if the porosity of a porous structure remains constant, the permeability of the medium can still be tuned by changing the pore size and/or tortuosity. Hence, changing the value of permeability at constant porosity is justified.

Table 5.1. Parameters related to the solution of the closure problems.

Parameter	**Value**
Permeability of ω-region (K_ω)	10^{-9} and 10^{-11} (m^2)
Porosity of η-region (ε_η)	1
Porosity of ω-region (ε_ω)	0.5
Flowing fluid	air
Solid to fluid thermal conductivity ratio in ω-region $\left(k_s/k_f\right)_\omega$	10 and 100

5.1.2. Velocity field calculation

To calculate the pore-level velocity field at level B (see Figure 4.1), the mass and momentum conservation equations are solved for the fluid. Only a narrow range of temperatures is considered to neglect the effect of temperature on thermophysical properties of the fluid.

Governing equations

In the inter-particle region (η-region), the traditional mass and momentum equation are solved. For the intra-particle region (ω-region), volume-averaged mass and momentum equations with the Darcy term are solved considering the values of permeability of ω-region presented in Table 5.1. For the inter-particle region (η-region), the conservation equations of mass and momentum for steady flow of an incompressible Newtonian fluid read:

$$\nabla \cdot \mathbf{v}_\eta = 0 \tag{5.1}$$

$$\rho_\eta \nabla \cdot \left(\mathbf{v}_\eta \mathbf{v}_\eta\right) = -\nabla p_\eta + \mu_\eta \nabla^2 \mathbf{v}_\eta \tag{5.2}$$

where $\mathbf{v}_\eta$ and p_η are the η-region velocity vector and the pressure, respectively. For intra-particle region (ω-region), the volume-averaged mass and momentum conservation equations are solved to model the fluid flow within the small pores of the spheres as below:

$$\nabla \cdot \left\langle \mathbf{v}_\omega \right\rangle = 0 \tag{5.3}$$

$$\frac{\rho_\omega}{\varepsilon_\omega} \nabla \cdot \left(\left\langle \mathbf{v}_\omega \right\rangle\right) = -\varepsilon_\omega \nabla \left\langle p_\omega \right\rangle^\omega + \mu_\omega \nabla^2 \left\langle \mathbf{v}_\omega \right\rangle - \frac{\varepsilon_\omega \mu_\omega}{k_\omega} \left\langle \mathbf{v}_\omega \right\rangle \tag{5.4}$$

where ε_ω is the porosity of the spherical particles of the packed bed, $\left\langle \mathbf{v}_\omega \right\rangle$ is the superficial average of velocity inside the spherical particles, and $\left\langle p_\omega \right\rangle^\omega$ is the intrinsic average of the pressure. The third term on the right hand side of Eq. (5.4) is the Darcy term which describes

the microscopic viscous force caused by interaction between the fluid and solid constituents in the ω-region.

Boundary and interface conditions

For the fluid flow simulations, the periodic boundary conditions are applied on the front and back faces of the domain in *z* direction to obtain the fully-developed velocity field. The symmetry boundary conditions are applied on the lateral faces of the domain (Figure 5.1). Interface conditions are needed to couple the momentum and mass transfer phenomena between the homogenous fluid flowing in inter-particle region and the fluid flowing in the porous spherical particles. For the interface between these two regions, the conditions of continuity of velocity and interfacial stress are applied as below [120, 207, 208]:

$$\mathbf{v}_\eta = \langle \mathbf{v}_\omega \rangle \tag{5.5}$$

$$\mu_\eta \left(\frac{\partial u}{\partial y} + \frac{\partial v}{\partial x} \right)_\eta = \frac{\mu_\omega}{\varepsilon_\omega} \left[\frac{\partial \langle u \rangle}{\partial y} + \frac{\partial \langle v \rangle}{\partial x} \right]_\omega \tag{5.6}$$

$$\mu_\eta \left(\frac{\partial w}{\partial y} + \frac{\partial v}{\partial z} \right)_\eta = \frac{\mu_\omega}{\varepsilon_\omega} \left[\frac{\partial \langle w \rangle}{\partial y} + \frac{\partial \langle v \rangle}{\partial z} \right]_\omega \tag{5.7}$$

$$\mu_\mathrm{f} \left(\frac{\partial w}{\partial x} + \frac{\partial u}{\partial z} \right) = \frac{\mu_\mathrm{f}}{\varepsilon} \left[\frac{\partial \langle w_\mathrm{p} \rangle}{\partial x} + \frac{\partial \langle u_\mathrm{p} \rangle}{\partial z} \right]_\mathrm{p} \tag{5.8}$$

$$-p_\eta = -\langle p_\omega \rangle^\omega \tag{5.9}$$

where u, v and w are the *x*, *y* and *z* direction velocity components, respectively.

Numerical method, mesh independency analysis and validation

The CFD code ANSYS FLUENT 17.1 is used to solve the governing equations using the finite volume method [209]. The 3D computational domain is discretised using tetrahedral cells with meshing refinement near the η–ω interface due to the presence of large velocity gradients. Figure 5.2 shows the meshing of the computational domain depicted in Figure 5.1a for SC packing arrangement. The pressure–velocity coupling is resolved by the SIMPLE algorithm, and the convection terms are discretised using the second order upwind scheme [210].

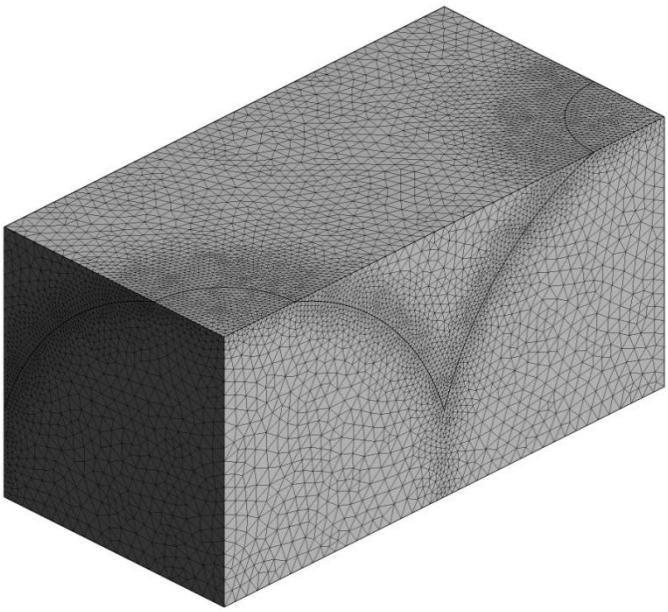

Figure 5.2. Meshing of the computational domain for SC packing arrangement.

Mesh independency analysis has been performed to ensure the results do not depend on the selected spatial discretisation. The total number of mesh elements for the dual-scale porous structures are varied from about 20,000 to 300,000. Velocity at different locations as well as the pressure drop per unit length of the packed bed are selected as the parameters to examine the grid independency. For instance, Figure 5.3 shows the values of pressure drop per unit length of the packed bed with SC arrangement in terms of number of mesh elements for the case of Re_p=5 and $K_\omega = 10^{-11}\,m^2$. Increasing the mesh elements to >200,000 affects the value of pressure gradient by less than 3%.

In order to show that the solver is consistent in fluid flow problem for conjugate fluid–porous domains, the numerical results obtained from current study is compared with the experimental ones reported by Leong et al. [125] for porous graphite foam. For validation, the conditions are kept similar to those mentioned in [125]. As seen in Figure 5.4, there is a good agreement between the results, which indicates that the solver is consistent for such problem.

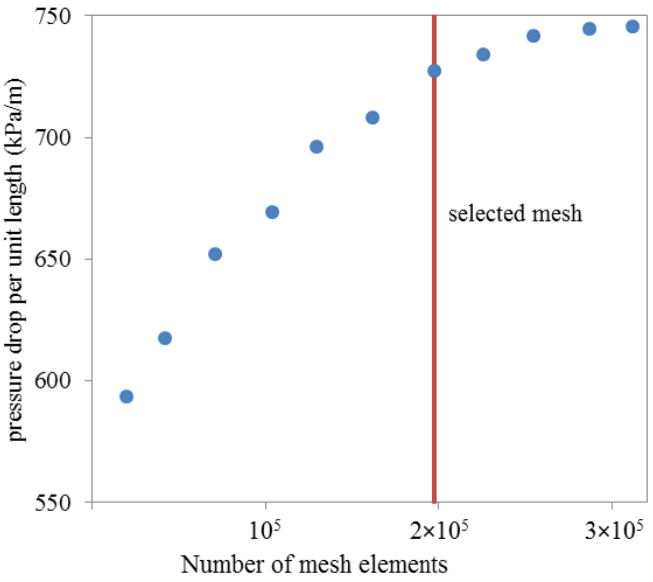

Figure 5.3. Mesh independency analysis for packed bed with SC arrangement.

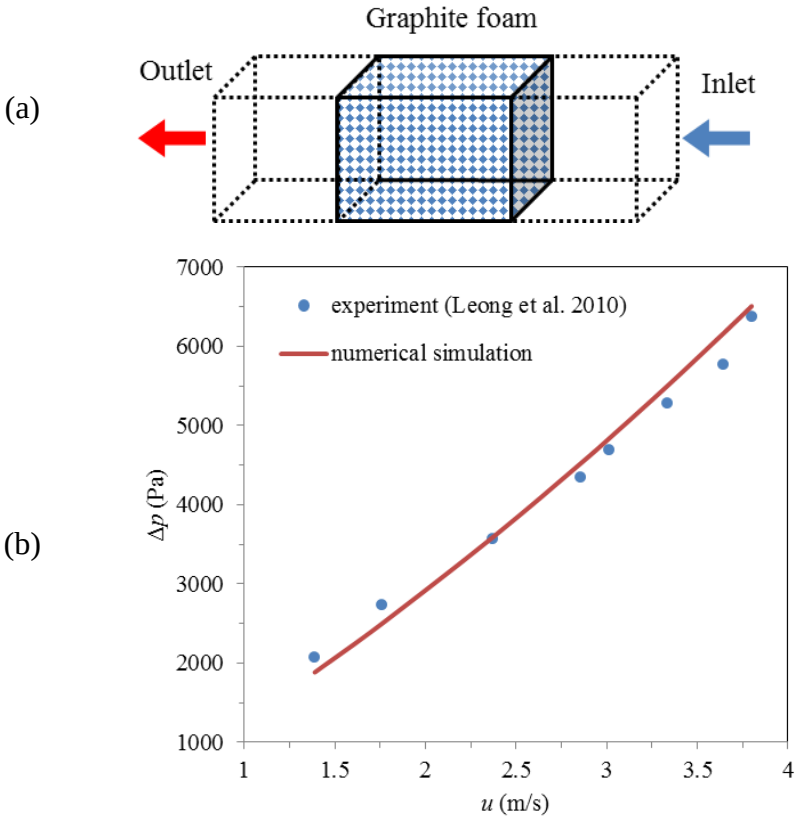

Figure 5.4. validation of the numerical method: (a) schematic diagram of the domain and (b) comparison of numerical and experimental results for pressure drop in terms of inlet velocity for graphite foam [125].

To validate the numerical method, the values of pressure drop calculated in this study for packed beds with solid particles are compared with those reported by Yang et al. [56] for different packing arrangements and Reynolds numbers. The results are presented in Table 5.2. There is a good agreement between the results showing the validity of the numerical method.

Table 5.2. Comparison of pressure drop for different packing arrangements.

Packing arrangement	Yang et al. [56]	Current simulation	Error (%)
	$\Delta p/\Delta x$ (Pa/m)	$\Delta p/\Delta x$ (Pa/m)	$\Delta p/\Delta x$ (Pa/m)
SC (Re=100)	8.32	8.63	3.7
SC (Re=5000)	301.42	308.63	2.4
BCC (Re=100)	39.89	41.07	2.9
BCC (Re=5000)	1057.77	1088.84	2.9
FCC (Re=100)	102.52	99.24	3.2
FCC (Re=5000)	2456.09	2531.06	3.1

Velocity field solution

Figure 5.5 illustrates the velocity fields for the SC unit cell for two different values of the particle Reynolds numbers Re_p and the ω-region permeability K_ω. With decreasing K_ω at fixed Re_p, the fraction of the fluid flowing through the ω-region decreases. For example, at Re_p=5, the fraction of the fluid flowing through the ω-region decreases from 13.9 to 3.16% for the permeability decreasing from K_ω=10^{-9} to 10^{-11} m^2, respectively. This effect is due to a higher pressure drop within the ω-region for lower K_ω. In addition, by decreasing the value of K_ω at fixed Re_p, stagnation zones are formed near the contact region between the spheres, resulting in vortex structures (see grey circles in Figure 5.5b and Figure 5.5d). Such vortex patterns were also observed in the study performed by Yang et al. [56] for packed bed of solid spherical particles. The pore-level velocity fields for BCC and FCC packing arrangements shown in Figure 5.1b and Figure 5.1c are also solved numerically, but they are not shown here for brevity.

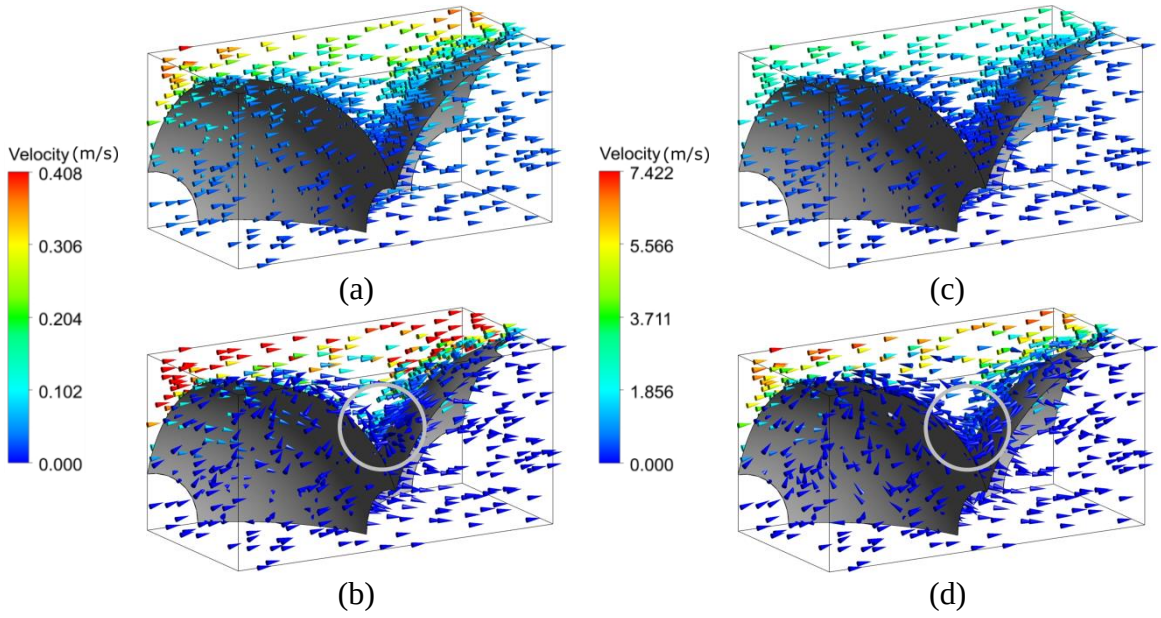

Figure 5.5. Pore-level velocity field for SC packing arrangement at (a) Re_p=5 and $K_\omega = 10^{-9}$ m^2, (b) Re_p=5 and $K_\omega = 10^{-11}$ m^2, (c) Re_p=50 and $K_\omega = 10^{-9}$ m^2, and (d) Re_p=50 and $K_\omega = 10^{-11}$ m^2.

5.1.3. Solution of the closure problems

The calculated velocity fields for three selected dual-scale porous structures are now used to solve the closure problems. ANSYS Fluent 17.1 is applied [209]. The closure problems have the form of advection–diffusion equations with integral source terms. Therefore, user defined scalars (UDSs) are defined in ANSYS Fluent for the transport equation of each closure variables. For instance, in *Closure problem I*, the steady-state boundary value problem with two variables, $\mathbf{b}_{\eta\eta}$ and $\mathbf{b}_{\eta\omega}$, are coupled through the inter-region flux terms, i.e. $\mathbf{c}_{\eta\eta}$ and $\mathbf{c}_{\omega\eta}$. The inter-region flux terms are computed via user defined functions (UDFs) applied to UDSs. This enables one to integrate the inter-region flux terms over the η–ω interface in Eqs. (4.68) and (4.69). Analogous procedures are applied to solve *Closure problems II* and *III*.

In the last row of the Table 5.1, the parameter $\left(k_s/k_f\right)_\omega$ has been defined which is the ratio of solid to fluid thermal conductivity in ω-region. This parameter is presented by k_r. As mentioned, the fluid flowing in the domain is air with a known value of thermal conductivity, which is assumed constant due to the assumption of reasonably small temperature range. Therefore, the thermal conductivity of the η-region is the same as that of the air, since η-region (the inter-particle region) is a homogenous region where only the fluid exists. Although the LTE assumption has been made within the ω-region, we need to set a value for

the thermal conductivity of the solid phase in ω-region in order to define the effective thermal conductivity of the ω-region, i.e. K_ω. Since only one working fluid has been considered in this study, the parameter k_r has been introduced to analyse the effect of ω-region thermal conductivity.

Figure 5.6 shows the fields of the closure variables $\left(b_{\eta\eta}\right)_z$ and $\left(b_{\eta\omega}\right)_z$, for example for SC packing arrangement, which are obtained using the solution of *Closure problem I*. Two different values for both parameters of K_ω and k_r are taken into account in the process of solving the closure problems in order to be able to investigate their effect on the results. It can be observed that at a given Re_p and K_ω, increasing the value of k_r leads to a more uniform distribution of closure variables within the ω-region. This observation is explained by the fact that for higher k_r, the ω-region effective thermal conductivity becomes greater in comparison with that of the η-region. Therefore, the closure variable can diffuse more uniformly in the ω-region (for instance, compare Figure 5.6a and Figure 5.6b). At a given value of Re_p and k_r, two observations can be made by decreasing the permeability of the ω-region. Firstly, the contour lines of the closure variable in the ω-region become more vertical (for instance, compare Figure 5.6e and Figure 5.6g). This is due to the fact that as the value of K_ω decreases, less fluid passes through the ω-region. Thus, the convective term becomes less dominant compared to the conductive term. Therefore, the closure variable transfers in the ω-region mostly due to diffusion. Secondly, when the value of K_ω is lower, the closure variable in the η-region is convected more to the downstream in the flow direction (for instance, compare Figure 5.6e and Figure 5.6g). Such an observation can be explained by looking at Figure 3 in which it was shown that when K_ω decreases, more fluid passes through the inter-particle region (η-region). This makes the convection term more dominant in the η-region. Another point that can be observed in Figure 4 is that at a given value of K_ω and k_r, increasing the value of Re_p from 5 to 50, significantly changes the contour pattern of the closure variables in both η- and ω-region (for instance, compare Figure 5.6a and Figure 5.6e). At Re_p=5, the contour pattern is almost symmetrical to the middle *xy*-plane. In contrast, at Re_p=50, the observed pattern is totally asymmetric. At higher values of Re_p, the

effect of convection becomes more significant compared to conduction, which causes the closure variables to be convected more in the flow direction. The closure problems are also solved for BCC and FCC packing arrangements with the conditions provided in Table 5.2. However, the solutions of the closure problems for BCC and FCC packing arrangements are not shown here for brevity.

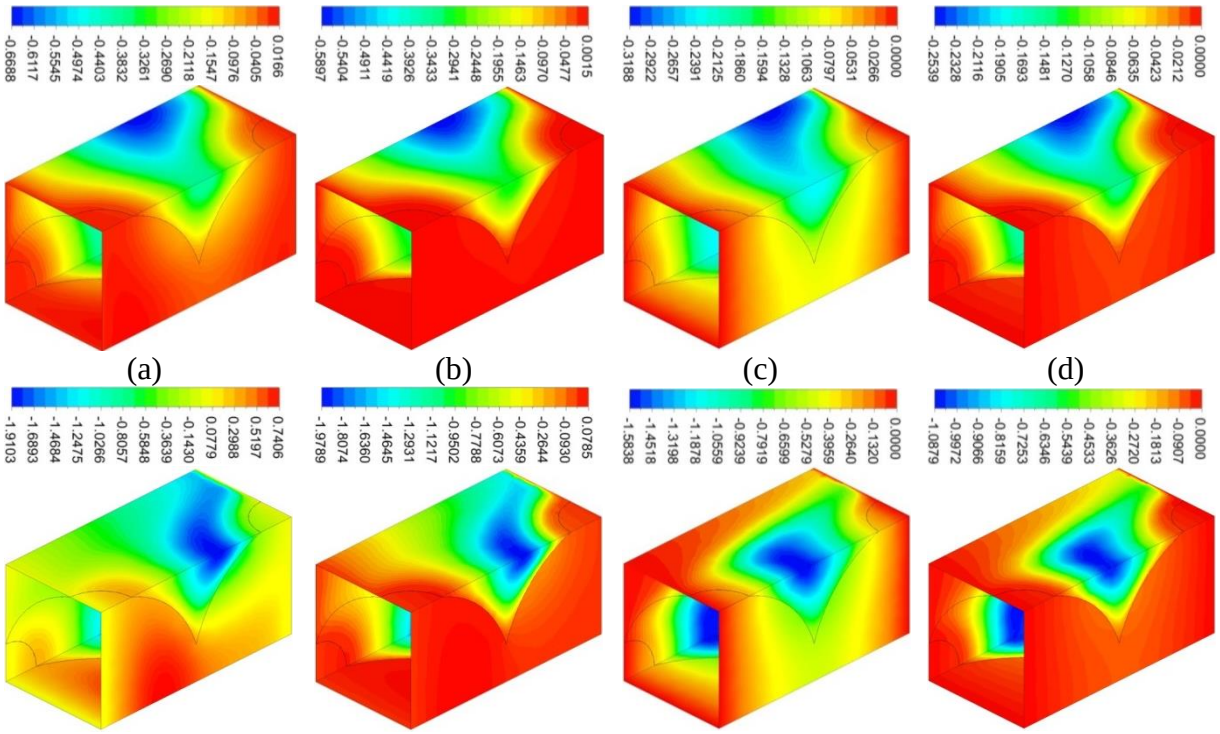

(a) Re_p=5, $K_\omega = 10^{-9}$ m^2 and k_r =10
(b) Re_p=5, $K_\omega = 10^{-9}$ m^2 and k_r =100
(c) Re_p=5, $K_\omega = 10^{-11}$ m^2 and k_r =10
(d) Re_p=5, $K_\omega = 10^{-11}$ m^2 and k_r =100
(e) Re_p=50, $K_\omega = 10^{-9}$ m^2 and k_r =10
(f) Re_p=50, $K_\omega = 10^{-9}$ m^2 and k_r =100
(g) Re_p=50, $K_\omega = 10^{-11}$ m^2 and k_r =10
(h) Re_p=50, $K_\omega = 10^{-11}$ m^2 and k_r =100

Figure 5.6. Closure variables $\left(b_{\eta\eta}\right)_z$ (m) and $\left(b_{\eta\omega}\right)_z$ (m) at different values of Re_p, K_ω and k_r for the SC packing arrangement.

Now that the closure problems are solved and the closure variables fields are obtained within the unit cell, the effective coefficients—which are functions of the closure variables—can be determined. Table 5.3 lists the effective coefficients of the dual-scale porous medium consisting of a packed bed of porous spherical particles with the SC packing arrangement calculated using the solution of the closure problems at different values of of Re_p, k_r and K_ω.

Table 5.3. Effective coefficients of the dual-scale porous medium consisting of a packed bed of porous spherical particles calculated from numerical solution of closure problems.

Coefficient	Re_p=5				Re_p=50			
	$K_\omega = 10^{-9}\,m^2$		$K_\omega = 10^{-11}\,m^2$		$K_\omega = 10^{-9}\,m^2$		$K_\omega = 10^{-11}\,m^2$	
	k_r =10	k_r =100	k_r =10	k_r =100	k_r =10	k_r =100	k_r =10	k_r =100
$\left(k_{\eta\eta}\right)_{zz}/\left(k_\eta\right)_{zz}$	0.707	0.339	0.707	0.339	0.707	0.339	0.707	0.339
$\left(k_{\omega\omega}\right)_{zz}/\left(k_\omega\right)_{zz}$	1.272	0.189	1.272	0.189	1.272	0.189	1.272	0.189
$\left(k_{\eta\omega}\right)_{zz}/\left(k_\eta\right)_{zz}$	0.031	0.087	0.037	0.119	0.032	0.097	0.061	0.190
$\left(k_{\omega\eta}\right)_{zz}/\left(k_\omega\right)_{zz}$	0.078	0.027	0.064	0.020	0.075	0.025	0.039	0.013
$\left(u_{\eta\eta}\right)_z/\left(k_\eta\right)_{zz}$ (1/m)	2.031 $\times 10^{-3}$	2.166 $\times 10^{-3}$	2.749 $\times 10^{-4}$	3.204 $\times 10^{-5}$	9.655 $\times 10^{-4}$	1.009 $\times 10^{-3}$	6.054 $\times 10^{-6}$	8.470 $\times 10^{-7}$
$\left(u_{\omega\omega}\right)_z/\left(k_\omega\right)_{zz}$ (1/m)	0.015	0.019	2.219 $\times 10^{-3}$	2.735 $\times 10^{-4}$	7.254 $\times 10^{-3}$	9.892 $\times 10^{-3}$	1.040 $\times 10^{-4}$	1.414 $\times 10^{-5}$
$\left(d_\eta\right)_z/\left(k_\eta\right)_{zz}$ (1/m)	1.404 $\times 10^{-6}$	1.403 $\times 10^{-6}$	5.131 $\times 10^{-6}$	4.439 $\times 10^{-5}$	3.245 $\times 10^{-6}$	3.234 $\times 10^{-6}$	6.037 $\times 10^{-6}$	5.092 $\times 10^{-5}$
$\left(d_\omega\right)_z/\left(k_\omega\right)_{zz}$ (m^{-1})	4.019 $\times 10^{-7}$	3.544 $\times 10^{-7}$	6.945 $\times 10^{-7}$	4.885 $\times 10^{-6}$	6.067 $\times 10^{-7}$	6.540 $\times 10^{-7}$	1.045 $\times 10^{-6}$	7.911 $\times 10^{-6}$
$\alpha/\left(k_\eta\right)_{zz}$ (m^{-2})	2.937 $\times 10^{-4}$	2.472 $\times 10^{-4}$	1.188 $\times 10^{-4}$	1.116 $\times 10^{-4}$	5.537 $\times 10^{-3}$	3.915 $\times 10^{-3}$	1.959 $\times 10^{-3}$	1.585 $\times 10^{-3}$

These effective coefficients can be applied in the up-scaled two-equation model of heat transfer for the given dual-scale porous structure. Using the effective coefficients makes it possible for the users intending to perform numerical simulation at level C to save computational resources instead of solving the energy equations at level B, Eqs. (4.5) to (4.8). For instance, the users intending to perform parametric study in a solar thermochemical reactor, they can employ the two-equation model at the reactor level along with the calculated effective coefficients for the reacting dual-scale porous medium [219–221].

5.2. Two-equation model verification

In this section, the fidelity of the two-equation model with the effective coefficients is investigated. For this purpose, pore-level simulations at level B are performed for the chosen packed beds of porous particles. The procedure of performing pore-level simulations for fluid flow at level B is similar to that of the Darcy-level simulations introduced in Chapter 3.

Traditional mass and momentum conservation equations, Eqs. (3.1) and (3.2), are solved for the inter-particle region (blue regions in Figure 5.7a). The volume-averaged equations for mass and momentum, Eqs. (3.3) and (3.4), are solved to model the fluid flow within the porous particles (yellow regions in Figure 5.7a). Note that only the Darcy term is considered in volume-averaged momentum equation. For heat transfer at level B, Eqs. (4.5)–(4.8) are solved.

A homogenised medium, shown in Figure 5.7b, is considered for the up-scaled volume-averaged model with the effective coefficients. For this case, the volume-averaged equations for mass and momentum, Eqs. (3.3) and (3.4), are solved to model the fluid flow in the whole homogenised dual-scale packed bed (yellow regions in Figure 5.7b). Only Darcy term is considered in volume-averaged momentum equation. The effective permeability of the homogenised medium is calculated using the results of the Darcy-level simulations, similar to the procedure performed in Section 3.4. For heat transfer in the homogenised medium, the two-equation volume-averaged model presented in Eqs. (4.93) and (4.100) are solved. For the effective coefficients defined in Eqs. (4.94)–(4.99) and Eqs. (4.101)–(4.106), the values listed Table 5.3 are considered.

Note that the inlet and outlet blocks are specified before and after the dual-scale porous blocks to minimise the boundary effects in the simulations. In the inlet and outlet blocks, the traditional mass and momentum and energy conservation equations are solved. Comparing the results of pore-level simulations for the SC, BCC and FCC packing arrangements with those of the two-equation model with effective coefficients enables us to demonstrate the capability of the up-scaled two-equation model to predict the heat transfer in dual-scale porous media.

Table 5.4 presents the parameters related to the cases of pore-level simulations at level B and up-scaled homogeneous two-equation model. Other parameters are exactly the same as the ones listed in Table 5.1.

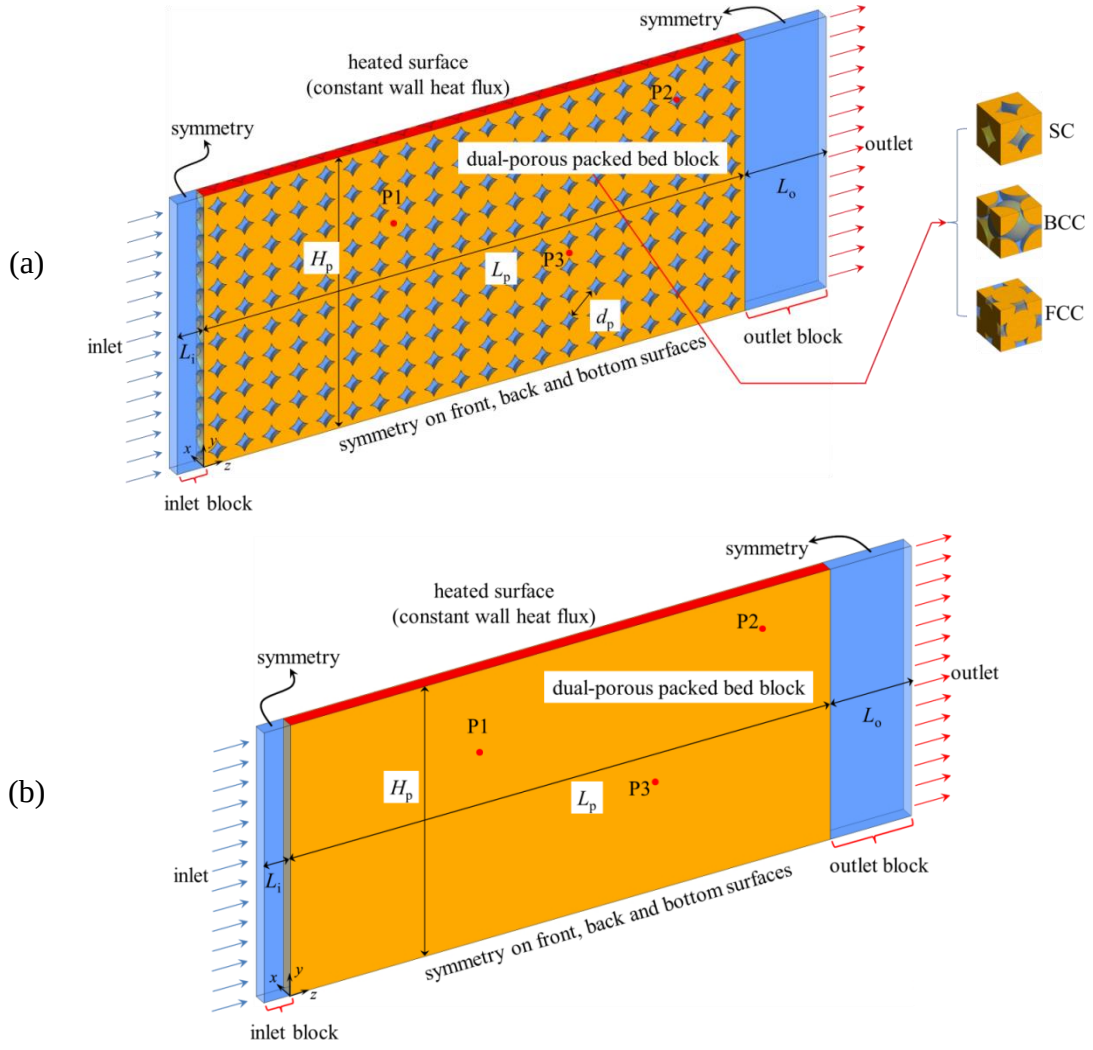

Figure 5.7. Computational domain for the solution of heat transfer for (a) pore-level at level B for different cases of SC, BCC and FCC packing arrangements and (b) up-scaled homogenised model at Level C.

Table 5.4. Parameters related to the cases of pore-level simulations at level B and up-scaled homogeneous two-equation model.

Parameter	SC	BCC	FCC
d_p	$2r_p$=1mm	$2r_p$=1mm	$2r_p$=1mm
l_{SC}	$=d_p$	–	–
l_{BCC}	–	$=2d_p/\sqrt{3}$	–
l_{FCC}	–	–	$=2d_p/\sqrt{2}$
L_i	$=d_p$	$=d_p$	$=d_p$
L_p	$=20l_{SC}$	$=20l_{BCC}$	$=20l_{FCC}$
L_o	$=3d_p$	$=3d_p$	$=3d_p$
H_p	$=10l_{SC}$	$=10l_{BCC}$	$=10l_{FCC}$

ANSYS Fluent 17.1 [209] is used to solve the conservation equations for both cases of pore-level simulations at level B and up-scaled two-equation models. Mesh independency analysis has also been performed for both cases to ensure the results are not changing with mesh refinement. The required number of mesh elements for the pore-level simulations for the cases of SC, BCC, and FCC packing arrangements are 5.19×10^6, 7.09×10^6 and 9.11×10^6, respectively. These values are, respectively, 133,350, 150,210, and 169,450 for the up-scaled homogenised cases. Figure 5.8 shows the meshing of the computational domain for performing pore-level simulations for SC packing arrangement depicted in Figure 5.7.

Figure 5.9 illustrates the velocity profile for a line located in the middle of the dual-porous packed bed with SC packing arrangement at Re_p=5, $K_\omega = 10^{-9}\,m^2$ for two cases of pore-level simulations at level B and homogenised model.

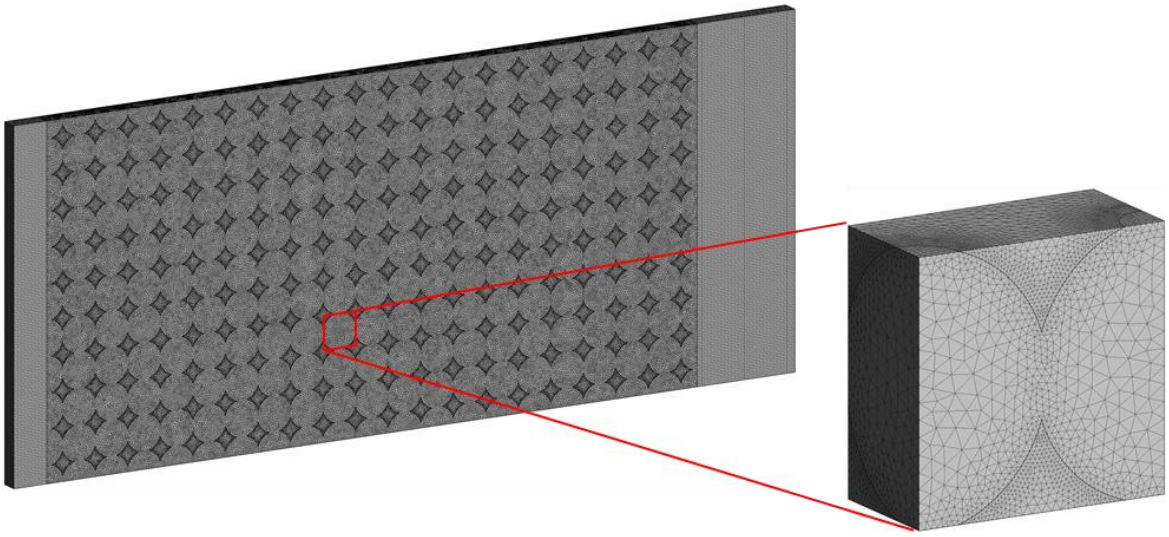

Figure 5.8. Meshing of the computational domain for performing pore-level simulations for the SC packing arrangement.

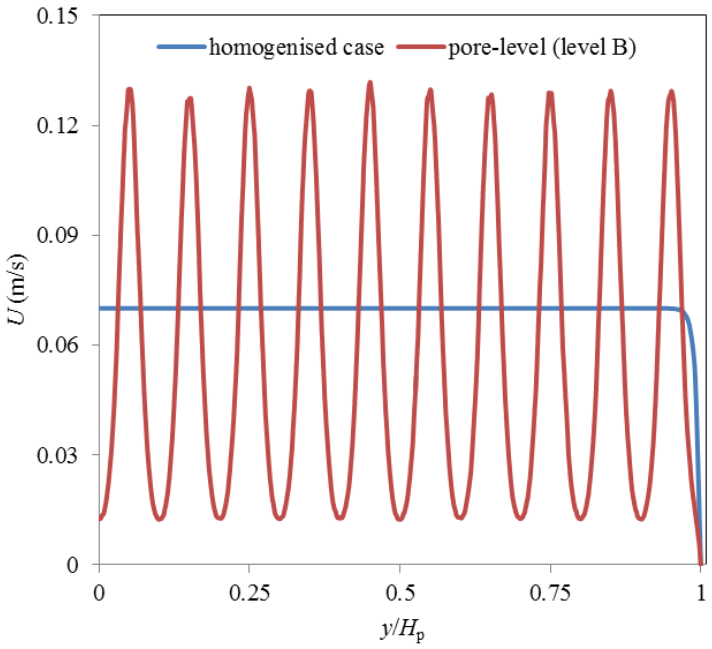

Figure 5.9. Velocity magnitude for a line located in the middle of the dual-porous packed bed with SC packing arrangement at Re_p=5, $K_\omega = 10^{-9}$ m^2 for two cases of pore-level at level B and homogenised case.

Figure 5.10 depicts the steady-state pore-level and up-scaled temperature fields for three cases. When comparing the temperature fields obtained using the results of pore-level simulations and up-scaled homogenised model, similar trends can be observed. This qualitatively shows the fidelity of the volume-averaged two-equation model with the effective coefficients in predicting the pore-level results. This fidelity has been obtained by using much less computational resources. Compare the number of mesh elements for pore-level simulations and up-scaled model. By comparing the results of up-scaled homogenised model to the pore-level simulations, the maximum point to point relative error is reported to be approximately 1.1%, mostly occurring at the vicinity of the wall with constant heat flux.

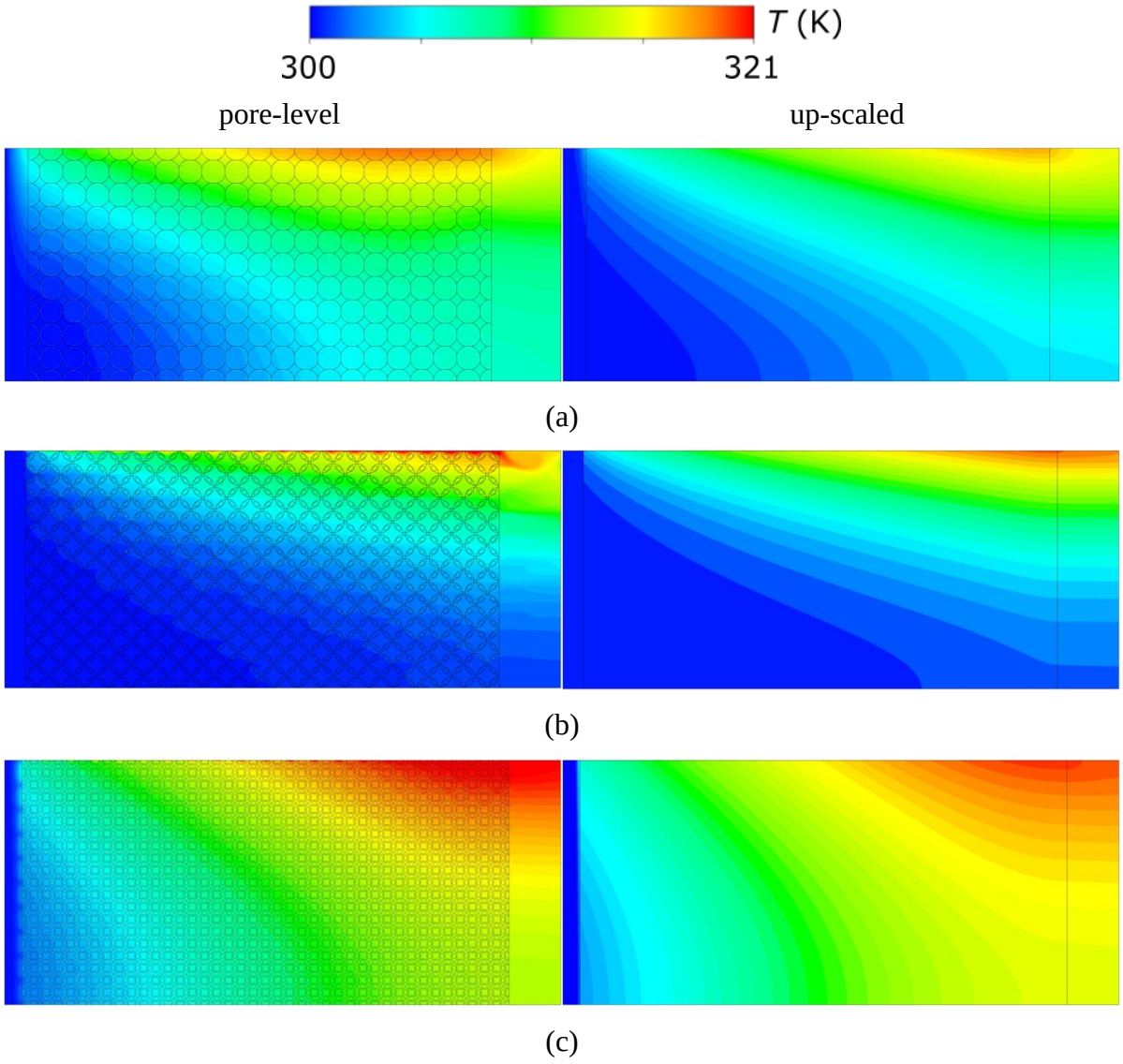

Figure 5.10. Steady-state pore-level and up-scaled temperature fields for (a) SC at Re_p=5, $K_\omega = 10^{-9}$ m^2, $k_r = 10$, q''_w=300 W/m^2, (b) BCC at Re_p=50, $K_\omega = 10^{-11}$ m^2, $k_r = 100$, q''_w=1800 W/m^2, and (c) FCC at Re_p=5, $K_\omega = 10^{-11}$ m^2, $k_r = 100$, q''_w=500 W/m^2.

Three control points P1, P2, and P3 are placed at selected locations of the domain showed in Figure 5.7. The temperature of the control points are calculated over time in order to quantitatively analyse the accuracy of the results of the homogenised model compared to those of the pore-level simulations at level B. For the case of SC packing arrangement, the coordinates of the control points P1, P2 and P3 are $\left(0, 7l_{SC}, 7l_{SC}\right)$, $\left(0.25l_{SC}, 8.5l_{SC}, 17.5l_{SC}\right)$, and $\left(0.5l_{SC}, 4l_{SC}, 13.5l_{SC}\right)$, respectively. The origin of the Cartesian coordinate system is in the leading edge of the dual-scale porous zone (see Figure 5.7).

Figure 5.11 shows the transient temperature calculated using the results of pore-level simulations and the up-scaled model for the case of SC at Re_p=5, K_ω=10^{-9}, k_r=10, q''_w=300 W/m^2 at the control points. Although the trend of temperature variation in terms of time is similar for all the control points, the transient temperature obtained using the up-scaled model seems to reach steady state faster than that of the pore-level simulations. For instance, for the control point P2, the temperature obtained using the homogenised model reaches steady-state after approximately 200 s. In contrast, the temperature obtained using the pore-level simulations at level B only starts to reach steady-state after 400 s. This can be attributed to the fact that for the up-scaled homogeneous model, we force the effective coefficients for the whole dual-porous domain. As shown in the procedure of calculating the effective coefficients in Section 5.1, the periodic unit cell with fully developed flow field was considered as the input for the closure problem solution (Section 5.1.2). However, in the pore-level simulations, it takes more time and length for the fluid flow and heat transfer to fully develop. Consequently, the temperature obtained using the results of pore-level simulations takes longer to reach steady state compared to the up-scaled model. However, the most important conclusion from comparing the results of pore-level simulations and the up-scaled model is that the two-equation homogenised model provides similar trends with appropriate fidelity and lower computational cost.

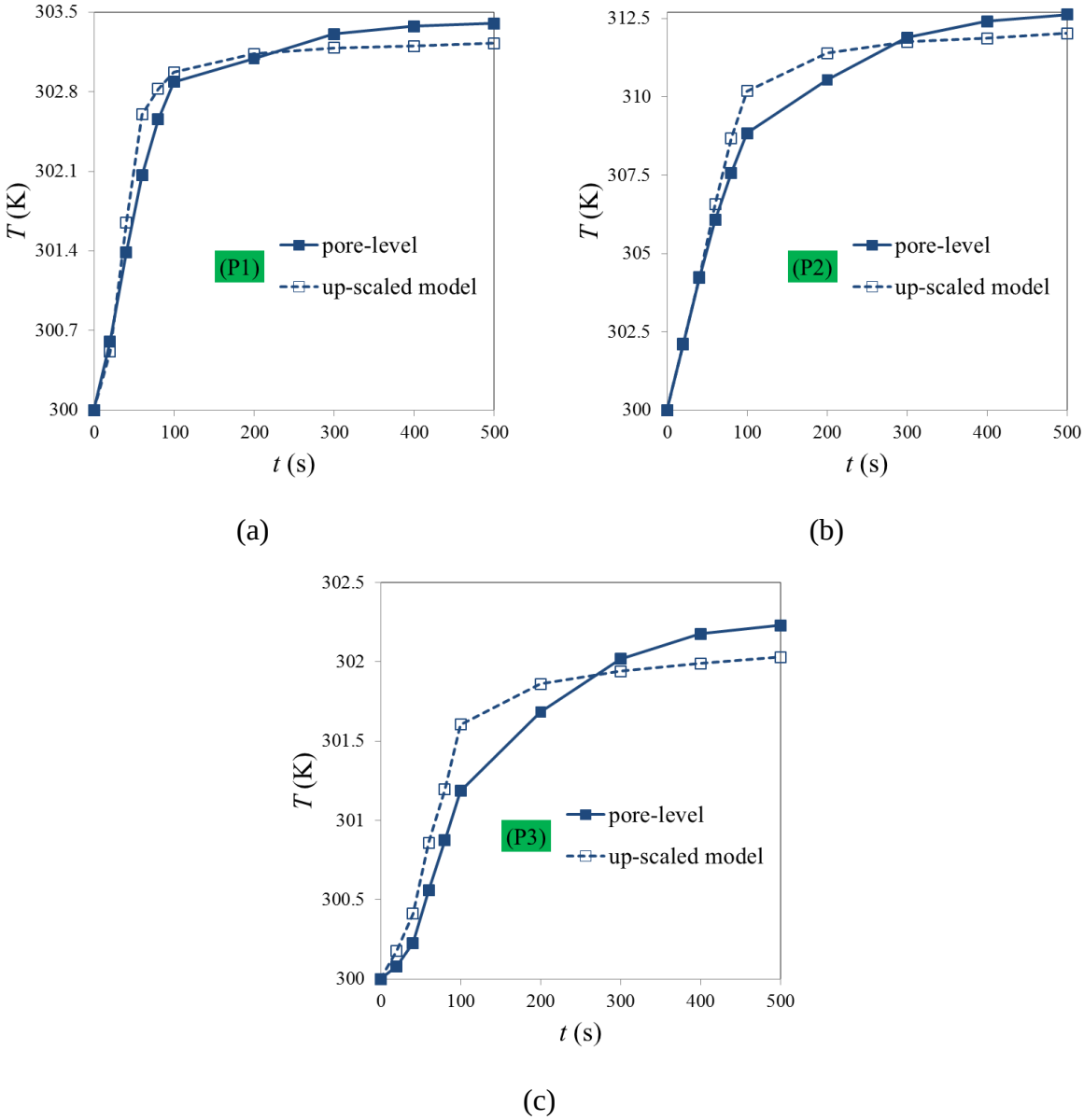

Figure 5.11. Transient temperature obtained using pore-level simulations and up-scaled model for the case of SC at Re_p=5, K_ω =10^{-9}, k_r =10, q''_w =300 W/m^2 at (a) P1, (b) P2, and (c) P3.

To obtain the effective coefficients to be used in the homogenised case, the closure problems are needed to be solved individually for each selected REV. This increases the computational time required for the homogenised case. Thus, the values of the effective coefficients are case-dependent. Every time the REV changes, the closure problems are solved for that specific case. However, the closure problems are only solved for a small selected REV (shown in Figure 5.1) requiring low computational time. Therefore, the overall computational time required for solving the closure problems, calculating the effective

properties, and solving the up-scaled homogenised case is still much lower than that of performing the pore-level simulations. For instance, the pore-level simulation for the case of SC arrangement with 5.19×10^6 mesh elements converged in less than 1.2 CPU hours. In contrast, the solution of the closure problems for the SC unit cell was completed in less than 0.18 CPU hours, and the up-scaled homogenised simulation converged in less than 0.22 CPU hours. Therefore, if the calculation time of the effective properties from the solution of the closure problems is neglected, the overall computational time is reduced by approximately 67%. Thus, for a given dual-scale porous media, the closure problems are solved only once, while the up-scaled problem will be solved many times in the application level. This enables performing parametric studies by saving a great deal of computational resources. This is the advantage of the up-scaled models compared to the pore-level simulations.

5.3. Summary

In this chapter, the closure problems introduced in Section 4.5 were numerically solved for a specific case of dual-scale porous structure. The medium consists of a packed bed of porous spherical particles. The effective coefficients appearing in the two-equation model of heat transfer in dual-porosity media are determined using the solutions of the closure problems. The procedure and results of analysing fluid flow in dual-scale porous media presented in Chapter 3 were used to model the velocity field in the dual-scale porous structure. Finally, "*numerical experiment*" was performed to qualitatively and quantitatively analyse the accuracy of the numerical results obtained using the up-scaled two-equation model in comparison with those of the pore-level simulations at level B. It was observed that the volume-averaged two-equation model with effective coefficients is well capable of estimating the results of pore-level simulations using much less computational resources.

For the theoretical analysis of heat transfer in dual-scale porous media, LTE was assumed within the micro-porous region and LTNE was assumed between the micro- and macro-pores. These assumptions were justified based on application of dual-scale porous media in high-temperature solar thermochemistry. However, in other applications such as hydrogeology and petroleum engineering, the characteristic length-scales of the two regions can be different but comparable. Therefore, the applicability of the proposed mathematical model needs to be considered in the specific applications. Addressing this problem is beyond the scope of this thesis.

Chapter 6
Conclusions and outlook

This dissertation was motivated by the need for understanding and analysing transport phenomena in dual-scale porous media appear and used in many applications such as hydrogeology, petroleum engineering, chemical reactors, and in particular, energy technologies in high-temperature thermochemistry. The main objective of this thesis is to theoretically formulate and numerically demonstrate the fluid flow and heat transfer phenomena in dual-scale porous media.

To investigate the flow process, numerical simulations, at the pore level and Darcy level, were performed on fluid flow in a dual-scale porous medium consisting of packed bed of porous spherical particles. The effect of changing the porosity of the porous particles was analysed on the flow behaviour in the dual-scale porous medium. It was observed that the size of the throats between the intra-particle pores considerably affects the fluid flow patterns at the inter- and intra-particle regions as well as the region between them. The permeability and Forchheimer coefficient of the packed bed featuring dual-scale porosity were calculated using the results of direct pore-level simulations and Darcy-level simulations. It was observed that the Darcy-level simulations overestimate the pressure drop in the dual-scale porous medium compared to the DPLS, particularly when the porosity of the porous particles is higher. However, Darcy-level simulations can provide acceptably accurate results using much less computational resources compared to DPLS. For Darcy-level simulations, the average of error in predicting effective flow properties compared to DPLS was approximately 7%.

To analyse the energy transport phenomena in dual-scale porous media, a theoretical approach was presented by applying volume-averaging method to the convective–conductive

energy conservation equation to derive the large-scale equations with effective coefficients. The closure problems were introduced along with the closure variables to establish the closed form of the two-equation model for heat transfer of dual-scale porous media. Such effort makes it possible for the users intending to perform numerical simulation at the application level, such as reactor level, to conveniently use the up-scaled equations along with the effective coefficients to model the heat transfer in the dual-scale porous media. The closure problems were numerically solved for a specific case of dual-scale porous structure consisting of a packed bed of porous spherical particles. The effective coefficients appearing in the two-equation model of heat transfer in dual-scale porous media were determined using the solution of the closure problems. The velocity field in the dual-scale porous structure was calculated using the solution of the fluid flow simulations in dual-scale porous medium. Finally, "numerical experiment" was performed to qualitatively and quantitatively analyse the accuracy of the numerical results obtained using the up-scaled model in comparison with those of the pore-level simulations. It was observed that the two-equation volume-averaged model with effective coefficients is well capable of estimating the pore-level results using much less computational resources.

Idealised ordered dual-scale porous structures were used to perform direct pore-level simulations. It has been shown in the literature that the heat and mass transfer phenomena in ordered porous structures may differ from the realistic and practical random porous structures. For instance, assuming models with ordered arrangement of particles in packed beds underestimate the hydraulic losses compared to randomly packed bed of particles [56, 126]. However, the REVs of realistic and practical dual-scale porous media (Figure 1.2) are much larger in size and more complex in geometry. Thus, considering the current computational resources, performing direct pore-level simulations of heat transfer and fluid flow in realistic dual-scale porous structures is a formidable task. This requires very large number of mesh elements and sophisticated meshing techniques, in particular for small-scale pores and the regions in the vicinity of the large- and small-scale pores. This issue can be considered in future studies.

Further investigations are required in future to fully understand and model different modes of transport phenomena in dual-scale porous media. Different modes of transport such as diffusion, dispersion, fluid flow, and different modes of heat transfer (conduction,

convection and radiation) can occur simultaneously in dual-scale porous media. Thus, in future studies, the effective coefficients are needed to be defined by considering other modes of transport. For instance, Klinkenberg's effect and Knudsen diffusion can occur for gas flow in dual-scale porous structures at high temperatures and low pressures. When the order of gas molecular mean free path is comparable to that of the average pore size, gas slippage and free-molecule flow becomes important. In such cases, the real permeability of a porous medium is different from the apparent permeability [222, 223]. This problem is beyond the scope of this thesis, and can be further investigated in future studies.

For the theoretical analysis of heat transfer in dual-scale porous media, LTE was assumed within the micro-porous region and LTNE was assumed between the micro- and macro-pores. These assumptions were justified based on conditions typical to dual-scale porous media in high-temperature solar thermochemical applications. In other applications, such as hydrogeology and petroleum engineering, the characteristic length-scales of the two regions can be different but comparable. Therefore, the applicability of the proposed mathematical model needs to be considered for specific applications.

Bibliography

[1] J. Bear, *Theory and Applications of Transport in Porous Media*, Springer, 2018.

[2] W. Lipiński, Future Fellowship: Thermal transport by design for fast and efficient solar thermochemical fuel production. *Australian Research Council*, FT140101213, 15 January 2015–14 January 2019.

[3] W.C. Chueh, C. Falter, M. Abbott, D. Scipio, P. Furler, S.M. Haile, A. Steinfeld, High-flux solar-driven thermochemical dissociation of CO_2 and H_2O using nonstoichiometric ceria, *Science*, 330 (2010) 1797–1801.

[4] P. Furler, D. Marxer, M. Takacs, A. Steinfeld, Solar thermochemical reactor technology for splitting CO_2, *AIP Conference Proceedings*, 2033 (2018) 130005.

[5] P. Furler, J. Scheffe, M. Gorbar, L. Moes, U. Vogt, A. Steinfeld, Solar thermochemical CO_2 splitting utilizing a reticulated porous ceria redox system, *Energy & Fuels*, 26 (2012) 7051–7059.

[6] P.G. Loutzenhiser, A. Meier, A. Steinfeld, Review of the two-step H_2O/CO_2-splitting solar thermochemical cycle based on Zn/Zno redox reactions, *Materials*, 3 (2010) 4922.

[7] A. Stamatiou, P.G. Loutzenhiser, A. Steinfeld, Syngas production from H_2O and CO_2 over Zn particles in a packed-bed reactor, *AIChE Journal*, 58 (2012) 625–631.

[8] A. Steinfeld, Solar thermochemical production of hydrogen—a review, *Solar Energy*, 78 (2005) 603–615.

[9] C. Agrafiotis, M. Roeb, C. Sattler, A review on solar thermal syngas production via redox pair-based water/carbon dioxide splitting thermochemical cycles, *Renewable and Sustainable Energy Reviews*, 42 (2015) 254–285.

[10] S. Abanades, P. Charvin, F. Lemont, G. Flamant, Novel two-step SnO_2/SnO water-splitting cycle for solar thermochemical production of hydrogen, *International Journal of Hydrogen Energy*, 33 (2008) 6021–6030.

[11] P. Furler, Solar thermochemical CO_2 and H_2O splitting via ceria redox reaction, *ETH* Zurich, 2014.

[12] N. Gokon, T. Mizuno, Y. Nakamuro, T. Kodama, Iron-containing yttria-stabilized zirconia system for two-step thermochemical water splitting, *Journal of Solar Energy Engineering*, 130 (2007) 011018–011018.

[13] S. Haussener, D. Hirsch, C. Perkins, A. Weimer, A. Lewandowski, A. Steinfeld, Modeling of a multitube high-temperature solar thermochemical reactor for hydrogen production, *Journal of Solar Energy Engineering*, 131 (2009) 024503–024503.

[14] K.-S. Kang, C.-H. Kim, W.-C. Cho, K.-K. Bae, S.-H. Kim, C.-S. Park, Novel two-step thermochemical cycle for hydrogen production from water using germanium oxide: KIER 4 thermochemical cycle, *International Journal of Hydrogen Energy*, 34 (2009) 4283–4290.

[15] T. Nakamura, Hydrogen production from water utilizing solar heat at high temperatures, *Solar Energy*, 19 (1977) 467–475.

[16] P. Furler, J.R. Scheffe, A. Steinfeld, Syngas production by simultaneous splitting of H_2O and CO_2 via ceria redox reactions in a high-temperature solar reactor, *Energy & Environmental Science*, 5 (2012) 6098–6103.

[17] P. Furler, A. Steinfeld, Heat transfer and fluid flow analysis of a 4 kW solar thermochemical reactor for ceria redox cycling, *Chemical Engineering Science*, 137 (2015) 373–383.

[18] P. Furler, J. Scheffe, D. Marxer, M. Gorbar, A. Bonk, U. Vogt, A. Steinfeld, Thermochemical CO_2 splitting via redox cycling of ceria reticulated foam structures with dual-scale porosities, *Physical Chemistry Chemical Physics*, 16 (2014) 10503–10511.

[19] S. Ackermann, J. Scheffe, J. Duss, A. Steinfeld, Morphological characterization and effective thermal conductivity of dual-scale reticulated porous structures, *Materials*, 7 (2014) 7173–7195.

[20] J. Petrasch, S. Haussener, W. Lipiński, Discrete vs. continuum-scale simulation of radiative transfer in semitransparent two-phase media, *Journal of Quantitative Spectroscopy and Radiative Transfer*, 112 (2011) 1450–1459.

[21] J. Petrasch, F. Meier, H. Friess, A. Steinfeld, Tomography based determination of permeability, Dupuit–Forchheimer coefficient, and interfacial heat transfer coefficient in reticulate porous ceramics, *International Journal of Heat and Fluid Flow*, 29 (2008) 315–326.

[22] J. Petrasch, B. Schrader, P. Wyss, A. Steinfeld, Tomography-based determination of the effective thermal conductivity of fluid-saturated reticulate porous ceramics, *Journal of Heat Transfer*, 130 (2008) 032602–032602.

[23] J. Petrasch, P. Wyss, R. Stämpfli, A. Steinfeld, Tomography-based multiscale analyses of the 3D geometrical morphology of reticulated porous ceramics, *Journal of the American Ceramic Society*, 91 (2008) 2659–2665.

[24] R.E. Hayes, S.T. Kolaczkowski, P.K.C. Li, S. Awdry, The palladium catalysed oxidation of methane: reaction kinetics and the effect of diffusion barriers, *Chemical Engineering Science*, 56 (2001) 4815–4835.

[25] C.S. Kong, D.-Y. Kim, H.-K. Lee, Y.-G. Shul, T.-H. Lee, Influence of pore-size distribution of diffusion layer on mass-transport problems of proton exchange membrane fuel cells, *Journal of Power Sources*, 108 (2002) 185–191.

[26] M.B. Rao, S. Sircar, Nanoporous carbon membranes for separation of gas mixtures by selective surface flow, *Journal of Membrane Science*, 85 (1993) 253–264.

[27] K. Zhang, J.D. Way, Optimizing the synthesis of composite polyvinylidene dichloride-based selective surface flow carbon membranes for gas separation, *Journal of Membrane Science*, 369 (2011) 243–249.

[28] D. Salama, A. Kantzas, Monitoring of diffusion of heavy oils with hydrocarbon solvents in the presence of sand, in *SPE International Thermal Operations and Heavy Oil Symposium*. 2005, Society of Petroleum Engineers: Calgary, Alberta, Canada.

[29] D.C. Gooddy, D.G. Kinniburgh, J.A. Barker, A rapid method for determining apparent diffusion coefficients in Chalk and other consolidated porous media, *Journal of Hydrology*, 343 (2007) 97–103.

[30] L. Cavé, T. Al, Y. Xiang, P. Vilks, A technique for estimating one-dimensional diffusion coefficients in low-permeability sedimentary rock using X-ray radiography: Comparison with through-diffusion measurements, *Journal of Contaminant Hydrology*, 103 (2009) 1–12.

[31] A.E. Scheidegger, General theory of dispersion in porous media, *Journal of Geophysical Research (1896–1977)*, 66 (1961) 3273–3278.

[32] R.A. Bernard, R.H. Wilhelm, Turbulent diffusion in fixed beds of packed solids, *Chemical Engineering Progress*, 46 (1950) 233–244.

[33] J.J. Carberry, R.H. Bretton, Axial dispersion of mass in flow through fixed beds, *AIChE Journal*, 4 (1958) 367–375.

[34] M. Auset, A.A. Keller, Pore-scale processes that control dispersion of colloids in saturated porous media, *Water Resources Research*, 40 (2004).

[35] H.P.G. Darcy. *Détermination des Lois d'Écoulement de l'Eau á travers le Sable*. 1856.

[36] J. Bear. *Dynamics of Fluids in Porous Media*. Courier Corporation, 1988.

[37] M. Kaviany, *Principles Of Heat Transfer In Porous Media*, Springer, 1991.

[38] P. Forchheimer, Wasserbewegung durch boden, *Zeitschrift des Vereins Deutscher Ingenieure*, 45 (1901) 1782–1788.

[39] H. Brinkman, A calculation of the viscous force exerted by a flowing fluid in a dense swarm of particles, *Applied Scientific Research*, 1 (1946) 27–34.

[40] T.S. Lundgren, Slow flow through stationary random beds and suspensions of spheres, *Journal of Fluid Mechanics*, 51 (2006) 273–299.

[41] R.S. Dhamrat, J.L. Ellzey, Numerical and experimental study of the conversion of methane to hydrogen in a porous media reactor, *Combustion and Flame*, 144 (2006) 698–709.

[42] P. Qian, J. Wang, Z. Wu, J. Yang, Q. Wang, Performance comparison of methane steam reforming in a randomly packed bed and a grille-sphere composite packed bed, *Energy Conversion and Management*, 193 (2019) 39–51.

[43] X.-H. Han, Q. Wang, Y.-G. Park, C. T'Joen, A. Sommers, A. Jacobi, A review of metal foam and metal matrix composites for heat exchangers and heat sinks, *Heat Transfer Engineering*, 33 (2012) 991–1009.

[44] J. Kim, T. Sibilli, M.Y. Ha, K. Kim, S.Y. Yoon, Compound porous media model for simulation of flat top U-tube compact heat exchanger, *International Journal of Heat and Mass Transfer*, 138 (2019) 1029–1041.

[45] G. Barreto, P. Canhoto, M. Collares-Pereira, Combined experimental and numerical determination of the asymmetry factor of scattering phase functions in porous volumetric solar receivers, *Solar Energy Materials and Solar Cells*, 206 (2020) 110327.

[46] S. Du, Z.-X. Tong, H.-H. Zhang, Y.-L. He, Tomography-based determination of Nusselt number correlation for the porous volumetric solar receiver with different geometrical parameters, *Renewable Energy*, 135 (2019) 711–718.

[47] J.C. Maxwell, *A Treatise on Electricity and Magnetism*, 3 ed., Cambridge University Press, Cambridge, 1954.

[48] C.T. Hsu, P. Cheng, K.W. Wong, Modified Zehner–Schlunder models for stagnant thermal conductivity of porous media, *International Journal of Heat and Mass Transfer*, 37 (1994) 2751–2759.

[49] K. Boomsma, D. Poulikakos, On the effective thermal conductivity of a three-dimensionally structured fluid-saturated metal foam, *International Journal of Heat and Mass Transfer*, 44 (2001) 827–836.

[50] M.A.A. Mendes, S. Ray, D. Trimis, A simple and efficient method for the evaluation of effective thermal conductivity of open-cell foam-like structures, *International Journal of Heat and Mass Transfer*, 66 (2013) 412–422.

[51] R. Singh, *Predictions of Effective Thermal Conductivity of Complex Materials.* In book: *Heat Transfer in Multi-Phase Materials*, A. Öchsner, G. Murch (eds), Vol 2, Springer, Berlin, Heidelberg, 2010.

[52] V.M. Eroshenko, L.A. Yaskin, Heat transfer in forced convection of fluid in porous sintered metals, *Journal of engineering physics*, 30 (1976) 1–8.

[53] A.G. Dixon, D.L. Cresswell, Theoretical prediction of effective heat transfer parameters in packed beds, *AIChE Journal*, 25 (1979) 663–676.

[54] A.R. Balakrishnan, D.C.T. Pei, Heat transfer in gas–solid packed bed systems. 3. Overall heat transfer rates in adiabatic beds, *Industrial & Engineering Chemistry Process Design and Development*, 18 (1979) 47–50.

[55] V.V. Calmidi, R.L. Mahajan, Forced convection in high porosity metal foams, *Journal of Heat Transfer*, 122 (2000) 557–565.

[56] J. Yang, Q. Wang, M. Zeng, A. Nakayama, Computational study of forced convective heat transfer in structured packed beds with spherical or ellipsoidal particles, *Chemical Engineering Science*, 65 (2010) 726–738.

[57] M.A. Mujeebu, M.Z. Abdullah, M.Z.A. Bakar, A.A. Mohamad, M.K. Abdullah, Applications of porous media combustion technology – A review, *Applied Energy*, 86 (2009) 1365–1375.

[58] S. Sobhani, J. Legg, D.F. Bartz, J.J. Kojima, C.T. Chang, J.D. Sullivan, J.P. Moder, M. Ihme, Experimental investigation of lean premixed pre-vaporized liquid-fuel combustion in porous media burners at elevated pressures up to 20 bar, *Combustion and Flame*, 212 (2020) 123–134.

[59] D.L. Damm, A.G. Fedorov, Radiation heat transfer in SOFC materials and components, *Journal of Power Sources*, 143 (2005) 158–165.

[60] W.A. Ge, C.Y. Zhao, B.X. Wang, Thermal radiation and conduction in functionally graded thermal barrier coatings. Part I: Experimental study on radiative properties, *International Journal of Heat and Mass Transfer*, 134 (2019) 101–113.

[61] L. Glicksman, M. Schuetz, M. Sinofsky, Radiation heat transfer in foam insulation, *International Journal of Heat and Mass Transfer*, 30 (1987) 187–197.

[62] D. Baillis, M. Arduini-Schuster, J.F. Sacadura, Identification of spectral radiative properties of polyurethane foam from hemispherical and bi-directional transmittance and reflectance measurements, *Journal of Quantitative Spectroscopy and Radiative Transfer*, 73 (2002) 297–306.

[63] J. Randrianalisoa, D. Baillis, L. Pilon, Improved inverse method for radiative characteristics of closed-cell absorbing porous media, *Journal of Thermophysics and Heat Transfer*, 20 (2006) 871–883.

[64] J.F. Sacadura, D. Baillis, Experimental characterization of thermal radiation properties of dispersed media, *International Journal of Thermal Sciences*, 41 (2002) 699–707.

[65] D. Baillis, J.-F. Sacadura, Thermal radiation properties of dispersed media: theoretical prediction and experimental characterization, *Journal of Quantitative Spectroscopy and Radiative Transfer*, 67 (2000) 327–363.

[66] M. Loretz, R. Coquard, D. Baillis, E. Maire, Metallic foams: Radiative properties/comparison between different models, *Journal of Quantitative Spectroscopy and Radiative Transfer*, 109 (2008) 16–27.

[67] E. Placido, M.C. Arduini-Schuster, J. Kuhn, Thermal properties predictive model for insulating foams, *Infrared Physics & Technology*, 46 (2005) 219–231.

[68] M.F. Modest, *Radiative Heat Transfer*, 3rd ed., Academic Press, San Diego, 2013.

[69] L.A. Dombrovsky, D. Baillis, *Thermal Radiation in Disperse Systems: an Engineering Approach*, 3rd ed., Begell House, New York, 2010.

[70] C. Argento, D. Bouvard, A ray tracing method for evaluating the radiative heat transfer in porous media, *International Journal of Heat and Mass Transfer*, 39 (1996) 3175–3180.

[71] A.K.C. Wu, S.H.K. Lee, Multiple-rays tracing technique for radiative exchange within packed beds, *Numerical Heat Transfer, Part B: Fundamentals*, 37 (2000) 469–487.

[72] A.F. Britto, C.S. Vivas, M.P. Almeida, I.C.d.C. Lima, A.T.d.C. Lima, Multiphase flow mobility impact on oil reservoir recovery: An open-source simulation, *AIP Advances*, 10 (2020) 035032.

[73] N. Chegenizadeh, A. Saeedi, X. Quan, Application of nanotechnology for enhancing oil recovery – A review, *Petroleum*, 2 (2016) 324–333.

[74] A. Jafari, M. Hasani, M. Hosseini, R. Gharibshahi, Application of CFD technique to simulate enhanced oil recovery processes: current status and future opportunities, *Petroleum Science*, 17 (2020) 434–456.

[75] J.H. Cushman, T.R. Ginn, Nonlocal dispersion in media with continuously evolving scales of heterogeneity, *Transport in Porous Media*, 13 (1993) 123–138.

[76] J.H. Cushman, B.X. Hu, F.W. Deng, Nonlocal reactive transport with physical and chemical heterogeneity: localization errors, *Water Resources Research*, 31 (1995) 2219–2237.

[77] A. Ding, D. Candela, Probing nonlocal tracer dispersion in flows through random porous media, *Physical Review E*, 54 (1996) 656–660.

[78] B.X. Hu, J.H. Cushman, F.-W. Deng, Nonlocal reactive transport with physical, chemical, and biological heterogeneity, *Advances in Water Resources*, 20 (1997) 293–308.

[79] B.X. Hu, F.-W. Deng, J.H. Cushman, Nonlocal reactive transport with physical and chemical heterogeneity: linear nonequilibrium sorption with random Kd, *Water Resources Research*, 31 (1995) 2239–2252.

[80] S.P.K. Sternberg, J.H. Cushman, R.A. Greenkorn, Laboratory observation of nonlocal dispersion, *Transport in Porous Media*, 23 (1996) 135–151.

[81] D.L. Koch, J.F. Brady, Anomalous diffusion in heterogeneous porous media, *The Physics of Fluids*, 31 (1988) 965–973.

[82] D.L. Koch, J.F. Brady, A non-local description of advection–diffusion with application to dispersion in porous media, *Journal of Fluid Mechanics*, 180 (2006) 387–403.

[83] H.P.A. Calis, J. Nijenhuis, B.C. Paikert, F.M. Dautzenberg, C.M. van den Bleek, CFD modelling and experimental validation of pressure drop and flow profile in a novel structured catalytic reactor packing, *Chemical Engineering Science*, 56 (2001) 1713–1720.

[84] J. Cushman, *Dynamics of Fluids in Hierarchical Porous Media*, Academic Press, 1990.

[85] J. Cushman, *The Physics of Fluids in Hierarchical Porous Media: Angstroms to Miles*, Springer Netherlands, 1997.

[86] D. Zhang, Impacts of local dispersion and first-order decay on solute transport in randomly heterogeneous porous media, *Transport in Porous Media*, 21 (1995) 123–144.

[87] D. Zhang, S.P. Neuman, Effect of local dispersion on solute transport in randomly heterogeneous media, *Water Resources Research*, 32 (1996) 2715–2723.

[88] G. Dagan, *Flow and Transport in Porous Formations*, Springer, Berlin, 1989.

[89] L.W. Gelhar, *Stochastic Subsurface Hydrology*, Prentice-Hall, Englewood Cliffs, 1993.

[90] S.P. Neuman, C.L. Winter, C.M. Newman, Stochastic theory of field-scale fickian dispersion in anisotropic porous media, *Water Resources Research*, 23 (1987) 453–466.

[91] L.W. Gelhar, A.L. Gutjahr, R.L. Naff, Stochastic analysis of macrodispersion in a stratified aquifer, *Water Resources Research*, 15 (1979) 1387–1397.

[92] J.E. Warren, F.F. Skiba, Macroscopic Dispersion, *Society of Petroleum Engineers Journal*, 4 (1964) 215–230.

[93] R.A. Freeze, A stochastic-conceptual analysis of one-dimensional groundwater flow in nonuniform homogeneous media, *Water Resources Research*, 11 (1975) 725–741.

[94] G. Dagan, Solute transport in heterogeneous porous formations, *Journal of Fluid Mechanics*, 145 (2006) 151–177.

[95] W.D. Graham, D.B. McLaughlin, A stochastic model of solute transport in groundwater: Application to the Borden, Ontario, Tracer Test, *Water Resources Research*, 27 (1991) 1345–1359.

[96] A.F.B. Tompson, L.W. Gelhar, Numerical simulation of solute transport in three-dimensional, randomly heterogeneous porous media, *Water Resources Research*, 26 (1990) 2541–2562.

[97] H. Zhan, On the Ergodicity hypothesis in heterogeneous formations, *Mathematical Geology*, 31 (1999) 113–134.

[98] W.-C. Yang, *Handbook of Fluidization and Fluid-Particle Systems*, 1st ed., CRC Press, Boca Raton, 2003.

[99] E. Sanchez-Palencia, *Non-homogeneous Media and Vibration Theory*, Springer-Verlag, New York, 1980.

[100] L. Tartar, C*onvergence of the Homogenization Process*, In Book: *Non-homogeneous Media and Vibration Theory*, E. Sanchez-Palencia (ed.), Springer-Verlag, New York, 1980.

[101] S.J. Hollister, N. Kikuchi, Homogenization theory and digital imaging: A basis for studying the mechanics and design principles of bone tissue, *Biotechnology and Bioengineering*, 43 (1994) 586–596.

[102] F. Ciucci, W. Lai, Derivation of micro/macro lithium battery models from homogenization, *Transport in Porous Media*, 88 (2011) 249–270.

[103] X. Zhang, D.M. Tartakovsky, Effective ion diffusion in charged nanoporous materials, *Journal of The Electrochemical Society*, 164 (2017) E53–E61.

[104] T.B. Anderson, R. Jackson, Fluid mechanical description of fluidized beds. Equations of motion, *Industrial & Engineering Chemistry Fundamentals*, 6 (1967) 527–539.

[105] J.C. Slattery, Flow of viscoelastic fluids through porous media, *AIChE Journal*, 13 (1967) 1066–1071.

[106] S. Whitaker, Diffusion and dispersion in porous media, *AIChE Journal*, 13 (1967) 420–427.

[107] S. Whitaker, The transport equations for multi-phase systems, *Chemical Engineering Science*, 28 (1973) 139–147.

[108] W.G. Gray, A derivation of the equations for multi-phase transport, *Chemical Engineering Science*, 30 (1975) 229–233.

[109] S. Whitaker, *The Method of Volume Averaging*, Kluwer Academic Publishers, Dordrecht, 1999.

[110] S. Whitaker, Flow in porous media I: A theoretical derivation of Darcy's law, *Transport in Porous Media*, 1 (1986) 3–25.

[111] S. Whitaker, The Forchheimer equation: A theoretical development, *Transport in Porous Media*, 25 (1996) 27–61.

[112] S. Whitaker, A.E. Cassano, *Concepts and Design of Chemical Reactors*, Gordon and Breach Science Publishers, 1986.

[113] M. Quintard, S. Whitaker, Local thermal equilibrium for transient heat conduction: theory and comparison with numerical experiments, *International Journal of Heat and Mass Transfer*, 38 (1995) 2779–2796.

[114] R.G. Carbonell, S. Whitaker, *Heat and Mass Transfer in Porous Media*, in Book: *Fundamentals of Transport Phenomena in Porous Media*, J. Bear, M.Y. Corapcioglu (Eds.), Springer Netherlands, Dordrecht, 1984, 121–198.

[115] W. Lipiński, D. Keene, S. Haussener, J. Petrasch, Continuum radiative heat transfer modeling in media consisting of optically distinct components in the limit of geometrical optics, *Journal of Quantitative Spectroscopy and Radiative Transfer*, 111 (2010) 2474–2480.

[116] W. Lipiński, J. Petrasch, S. Haussener, Application of the spatial averaging theorem to radiative heat transfer in two-phase media, *Journal of Quantitative Spectroscopy and Radiative Transfer*, 111 (2010) 253–258.

[117] V. Leroy, D. Bernard, Use of a downscaling procedure for macroscopic heat source modeling in porous media, *Transport in Porous Media*, 122 (2018) 459–486.

[118] T. Zaouter, D. Lasseux, M. Prat, Gas slip flow in a fracture: local Reynolds equation and upscaled macroscopic model, *Journal of Fluid Mechanics*, 837 (2017) 413–442.

[119] T. Qiu, Q. Wang, C. Yang, Upscaling multicomponent transport in porous media with a linear reversible heterogeneous reaction, *Chemical Engineering Science*, 171 (2017) 100–116.

[120] J.A. Ochoa-Tapia, S. Whitaker, Momentum transfer at the boundary between a porous medium and a homogeneous fluid—I. Theoretical development, *International Journal of Heat and Mass Transfer*, 38 (1995) 2635–2646.

[121] J.A. Ochoa-Tapia, S. Whitaker, Momentum transfer at the boundary between a porous medium and a homogeneous fluid—II. Comparison with experiment, *International Journal of Heat and Mass Transfer*, 38 (1995) 2647–2655.

[122] J.A. Ochoa-Tapia, S. Whitaker, Heat transfer at the boundary between a porous medium and a homogeneous fluid, *International Journal of Heat and Mass Transfer*, 40 (1997) 2691–2707.

[123] B. Alazmi, K. Vafai, Analysis of fluid flow and heat transfer interfacial conditions between a porous medium and a fluid layer, *International Journal of Heat and Mass Transfer*, 44 (2001) 1735–1749.

[124] A.G. Straatman, N.C. Gallego, Q. Yu, L. Betchen, B.E. Thompson, Forced convection heat transfer and hydraulic losses in graphitic foam, *Journal of Heat Transfer*, 129 (2006) 1237–1245.

[125] K.C. Leong, H.Y. Li, L.W. Jin, J.C. Chai, Numerical and experimental study of forced convection in graphite foams of different configurations, *Applied Thermal Engineering*, 30 (2010) 520–532.

[126] J. Yang, J. Wang, S. Bu, M. Zeng, Q. Wang, A. Nakayama, Experimental analysis of forced convective heat transfer in novel structured packed beds of particles, *Chemical Engineering Science*, 71 (2012) 126–137.

[127] S. Ergun, Fluid flow through packed columns, *Chemical Engineering Progress*, (1952) 89–94.

[128] N. Wakao, Kaguei, S., *Heat and Mass Transfer in Packed Beds*, McGraw-Hill, New York, 1982.

[129] J.K. Arthur, D.W. Ruth, M.F. Tachie, PIV measurements of flow through a model porous medium with varying boundary conditions, *Journal of Fluid Mechanics*, 629 (2009) 343–374.

[130] A.Y.L. Huang, M.Y.F. Huang, H. Capart, R.-H. Chen, Optical measurements of pore geometry and fluid velocity in a bed of irregularly packed spheres, *Experiments in Fluids*, 45 (2008) 309–321.

[131] A. Lachhab, Y.-K. Zhang, M.V.I. Muste, Particle tracking experiments in match-index-refraction porous media, *Groundwater*, 46 (2008) 865–872.

[132] M. Shams, Study of flow at the interface of a porous medium using particle image velocimetry Ph.D., *University of Toronto*, 1999.

[133] A. Raoof, S.M. Hassanizadeh, Upscaling transport of adsorbing solutes in porous media, *Journal of Porous Media*, 13 (2010) 395–408.

[134] I. Fatt, The network model of porous media I–III, *Petroleum Transactions AIME*, 207 (1956) 144–181.

[135] L. Tomutsa, D. Silin, Nanoscale pore imaging and pore scale fluid flow modelling in chalk, *Lawrence Berkeley National Laboratory*, 56266 (2004) 257–261.

[136] J.T. Fredrich, B. Menéndez, T.-F. Wong, Imaging the pore structure of geomaterials, *Science*, 268 (1995) 276–279.

[137] B. Matsumoto, I.L. Hale, *Preparation of Retinas for Studying Photoreceptors with Confocal Microscopy*, in Book: *Methods in Neurosciences*, P.A. Hargrave (Ed.), Academic Press, 1993, pp. 54–71.

[138] J. Coenen, E. Tchouparova, X. Jing, Measurement parameters and resolution aspects of micro X-ray tomography for advanced core analysis, *In Proceedings of International Symposium of the Society of Core Analysts, Abu Dhabi*, (2004).

[139] S. Schlüter, A. Sheppard, K. Brown, D. Wildenschild, Image processing of multiphase images obtained via X-ray microtomography: A review, *Water Resources Research*, 50 (2014) 3615–3639.

[140] A. Akolkar, J. Petrasch, Tomography based pore-level optimization of radiative transfer in porous media, *International Journal of Heat and Mass Transfer*, 54 (2011) 4775–4783.

[141] A. Akolkar, J. Petrasch, Tomography-based characterization and optimization of fluid flow through porous media, *Transport in Porous Media*, 95 (2012) 535–550.

[142] S. Haussener, P. Coray, W. Lipiński, P. Wyss, A. Steinfeld, Tomography-based heat and mass transfer characterization of reticulate porous ceramics for high-temperature processing, *Journal of Heat Transfer*, 132 (2009) 023305–023305.

[143] S. Haussener, I. Jerjen, P. Wyss, A. Steinfeld, Tomography-based determination of effective transport properties for reacting porous media, *Journal of Heat Transfer*, 134 (2011) 012601.

[144] S. Haussener, W. Lipiński, J. Petrasch, P. Wyss, A. Steinfeld, Tomographic characterization of a semitransparent-particle packed bed and determination of its thermal radiative properties, *Journal of Heat Transfer*, 131 (2009) 072701.

[145] J. Petrasch, P. Wyss, A. Steinfeld, Tomography-based Monte–Carlo determination of radiative properties of reticulate porous ceramics, *Journal of Quantitative Spectroscopy and Radiative Transfer*, 105 (2007) 180–197.

[146] S. Suter, A. Steinfeld, S. Haussener, Pore-level engineering of macroporous media for increased performance of solar-driven thermochemical fuel processing, *International Journal of Heat and Mass Transfer*, 78 (2014) 688–698.

[147] T. Atmakidis, E.Y. Kenig, CFD-based analysis of the wall effect on the pressure drop in packed beds with moderate tube/particle diameter ratios in the laminar flow regime, *Chemical Engineering Journal*, 155 (2009) 404–410.

[148] H. Bai, J. Theuerkauf, P.A. Gillis, P.M. Witt, A coupled DEM and CFD simulation of flow field and pressure drop in fixed bed reactor with randomly packed catalyst particles, *Industrial & Engineering Chemistry Research*, 48 (2009) 4060–4074.

[149] G. Boccardo, F. Augier, Y. Haroun, D. Ferré, D.L. Marchisio, Validation of a novel open-source work-flow for the simulation of packed-bed reactors, *Chemical Engineering Journal*, 279 (2015) 809–820.

[150] S. Das, N.G. Deen, J.A.M. Kuipers, A DNS study of flow and heat transfer through slender fixed-bed reactors randomly packed with spherical particles, *Chemical Engineering Science*, 160 (2017) 1–19.

[151] A.G. Dixon, G. Walls, H. Stanness, M. Nijemeisland, E.H. Stitt, Experimental validation of high Reynolds number CFD simulations of heat transfer in a pilot-scale fixed bed tube, *Chemical Engineering Journal*, 200-202 (2012) 344–356.

[152] N.J. Dyck, A.G. Straatman, A new approach to digital generation of spherical void phase porous media microstructures, *International Journal of Heat and Mass Transfer*, 81 (2015) 470–477.

[153] T. Eppinger, K. Seidler, M. Kraume, DEM-CFD simulations of fixed bed reactors with small tube to particle diameter ratios, *Chemical Engineering Journal*, 166 (2011) 324–331.

[154] N. Riefler, M. Heiland, N. Räbiger, U. Fritsching, Pressure loss and wall shear stress in flow through confined sphere packings, *Chemical Engineering Science*, 69 (2012) 129–137.

[155] M.V. Tabib, S.T. Johansen, S. Amini, A 3D CFD–DEM methodology for simulating industrial scale packed bed chemical looping combustion reactors, *Industrial & Engineering Chemistry Research*, 52 (2013) 12041–12058.

[156] J. Vu, A.G. Straatman, Comparison of pore-level and volume-averaged computations in highly conductive spherical-void-phase porous materials, *Transport in Porous Media*, 124 (2018) 509–531.

[157] S. Das, N.G. Deen, J.A.M. Kuipers, Direct numerical simulation for flow and heat transfer through random open-cell solid foams: Development of an IBM based CFD model, *Catalysis Today*, 273 (2016) 140–150.

[158] B. Dietrich, Pressure drop correlation for ceramic and metal sponges, *Chemical Engineering Science*, 74 (2012) 192–199.

[159] K. Alam, M.S. Anghelescu, A. Bradu, *Computational Model of Porous Media Using True 3-D Images*, in Book: *Heat Transfer in Multi-Phase Materials*, A. Öchsner, G.E. Murch (Eds.), Springer Berlin Heidelberg, Berlin, Heidelberg, 2011, 347–377.

[160] S.A.M. Karimian, A.G. Straatman, Numerical modeling of multidirectional flow and heat transfer in graphitic foams, *Journal of Heat Transfer*, 131 (2009).

[161] K.C. Leong, H.Y. Li, Theoretical study of the effective thermal conductivity of graphite foam based on a unit cell model, *International Journal of Heat and Mass Transfer*, 54 (2011) 5491–5496.

[162] Q. Yu, B.E. Thompson, A.G. Straatman, A unit cube-based model for heat transfer and fluid flow in porous carbon foam, *Journal of Heat Transfer*, 128 (2005) 352–360.

[163] S. Krishnan, J.Y. Murthy, S.V. Garimella, Direct simulation of transport in open-cell metal foam, *Journal of Heat Transfer*, 128 (2006) 793–799.

[164] P. Kumar, F. Topin, Micro-structural impact of different strut shapes and porosity on hydraulic properties of Kelvin-like metal foams, *Transport in Porous Media*, 105 (2014) 57–81.

[165] M. Sahraoui, M. Kaviany, Slip and no-slip velocity boundary conditions at interface of porous, plain media, *International Journal of Heat and Mass Transfer*, 35 (1992) 927–943.

[166] M. Sahraoui, M. Kaviany, Slip and no-slip temperature boundary conditions at interface of porous, plain media: conduction, *International Journal of Heat and Mass Transfer*, 36 (1993) 1019–1033.

[167] M. Sahraoui, M. Kaviany, Slip and no-slip temperature boundary conditions at the interface of porous, plain media: Convection, *International Journal of Heat and Mass Transfer*, 37 (1994) 1029–1044.

[168] O.A. Plumb, S. Whitaker, Dispersion in heterogeneous porous media: 1. Local volume averaging and large-scale averaging, *Water Resources Research*, 24 (1988) 913–926.

[169] O.A. Plumb, S. Whitaker, Dispersion in heterogeneous porous media: 2. Predictions for stratified and two-dimensional spatially periodic systems, *Water Resources Research*, 24 (1988) 927–938.

[170] O.A. Plumb, S. Whitaker, *Diffusion, Adsorption and Dispersion in Porous Media: Small-scale Averaging and Local Volume Averaging,* In Book: *Dynamics of Fluids in Hierarchical Porous Media*, J. H. Cushman (ed.), Academic Press, 1990, 97–149.

[171] O.A. Plumb, S. Whitaker, *Diffusion, Adsorption and Dispersion in Heterogeneous Porous Media: The Method of Large-scale Averaging,* In Book: *Dynamics of Fluids in Hierarchical Porous Media,* J. H. Cushman (ed.), Academic Press, 1990, 149–176.

[172] M. Quintard, S. Whitaker, Two-phase flow in heterogeneous porous media: The method of large-scale averaging, *Transport in Porous Media*, 3 (1988) 357–413.

[173] M. Quintard, S. Whitaker, Transport in chemically and mechanically heterogeneous porous media IV: large-scale mass equilibrium for solute transport with adsorption, *Advances in Water Resources*, 22 (1998) 33–57.

[174] X. Yan, Q. Wang, H.H. Bau, Dispersion in retentive pillar array columns, *Journal of Chromatography A*, 1217 (2010) 1332–1342.

[175] X. Yan, Q. Wang, N. Li, Predictive model of solute transport with reversible adsorption in spatially periodic hierarchical porous media, *Journal of Chromatography A*, 1407 (2015) 69–75.

[176] R.S. Jadhav, K.M. Pillai, Numerical study of heat transfer during unsaturated flow in dual-scale porous media, *Numerical Heat Transfer, Part A: Applications*, 43 (2003) 385–407.

[177] M.S. Munagavalasa, K.M. Pillai, An estimation of effective thermal conductivity of a fibrous dual-scale porous medium during unsaturated flow, *International Journal of Heat and Mass Transfer*, 49 (2006) 317–328.

[178] S. Sabet, M. Mobedi, M. Barisik, A. Nakayama, Numerical determination of interfacial heat transfer coefficient for an aligned dual scale porous medium, *International Journal of Numerical Methods for Heat & Fluid Flow*, 28 (2018) 2716–2733.

[179] H. Tan, K.M. Pillai, Fast liquid composite molding simulation of unsaturated flow in dual-scale fiber mats using the imbibition characteristics of a fabric-based unit cell, *Polymer Composites*, 31 (2010) 1790–1807.

[180] H. Tan, K.M. Pillai, Multiscale modeling of unsaturated flow of dual-scale fiber preform in liquid composite molding II: Non-isothermal flows, *Composites Part A: Applied Science and Manufacturing*, 43 (2012) 14–28.

[181] H. Tan, K.M. Pillai, Multiscale modeling of unsaturated flow in dual-scale fiber preforms of liquid composite molding III: reactive flows, *Composites Part A: Applied Science and Manufacturing*, 43 (2012) 29–44.

[182] A.B. Donald A. Nield, *Convection in Porous Media*, Springer, Cham, 2013.

[183] Y. Mahmoudi, K. Hooman, K. Vafai, *Convective Heat Transfer in Porous Media*, 1st ed., CRC Press, Boca Raton, 2019.

[184] D.A. Nield, A.V. Kuznetsov, Forced convection in a bi-disperse porous medium channel: a conjugate problem, *International Journal of Heat and Mass Transfer*, 47 (2004) 5375–5380.

[185] D.A. Nield, A.V. Kuznetsov, A two-velocity two-temperature model for a bi-dispersed porous medium: Forced convection in a channel, *Transport in Porous Media*, 59 (2005) 325–339.

[186] D.A. Nield, A.V. Kuznetsov, The onset of convection in a bidisperse porous medium, *International Journal of Heat and Mass Transfer*, 49 (2006) 3068–3074.

[187] D.A. Nield, A.V. Kuznetsov, Natural convection about a vertical plate embedded in a bidisperse porous medium, *International Journal of Heat and Mass Transfer*, 51 (2008) 1658–1664.

[188] M. Kumari, I. Pop, Mixed convection boundary layer flow past a horizontal circular cylinder embedded in a bidisperse porous medium, *Transport in Porous Media*, 77 (2009) 287–303.

[189] K. Wang, P. Li, Forced convection in bidisperse porous media incorporating viscous dissipation, *Applied Thermal Engineering*, 140 (2018) 86–94.

[190] A. Narasimhan, B.V.K. Reddy, Laminar forced convection in a heat generating bi-disperse porous medium channel, *International Journal of Heat and Mass Transfer*, 54 (2011) 636–644.

[191] A. Narasimhan, B.V.K. Reddy, P. Dutta, Thermal management using the bi-disperse porous medium approach, *International Journal of Heat and Mass Transfer*, 55 (2012) 538–546.

[192] A. Narasimhan, B.V.K. Reddy, Natural convection inside a bidisperse porous medium enclosure, *Journal of Heat Transfer*, 132 (2009).

[193] R. Bader, W. Lipiński, *Solar Thermal Processing*, in Book: *Advances in Concentrating Solar Thermal Research and Technology*, M.J. Blanco, L.R. Santigosa (Eds.), Woodhead Publishing, 2017, 403–459.

[194] W. Lipiński, J.H. Davidson, S. Haussener, J.F. Klausner, A.M. Mehdizadeh, J. Petrasch, A. Steinfeld, L. Venstrom, Review of heat transfer research for solar thermochemical applications, *Journal of Thermal Science and Engineering Applications*, 5 (2013) 021005.

[195] V.M. Wheeler, R. Bader, P.B. Kreider, M. Hangi, S. Haussener, W. Lipiński, Modelling of solar thermochemical reaction systems, *Solar Energy*, 156 (2017) 149–168.

[196] ANSYS, *ANSYS DesignModeler User Guide*, ANSYS Incorporation, Canonsburg, 2012.

[197] S. Cai, D. Zhang, L. Zhang, L. Huang, H. Li, R. Gao, L. Shi, J. Zhang, Comparative study of 3D ordered macroporous $Ce_{0.75}Zr_{0.2}M_{0.05}O_{2-\delta}$ (M = Fe, Cu, Mn, Co) for selective catalytic reduction of NO with NH_3, *Catalysis Science & Technology*, 4 (2014) 93–101.

[198] J. Xiong, Q. Wu, X. Mei, J. Liu, Y. Wei, Z. Zhao, D. Wu, J. Li, Fabrication of spinel-type $Pd_xCo_{3-x}O_4$ binary active sites on 3D ordered meso-macroporous Ce-Zr-O_2 with enhanced activity for catalytic soot oxidation, *ACS Catalysis*, 8 (2018) 7915–7930.

[199] K. Ganesan, J. Randrianalisoa, W. Lipiński, Effect of morphology on spectral radiative properties of three-dimensionally ordered macroporous ceria packed bed, *Journal of Heat Transfer*, 135 (2013) 122701–122701.

[200] S.G. Rudisill, L.J. Venstrom, N.D. Petkovich, T. Quan, N. Hein, D.B. Boman, J.H. Davidson, A. Stein, Enhanced oxidation kinetics in thermochemical cycling of CeO_2 through templated porosity, *The Journal of Physical Chemistry C*, 117 (2013) 1692–1700.

[201] L.J. Venstrom, N. Petkovich, S. Rudisill, A. Stein, J.H. Davidson, The effects of morphology on the oxidation of ceria by water and carbon dioxide, *Journal of Solar Energy Engineering*, 134 (2011) 011005–011005.

[202] C.M. Doherty, R.A. Caruso, B.M. Smarsly, C.J. Drummond, Colloidal crystal templating to produce hierarchically porous $LiFePO_4$ electrode materials for high power lithium ion batteries, *Chemistry of Materials*, 21 (2009) 2895–2903.

[203] S. Wang, Z. Zhang, S. Fang, L. Yang, C. Yang, S.-i. Hirano, Synthesis and electrochemical properties of ordered macroporous $Li_3V_2(PO_4)_3$ cathode materials for lithium ion batteries, *Electrochimica Acta*, 111 (2013) 685–690.

[204] X. Tao, R. Long, D. Wu, Y. Hu, G. Qiu, Z. Qi, B. Li, R. Jiang, Y. Xiong, Anchoring positively charged Pd single atoms in ordered porous ceria to boost catalytic activity and stability in Suzuki coupling reactions, *Small*, 16 (2020) 2001782.

[205] G. Zhang, Z. Zhao, J. Liu, G. Jiang, A. Duan, J. Zheng, S. Chen, R. Zhou, Three dimensionally ordered macroporous $Ce_{1-x}Zr_xO_2$ solid solutions for diesel soot combustion, *Chemical Communications*, 46 (2010) 457–459.

[206] S.V. Patankar, C.H. Liu, E.M. Sparrow, Fully developed flow and heat transfer in ducts having streamwise-periodic variations of cross-sectional area, *Journal of Heat Transfer*, 99 (1977) 180–186.

[207] M.L. Martins-Costa, R.M. Saldanha de Gama, A local model for the heat transfer process in two distinct flow regions, *International Journal of Heat and Fluid Flow*, 15 (1994) 477–485.

[208] K. Vafai, S.J. Kim, On the limitations of the Brinkman–Forchheimer-extended Darcy equation, *International Journal of Heat and Fluid Flow*, 16 (1995) 11–15.

[209] ANSYS, *ANSYS Fluent 17.1: Theory Guide*, ANSYS Incorporation, Canonsburg, 2016.

[210] H. Versteeg, W. Malalasekera, *An Introduction to Computational Fluid Dynamics*, 2nd ed., Pearson Education, England, 2007.

[211] K. Vafai, *Handbook of Porous Media*., Marcel Dekker Inc., New York, 2000.

[212] R. Pietlicki, I.R. Barden, Inertial model of flow through porous media, *International Association of Hydrological Sciences*, 237 (1996) 443–452.

[213] W. Lipiński, E. Abbasi-Shavazi, J. Chen, J. Coventry, M. Hangi, S. Iyer, A. Kumar, L. Li, S. Li, J. Pye, J.F. Torres, B. Wang, Y. Wang, V.M. Wheeler, Progress in heat transfer research for high-temperature solar thermal applications, *Applied Thermal Engineering*, (2020) 116137.

[214] V.M.W. M. Hangi, W. Lipinski,, Numerical investigation of heat and mass transfer in a structured packed bed of porous spherical particles, *Proceedings of the 16th International Heat Transfer Conference, Beijing, China*, 22800 (2018).

[215] M.S. Anghelescu, Thermal and Mechanical Analysis of Carbon Foam, *Ohio University*, USA, 2009.

[216] K.K. Bodla, J.Y. Murthy, S.V. Garimella, Microtomography-based simulation of transport through open-cell metal foams, *Numerical Heat Transfer, Part A: Applications*, 58 (2010) 527–544.

[217] A. Diani, K.K. Bodla, L. Rossetto, S.V. Garimella, Numerical investigation of pressure drop and heat transfer through reconstructed metal foams and comparison against experiments, *International Journal of Heat and Mass Transfer*, 88 (2015) 508–515.

[218] Z. Wu, C. Caliot, G. Flamant, Z. Wang, Numerical simulation of convective heat transfer between air flow and ceramic foams to optimise volumetric solar air receiver performances, *International Journal of Heat and Mass Transfer*, 54 (2011) 1527–1537.

[219] R. Bala Chandran, R. Bader, W. Lipiński, Transient heat and mass transfer analysis in a porous ceria structure of a novel solar redox reactor, *International Journal of Thermal Sciences*, 92 (2015) 138–149.

[220] R. Bala Chandran, J.H. Davidson, Model of transport and chemical kinetics in a solar thermochemical reactor to split carbon dioxide, *Chemical Engineering Science*, 146 (2016) 302–315.

[221] R. Bala Chandran, R.M. De Smith, J.H. Davidson, Model of an integrated solar thermochemical reactor/reticulated ceramic foam heat exchanger for gas-phase heat recovery, *International Journal of Heat and Mass Transfer*, 81 (2015) 404–414.

[222] C.K. Ho, S.W. Webb, *Gas Transport in Porous Media*, Springer, Dordrecht, 2006.

[223] H. Sun, J. Yao, D.-y. Fan, C.-c. Wang, Z.-x. Sun, Gas transport mode criteria in ultra-tight porous media, *International Journal of Heat and Mass Transfer*, 83 (2015) 192–199.